Non-Invasive Electromagnetic Ablation of Female Breast Tumors

Wyger M. Brink
1266225

September 17, 2010

Committee members:

Prof. dr. sci. A.G. Yarovoy
Dr. ir. B.J. Kooij
Dr. ing. I.E. Lager
Dr. ir. R.F. Remis

Microwave Technology and Systems for Radar
Department of Electrical Engineering
Faculty of Electrical Engineering, Mathematics and Computer Science
Delft University of Technology

If we knew what we were doing,
then it wouldn't be called research
– Albert Einstein

Abstract

Breast cancer is the most common malignant tumor among women today. Available techniques for treating breast cancer often introduce strong side effects. The non-invasive electromagnetic ablation of breast tumors has a lot of potential, because it can provide a quick treatment modality without introducing harmful side effects.

In this project we assess the feasibility of non-invasive electromagnetic ablation of female breast tumors. The two main challenges in this project are

1. The computation of electromagnetic fields inside the female breast.
2. The focussing of power such that the power dissipated in the tumor is maximized while the power dissipated in healthy tissue is minimized.

In our investigation we simulate a two-dimensional configuration with a circular array of line-sources operating at a single-frequency within the range of 1 to 10 GHz. The electromagnetic fields are computed using a discretized EFIE method, after which we evaluate three algorithms that focus the dissipated power in order to gain insight in the potential of this treatment modality.

Preface

I present this thesis in the partial fulfillment of the requirements for the MSc degree in Electrical Engineering from the Delft University of Technology. The medical application of technology has always inspired me and finishing my study with this thesis project has therefore been a great joy. I hope that I can delight the reader with the mathematical ‘elegance’ by which the subject is treated, as much as I enjoyed this.

I would like to thank my supervisor Dr. ir. B.J. Kooij, whose support enabled me to develop a thorough understanding of the subject and helped me straighten the theoretical fundaments of this thesis. I also thank my supervisor Dr. ing. I.E. Lager for his thorough review of this thesis, tips with LaTeX and lessons in writing a scientific account. Furthermore, I have enjoyed the company of my student colleagues, Hossein, Pablo and Mark. Finally, I thank Anthilde for her moral support and love.

Wyger M. Brink

Delft, September 2010

Contents

Chapter 1

Introduction

This thesis concerns a non-invasive treatment modality for treating breast cancer using focused electromagnetic waves. In this introductory chapter we will discuss the background and context of this thesis. After a general introduction, we will successively pay attention to the problem statement, our notation conventions and, finally, to the outline of this thesis.

1.1 Breast cancer treatment

Breast cancer is the most common malignant tumor among women today. Within the European Union, every 7.5 minutes a woman dies from this disease [39]. Following lung cancer, it is the second leading cause of death due to cancer for women. Among women of the age 35–55, this disease forms the leading cause of death. One out of eight women is expected to be affected by this type of cancer during her life.

Breast cancer is a disease which causes cells in the breast to change and grow in an uncontrolled manner. The cancer cells eventually form a lump or mass called a ‘tumor’. The breast is made up of glands for milk production and ducts that connect these glands to the nipple. The remainder of the breast is made up of adipose (fatty) and fibroconnective tissue. This is illustrated in Fig. 1.1. Most breast tumors originate in the ducts and glands of the breast.

Available techniques for treating breast cancer often introduce strong side effects. The most common treatment is surgical treatment like mastectomy, a radical approach which comes down to removing the entire breast, or lumpectomy, where only part of the breast is removed. Ablative therapies that cause cellular damage are also common, like radiation therapy and chemotherapy. A treatment modality that has received a lot of attention in the past, is thermal therapy. The thermal treatment of cancer has a lot of potential, since it can offer a non-invasive treatment with low side effects. Therefore, further development of this approach deserves attention.

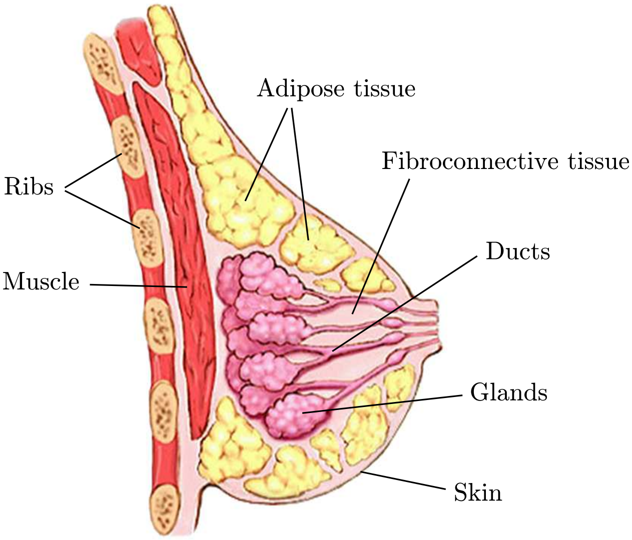

Fig. 1.1: The anatomy of the breast

In the thermal treatment of cancer, the tissue temperature is raised in order to kill the malignant tissue. Among thermal therapies we can make a clear distinction between hyperthermia and thermal ablation, which differ in the temperature elevation that is applied to the tissue. Hence, these two approaches are based on different biological damage processes.

Hyperthermia therapy aims on maintaining a moderate temperature elevation for a longer period of time [42]. This type of treatment applies temperatures between 42 and 47 degrees, for which it known that cellular damage increases exponentially with treatment time and temperature [16]. The tumor is more sensitive for this excess heat due to its chaotic vascular structure [45]. Hyperthermia has also shown to increase the effectiveness of chemo- or radiation therapy [21]. Hyperthermia treatment is typically performed in multiple sessions spread over several weeks, with each session lasting 30 minutes to hours. This makes this type of treatment very costly. Furthermore, the acquired thermotolerance of the tissue reduces the effectiveness of subsequent treatment sessions [36].

In thermal ablation, or local hyperthermia, the goal is to obtain the highest possible temperature in the tumor for only a short period of time in order to irreversibly destruct the tumor tissue. At temperatures from approximately 50 ℃ up to 100 ℃, protein coagulation causes almost immediate irreversible cell death. Higher temperatures cause tissue boiling, tissue water vaporization and eventually carbonization of the tissue [13].

Thermal ablation can be applied using various techniques which can be categorized into minimally-invasive, like radiofrequency ablation and microwave ablation where an electrode is inserted in the tumor tissue [13, 40], and non-invasive, like focused microwave ablation or high intensity focused ultrasound where electromagnetic or acoustic energy is focused at the tumor tissue. Comparison studies show that electromagnetic heating is much more efficient than acoustic heating [3]. Therefore, this approach may offer a non-invasive, quick and power-efficient technique for the treatment of female breast cancer.

1.2 Problem statement

The challenge in focused microwave ablation is to avoid heating the healthy tissue while heating the tumor. The relatively high conductivity of tumor tissue increases the local heating potential, thus high temperature gradients can be obtained. However, healthy glandular tissue and skin tissue also possess a high conductivity, which implies that secondary (unwanted) hot spots may appear there. Hot spots in the healthy tissue result in undesired side effects like extra pain, burns and blisters. Also, these hot spots deteriorate the system efficiency.

Several techniques that focus electromagnetic energy at a tumor have been developed in the past. The ability of magnetic materials and nanoparticles to locally absorb electromagnetic energy and convert this energy into heat is exploited in [17] and [18]. In [14] simulation results show that a slab of metamaterial can be used to focus the electromagnetic field of an external electromagnetic source.

A more flexible approach for focusing electromagnetic energy is the use of a phased array system. The resulting power distribution can be steered by adjusting the amplitude and phase of each array element. This type of applicator has already been used in electromagnetic systems at radiofrequencies (e.g. 10-1000 MHz) [9, 38, 41] and in acoustic systems [3, 20]. It is shown in [10, 11] that a phased array can be used to adaptively steer nulls at preassigned areas of the target body, while heating the part that contains the tumor. However, thermal ablation is not possible at these frequencies since the focal spot includes a large part of the body.

From antenna theory we know that, for a fixed antenna size, the main beamwidth is proportional to the wavelength. In other words, using a higher frequency could increase the ability of a phased array system to selectively heat the tumor. It is derived in [9] that the focal spot size of a ring array antenna equals half the wavelength in the target body. In focused microwave ablation, this would imply that frequencies between 1 and 10 GHz can induce a focal spot size in the range of centimeters to millimeters.

However, increasing the frequency deteriorates the transmission of power into the breast [9]. Also, the heterogeneous structures will cause the wavefields to be scattered in a more diffuse manner. Due to internal reflections, resonances and standing wave phenomena, additional hot spots may be induced. These effects imply the need for an accurate propagation model in order to assess the feasibility of focused microwave ablation of female breast cancer.

Next to computing the fields, we need a method for finding the controls that optimize the resulting power distribution in the breast. Several methods have been developed in the past for optimizing the heating pattern in hyperthermia. Simple methods exist like the target center position method [3] or conjugate field matching [33, 34], in which the only objective is to obtain constructive interference at one point in the target body. These methods do not concern covering the whole tumor and they do not concern reducing power dissipation in the surrounding healthy tissue. Therefore, these methods are not appropriate for focused microwave ablation.

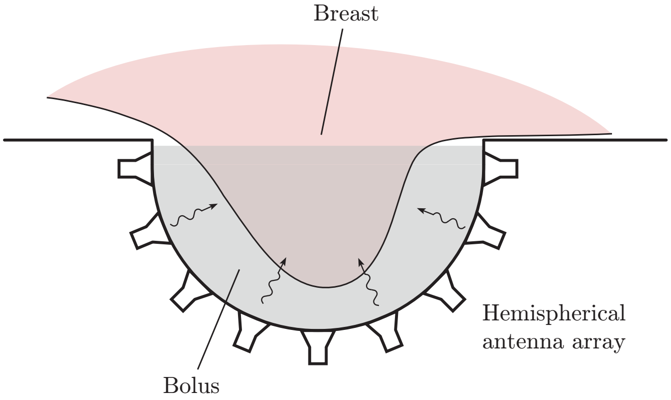

Fig. 1.2: A focused microwave ablation system for the treatment of breast cancer

More sophisticated also exist like adaptive nulling [9, 10] or temperature based optimization [26]. The latter two methods are not useful in this feasibility study since our only objective is to obtain the most localized temperature distribution, and therefore the most localized power distribution.

A common problem encountered in array pattern synthesis is that of conflicting objectives [2]. For example, increasing the dissipated power in the focus will inherently increase the power dissipated in the healthy tissue. This has also been proven by [23]. Also, increasing the amount of destructive interference in the healthy tissue will degrade the power distribution in the target area. Thus, for optimizing the power distribution is the breast, an algorithm needs to be devised in such a way that it handles the conflicting objectives of thermal ablation in a correct manner.

1.3 Project goal

The goal of this project is to assess the feasibility of non-invasive electromagnetic ablation of female breast tumors by designing an algorithm that optimizes the power distribution. We propose using a hemispherical antenna array configuration operating at a single-frequency between 1 and 10 GHz. The patient will be prone positioned, i.e. laying face-down, on a treatment table and the hemispherical antenna array encloses the breast from below. The space in between the breast and the applicator is filled with a bolus in order to improve the coupling between the applicator and the breast. This configuration is illustrated in Fig. 1.2.

For our investigation, we will simulate a two-dimensional configuration with line sources surrounding a transverse section of the breast. After computing the electromagnetic fields, we evaluate the focusing ability of three focusing algorithms.

We assume that an electromagnetic model of the patient's breast is available. This model could for instance be obtained through magnetic resonance imaging or even better, microwave imaging using the same array configuration [28]. The latter can improve the system a lot since errors due to mismatches in the propagation model could then automatically be corrected. However, since this research is limited to a feasibility study, we assume that the propagation models are known in advance.

For modeling the temperature increase in thermal ablation we assume that the influence of thermal conduction, perfusion and metabolic heating can be neglected. Thus, the local temperature increase is proportional to the dissipated power and the treatment duration. We thus only need to obtain a localized dissipated power pattern in order to assess the feasibility of focused microwave ablation. A justification of this approach can be found in Appendix A, where also a quantative goal of the system is formulated.

It is known that the skin tissue has a high conductivity and, hence, it will be inevitable that the surface of the breast is also heated during the treatment. We follow the approach suggested in [7] and assume that the breast is superficially cooled by the bolus material beforehand. Therefore, we will not consider reducing the power dissipation in the skin as an objective in this study.

We assume that the electromagnetic behaviour of the breast tissue is linear, dispersive, isotropic and time-invariant. We also assume that the tissue properties are independent of the temperature. A temperature dependency of the electromagnetic properties of liver tissue has been shown in [29]. Although the heterogeneous structure remains approximately the same, there are still some changes in permittivity and conductivity values. Therefore, this assumption does not impede on the feasibility of thermal ablation, but the thermal dependence will eventually have to be taken into account in order to prevent defocusing of the field during the treatment.

1.4 Notation conventions

In this section we will define some of the notation conventions that will be used throughout this thesis.

- Symbols that denote a variable are written in '*italic*' font. Symbols that represent a constant are written in 'roman' font, except for the greek symbols that represent a constant.

- Scalar quantities are put in a 'plain' typeset. Vector valued quantities will be represented by a symbol with a **bold** typeset.

- The location of a point in space will be represented by its position vector $\boldsymbol{x} = \mathbf{i}_1 x_1 + \mathbf{i}_2 x_2 + \mathbf{i}_3 x_3$ with three spatial coordinates indicating the position of the point with respect to the origin $\mathcal{O}$ of a right-handed, orthogonal, Cartesian reference frame consisting of three base vectors $\{\mathbf{i}_1, \mathbf{i}_2, \mathbf{i}_3\}$ that are each of unit length. The spatial differentiation operator ∇ is defined as $\nabla = \mathbf{i}_1\partial_1 + \mathbf{i}_2\partial_2 + \mathbf{i}_3\partial_3$.

- Time instants are represented by the time coordinate t.

1.5 Thesis outline

The outline of this thesis is as follows;

Chapter 2: Basic electromagnetic equations

In Chapter 2, we present the mathematical and physical fundaments for electromagnetic wave phenomena. From the local form of Maxwell's equations we derive a pair of coupled integral equations from which the field in inhomogeneous media can be evaluated.

Chapter 3: General configuration

Chapter 3 covers the general configuration that is used to support our investigation. First we describe the two-dimensional configuration that is used in this investigation. Then we present the model that is used to describe the interaction between the breast and the electromagnetic field.

Chapter 4: The forward scattering problem

This chapter describes the method that is used to compute the electromagnetic fields in inhomogeneous media. After presenting the Electric Field Integral Equation (EFIE), we describe the discretization of the computational domain. Chapter 4 is concluded by describing the conjugate gradient method for computing the electric field in the breast model.

Chapter 5: Power optimization

The theoretical part of this thesis is completed by presenting three algorithms that optimize the power distribution inside the breast. First we derive an eigenvalue method that maximizes the average power dissipated in the tumor. A similar eigenvalue method results from maximizing this quantity with respect to the average power dissipated in the healthy tissue. We conclude Chapter 5 by presenting a conjugate gradient scheme that optimizes a given power dissipation pattern in order to suppress undesired hot spots.

Chapter 6: Numerical simulations and results

In this chapter we present numerical simulations by which we determine remaining system parameters and the results obtained with the various power optimization methods. Through these results we evaluate the feasibility of non-invasive electromagnetic ablation of female breast tumors.

Chapter 7: Conclusions and recommendations

Chapter 7 completes this thesis by presenting the conclusions that can be drawn from this research, together with a number of recommendations for future development.

Chapter 2

Basic electromagnetic equations

This chapter covers the basic electromagnetic equations which form the basis for any electromagnetic analysis. We will start with presenting the local form of Maxwell's equations for the electromagnetic field in matter. From these equations we aim to analytically derive a system of coupled integral equations from which the field in an inhomogeneous medium can be evaluated. More background on the equations that govern the electromagnetic field can be found in [19].

2.1 Time domain Maxwell's equations

As a starting point for the description of electromagnetic waves we take the local form of Mawell's equations in matter. In vector notation, these are given by

$$-\nabla \times \boldsymbol{H} + \boldsymbol{J}^{\mathrm{con}} + \partial_t \boldsymbol{D} = -\boldsymbol{J}^{\mathrm{ext}} \tag{2.1}$$

$$\nabla \times \boldsymbol{E} + \partial_t \boldsymbol{B} = -\boldsymbol{K}^{\mathrm{ext}} \tag{2.2}$$

where $\boldsymbol{E}$ is the electric field strength, $\boldsymbol{H}$ is the magnetic field strength, $\boldsymbol{D}$ denotes the electric flux density and $\boldsymbol{B}$ denotes the magnetic flux density. The quantities $\partial_t \boldsymbol{D}$ and $\partial_t \boldsymbol{B}$ are also known as the volume density of the electric and magnetic displacement current, respectively. The volume density of the electric conduction current is represented by $\boldsymbol{J}^{\mathrm{con}}$.

The symbols $\boldsymbol{J}^{\mathrm{ext}}$ and $\boldsymbol{K}^{\mathrm{ext}}$ represent the volume densities of the external electric and magnetic current. These current densities describe the sources that generate the electromagnetic field, they are given and are field-independent.

The electromagnetic field quantities are numerically represented according to the International Systems of Units (SI). These are given in Table 2.1.

Table 2.1: Electromagnetic field quantities and their SI-units

Symbol	Unit	Quantity
$\boldsymbol{E}$	V/m	electric field strength
$\boldsymbol{H}$	A/m	magnetic field strength
$\boldsymbol{D}$	C/m^2	electric flux density
$\boldsymbol{B}$	T	magnetic flux density
$\boldsymbol{J}$	A/m^2	electric current density
$\boldsymbol{K}$	V/m^2	magnetic current density

2.1.1 Compatibility relations

Supplementary relations are obtained when we apply the divergence operator $(\nabla\cdot)$ to Eqs. (2.1) and (2.2). This yields

$$\nabla\cdot\boldsymbol{J}^{\text{con}} + \partial_t\nabla\cdot\boldsymbol{D} = -\nabla\cdot\boldsymbol{J}^{\text{ext}} \tag{2.3}$$

$$\partial_t\nabla\cdot\boldsymbol{B} = -\nabla\cdot\boldsymbol{K}^{\text{ext}}\,. \tag{2.4}$$

These equations are known as the compatibility relations and form necessary conditions for solutions of Maxwell's equations to exist.

2.1.2 Constitutive relations

The constitutive relations describe the macroscopic reaction of matter to an electromagnetic field. They relate the electric conduction current and the electric and magnetic flux densities $\{\boldsymbol{J}^{\text{con}}, \boldsymbol{D}, \boldsymbol{B}\}$ to the fields $\{\boldsymbol{E},\boldsymbol{H}\}$. The constitutive parameters and constants that are involved in these relations are given in Table 2.2. In our general form of Maxwell's equations we consider linear, time-invariant, causal, locally reacting, relaxating, dispersive, isotropic, and inhomogeneous media.

The constitutive relations are defined through relaxation functions, which describe the impulse response of the medium. These functions allow us to write the reaction of the medium to a field quantity as a convolution. For example, the electric conduction current $\boldsymbol{J}^{\text{con}}$ is related to the electric field strength $\boldsymbol{E}$ through a convolution with the relaxation function of conduction $\kappa^{(\text{c})}$. This is written as

$$\boldsymbol{J}^{\text{con}}(\boldsymbol{x},t) = \int\limits_{-\infty}^{\infty} \kappa^{(\text{c})}(\boldsymbol{x},t-t')\boldsymbol{E}(\boldsymbol{x},t')\mathrm{d}t' = \kappa^{(\text{c})}(\boldsymbol{x},t) \overset{t}{*} \boldsymbol{E}(\boldsymbol{x},t)\,. \tag{2.5}$$

Causality of the medium implies that at a certain instant t, the quantities $\{\boldsymbol{J}^{\text{con}}, \boldsymbol{D}, \boldsymbol{B}\}$ depend on the values of $\{\boldsymbol{E}, \boldsymbol{H}\}$ at instants up till t, only. Thus, we should actually consider the convolution integral for values of t' up till t, only. This is enforced by

Table 2.2: Constitutive parameters and their SI-units

Symbol	Unit	Quantity
$\kappa^{(\mathrm{c})}$	S/(m·s)	relaxation function of conductivity
$\hat{\sigma}$	S/m	conductivity
$\kappa^{(\mathrm{e})}$	F/(m·s)	relaxation function of permittivity
$\hat{\varepsilon}$	F/m	permittivity
$\kappa^{(\mathrm{m})}$	H/(m·s)	relaxation function of permeability
$\hat{\mu}$	H/m	permeability
Numerical values		
$\mathrm{c}_0 = 299792458$ m/s; $\mu_0 = 4\pi \times 10^{-7}$ H/m; $\varepsilon_0 = (\mu_0 \mathrm{c}_0^2)^{-1} \approx 8.8541878 \times 10^{-12}$ F/m		

requiring that $\kappa^{(\mathrm{c})}(\boldsymbol{x}, t)$ satisfies

$$\kappa^{(\mathrm{c})}(\boldsymbol{x}, t) = \kappa^{(\mathrm{c})}(\boldsymbol{x}, t)\mathcal{H}(t) \tag{2.6}$$

where

$$\mathcal{H}(t) = \begin{cases} 0 & \forall \quad t < 0 \\ \frac{1}{2} & \forall \quad t = 0 \\ 1 & \forall \quad t > 0 \end{cases} \tag{2.7}$$

is the Heaviside step function.

Now, by imposing the causality condition of Eq. (2.6) on all relaxation functions, the constitutive relations are written as

$$\boldsymbol{J}^{\mathrm{con}}(\boldsymbol{x}, t) = \kappa^{(\mathrm{c})}(\boldsymbol{x}, t) \overset{t}{*} \boldsymbol{E}(\boldsymbol{x}, t) \tag{2.8}$$

$$\boldsymbol{D}(\boldsymbol{x}, t) = \kappa^{(\mathrm{e})}(\boldsymbol{x}, t) \overset{t}{*} \boldsymbol{E}(\boldsymbol{x}, t) \tag{2.9}$$

$$\boldsymbol{B}(\boldsymbol{x}, t) = \kappa^{(\mathrm{m})}(\boldsymbol{x}, t) \overset{t}{*} \boldsymbol{H}(\boldsymbol{x}, t)\,. \tag{2.10}$$

2.2 Frequency domain Maxwell's equations

Maxwell's equations in the time domain can be simplified with no (or minimal) loss of generality using analytical techniques. In most problems, one is interested in the behavior of a time-invariant configuration with linear and causal media. In these cases, one can advantageously describe the problem via its Laplace domain representation, which is obtained by applying the Laplace transform with respect to time. From this representation, we can easily go to the frequency domain representation of Maxwell's equations.

2.2.1 The Laplace domain

In the Laplace domain representation, the dependence on the time coordinate is transformed into the dependence on the complex parameter s. Also, temporal differentiation ∂_t is transformed into a multiplication by s and convolutions in the time domain are transformed into multiplications.

Take $\boldsymbol{E}(\boldsymbol{x}, t)$ as an example of an electromagnetic quantity that is causally related to a source which is switched on at instant t_0. The Laplace transform with respect to time of $\boldsymbol{E}(\boldsymbol{x}, t)$ is then defined as

$$\hat{\boldsymbol{E}}(\boldsymbol{x}, s) = \mathcal{L}_t\{\boldsymbol{E}(\boldsymbol{x}, t)\} = \int\limits_{t_0}^{\infty} \boldsymbol{E}(\boldsymbol{x}, t)\mathrm{e}^{-st}\mathrm{d}t\,, \quad \text{for } \mathrm{Re}\{s\} > s_0 \geq 0 \tag{2.11}$$

where s denotes the complex Laplace transform parameter and $\hat{\boldsymbol{E}}$ is an analytic function, i.e. differentiable with respect to s, in the right half of the complex s-plane for $\mathrm{Re}\{s\} > s_0 \geq 0$.

When a solution has been found in the Laplace domain, one can obtain the solution in the time domain by using the inverse Laplace transform. However, we are not interested in the transient behavior of the fields but rather in the steady state behavior of single-frequency sinusoidally varying or harmonic wave fields. This information can be retrieved without the need for applying the inverse Laplace transform, namely through a frequency domain analysis.

Frequency domain analysis

In a frequency domain analysis all field quantities depend sinusoidally on time with a common angular frequency $\omega = 2\pi f$ where f is the common frequency. It is related to the Laplace domain representation by considering the limiting case with

$$s = \lim_{\delta \downarrow 0}(\delta + \mathrm{j}\omega) = \mathrm{j}\omega \tag{2.12}$$

in which j is the imaginary unit ($\mathrm{j}^2 = -1$).

In the frequency domain analysis, a time-dependent quantity like $\boldsymbol{E}(\boldsymbol{x}, t)$ is represented by a time-independent complex phasor $\hat{\boldsymbol{E}}(\boldsymbol{x}, \omega)$ and a common time factor $\mathrm{e}^{\mathrm{j}\omega t}$. The time domain quantity can be retrieved from its complex counterpart through

$$\boldsymbol{E}(\boldsymbol{x}, t) = \mathrm{Re}\Big\{\hat{\boldsymbol{E}}(\boldsymbol{x}, \omega)\mathrm{e}^{\mathrm{j}\omega t}\Big\}\,. \tag{2.13}$$

2.2.2 Transforming Maxwell's equations

After applying the Laplace transform with respect to time on Eqs. (2.1) and (2.2), and applying the limiting case where $s = \mathrm{j}\omega$, we arrive at

$$-\nabla \times \hat{\boldsymbol{H}} + \hat{\boldsymbol{J}}^{\mathrm{con}} + \mathrm{j}\omega \hat{\boldsymbol{D}} = -\hat{\boldsymbol{J}}^{\mathrm{ext}} \tag{2.14}$$

$$\nabla \times \hat{\boldsymbol{E}} + \mathrm{j}\omega \hat{\boldsymbol{B}} = -\hat{\boldsymbol{K}}^{\mathrm{ext}}\,. \tag{2.15}$$

The constitutive relations can also be transformed to the frequency domain resulting in

$$\hat{\boldsymbol{J}}^{\mathrm{con}}(\boldsymbol{x},\omega) = \hat{\sigma}(\boldsymbol{x},\omega)\hat{\boldsymbol{E}}(\boldsymbol{x},\omega) \tag{2.16}$$

$$\hat{\boldsymbol{D}}(\boldsymbol{x},\omega) = \hat{\varepsilon}(\boldsymbol{x},\omega)\hat{\boldsymbol{E}}(\boldsymbol{x},\omega) \tag{2.17}$$

$$\hat{\boldsymbol{B}}(\boldsymbol{x},\omega) = \hat{\mu}(\boldsymbol{x},\omega)\hat{\boldsymbol{H}}(\boldsymbol{x},\omega) \tag{2.18}$$

where the scalar functions $\hat{\sigma}$, $\hat{\varepsilon}$ and $\hat{\mu}$ are the frequency domain representations of the relaxation functions of conductivity, permittivity and permeability, respectively.

By substituting Eqs. (2.16)–(2.18) in Eqs. (2.14) and (2.15), we can rewrite them as

$$-\nabla \times \hat{\boldsymbol{H}} + \hat{\eta}\hat{\boldsymbol{E}} = -\hat{\boldsymbol{J}}^{\mathrm{ext}} \tag{2.19}$$

$$\nabla \times \hat{\boldsymbol{E}} + \hat{\zeta}\hat{\boldsymbol{H}} = -\hat{\boldsymbol{K}}^{\mathrm{ext}} \tag{2.20}$$

in which

$$\hat{\eta}(\boldsymbol{x},\omega) = \hat{\sigma}(\boldsymbol{x},\omega) + \mathrm{j}\omega\hat{\varepsilon}(\boldsymbol{x},\omega) \tag{2.21}$$

$$\hat{\zeta}(\boldsymbol{x},\omega) = \mathrm{j}\omega\hat{\mu}(\boldsymbol{x},\omega) \tag{2.22}$$

are the transverse admittance and the longitudinal impedance per unit length, respectively.

The compatibility relations are transformed to the frequency domain as well by applying the Laplace transform and taking $s = \mathrm{j}\omega$. Then by inserting Eqs. (2.16)–(2.18), (2.21) and (2.22) in Eqs. (2.3) and (2.4), we write the compatibility relations as

$$\nabla \cdot \hat{\eta}\hat{\boldsymbol{E}} = -\nabla \cdot \hat{\boldsymbol{J}}^{\mathrm{ext}} \tag{2.23}$$

$$\nabla \cdot \hat{\zeta}\hat{\boldsymbol{H}} = -\nabla \cdot \hat{\boldsymbol{K}}^{\mathrm{ext}}\,. \tag{2.24}$$

2.2.3 Electromagnetic power flow

Understanding the principles of electromagnetic power flow is essential for designing a tumor ablation system, since it is fundamental to its operation. The electromagnetic power flow is described by the Poynting vector

$$\boldsymbol{S} = \boldsymbol{E} \times \boldsymbol{H} \tag{2.25}$$

which measures the local and instantaneous power flow density. This quantity forms the basis for the equation describing the electromagnetic power balance.

By performing a frequency domain analysis of the electromagnetic power flow, using the phasor representation of Eq. (2.13) for $\boldsymbol{E}$ and $\boldsymbol{H}$, we can obtain the time average value of the Poynting vector as

$$\langle \boldsymbol{S} \rangle = \tfrac{1}{2}\mathrm{Re}\Big\{ \hat{\boldsymbol{E}} \times \hat{\boldsymbol{H}}^* \Big\} \tag{2.26}$$

where the asterisk $*$ denotes the complex conjugate and the brackets $\langle \cdot \rangle$ denote time average.

By multiplying the complex conjugate of Eq. (2.19) by $\hat{\boldsymbol{E}}\cdot$ and Eq. (2.20) by $\hat{\boldsymbol{H}}^*\cdot$, adding both results and using the vector identity $\nabla\cdot(\hat{\boldsymbol{E}}\times\hat{\boldsymbol{H}}^*) = \hat{\boldsymbol{H}}^*\cdot(\nabla\times\hat{\boldsymbol{E}}) - \hat{\boldsymbol{E}}\cdot(\nabla\times\hat{\boldsymbol{H}}^*)$, we obtain after taking half of the real part

$$\nabla\cdot\langle \boldsymbol{S} \rangle + \tfrac{1}{2}\mathrm{Re}\{\hat{\eta}\}\hat{\boldsymbol{E}}\cdot\hat{\boldsymbol{E}}^* + \tfrac{1}{2}\mathrm{Re}\{\hat{\zeta}\}\hat{\boldsymbol{H}}\cdot\hat{\boldsymbol{H}}^* = -\tfrac{1}{2}\mathrm{Re}\Big\{ \hat{\boldsymbol{E}}\cdot\hat{\boldsymbol{J}}^{\mathrm{ext}^*} + \hat{\boldsymbol{H}}^*\cdot\hat{\boldsymbol{K}}^{\mathrm{ext}} \Big\}\,. \tag{2.27}$$

The right hand side of 2.27 can be interpreted as the time average value of the source power density, whose action has been described through the external electric and magnetic current densities. The first term on the left hand side, $\nabla\cdot\langle \boldsymbol{S} \rangle$, describes the time average divergence of the Poynting vector. The remaining terms on the left hand side represent the time average value of dissipated power density, P_{diss}, which is irreversibly converted into heat. We thus write

$$P_{\mathrm{diss}} = \tfrac{1}{2}\mathrm{Re}\{\hat{\eta}\}\hat{\boldsymbol{E}}\cdot\hat{\boldsymbol{E}}^* + \tfrac{1}{2}\mathrm{Re}\{\hat{\zeta}\}\hat{\boldsymbol{H}}\cdot\hat{\boldsymbol{H}}^*\,. \tag{2.28}$$

2.3 Contrast source formulation

In order to construct a system of equations from which the field in an inhomogeneous configuration can be evaluated, we will reformulate the problem. This will result in having two sets of equations concerning fields in a homogeneous medium where one of them has unknown sources. First, we will describe the general configuration of an electromagnetic scattering problem.

In general, we consider the inhomogeneities of the medium to be confined to a bounded domain, denoted as the object domain $\mathcal{D}$. This object domain is embedded in an unbounded homogeneous background medium $\mathcal{D}_{\mathrm{b}}$, characterized by the medium parameters $\hat{\eta}_{\mathrm{b}}(\omega)$ and $\hat{\zeta}_{\mathrm{b}}(\omega)$. When we removed the object from $\mathcal{D}$, a homogeneous background medium would remain. In our configuration, the constitutive parameters are functions of $\boldsymbol{x}$ and ω within $\mathcal{D}$ and are functions of ω outside $\mathcal{D}$. The sources are located in the source domain $\mathcal{S}$, which is located in $\mathcal{D}_{\mathrm{b}}$ and exterior to $\mathcal{D}$.

We can form an additional set of Maxwell's equations that define the so-called incident fields $\{\hat{\boldsymbol{E}}^{\mathrm{inc}}, \hat{\boldsymbol{H}}^{\mathrm{inc}}\}$. These fields would be present if the object was absent, thus $\mathcal{D}$ would be

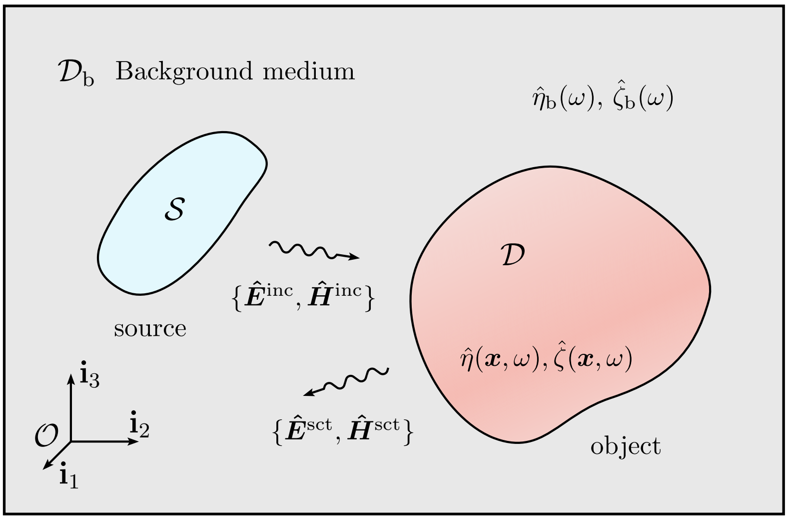

Fig. 2.1: The general scattering configuration

homogeneously filled with the background medium. Since the sources remain unchanged, we can write Maxwell's equations for this configuration as

$$-\nabla \times \hat{\boldsymbol{H}}^\mathrm{inc} + \hat{\eta}_\mathrm{b}\hat{\boldsymbol{E}}^\mathrm{inc} = -\hat{\boldsymbol{J}}^\mathrm{ext} \tag{2.29}$$

$$\nabla \times \hat{\boldsymbol{E}}^\mathrm{inc} + \hat{\zeta}_\mathrm{b}\hat{\boldsymbol{H}}^\mathrm{inc} = -\hat{\boldsymbol{K}}^\mathrm{ext}\,. \tag{2.30}$$

By subtracting Eq. (2.29) from Eq. (2.19) and Eq. (2.30) from Eq. (2.20), we obtain a new set of equations

$$-\nabla \times \hat{\boldsymbol{H}}^\mathrm{sct} + \hat{\eta}_\mathrm{b}\hat{\boldsymbol{E}}^\mathrm{sct} = -\hat{\chi}_\mathrm{e}\hat{\boldsymbol{E}} \tag{2.31}$$

$$\nabla \times \hat{\boldsymbol{E}}^\mathrm{sct} + \hat{\zeta}_\mathrm{b}\hat{\boldsymbol{H}}^\mathrm{sct} = -\hat{\chi}_\mathrm{m}\hat{\boldsymbol{H}} \tag{2.32}$$

where we have introduced the scattered fields through the relations

$$\hat{\boldsymbol{E}} = \hat{\boldsymbol{E}}^\mathrm{inc} + \hat{\boldsymbol{E}}^\mathrm{sct} \tag{2.33}$$

$$\hat{\boldsymbol{H}} = \hat{\boldsymbol{H}}^\mathrm{inc} + \hat{\boldsymbol{H}}^\mathrm{sct} \tag{2.34}$$

and the electric and magnetic contrast with respect to the background as

$$\hat{\chi}_\mathrm{e}(\boldsymbol{x},\omega) = \hat{\eta}(\boldsymbol{x},\omega) - \hat{\eta}_\mathrm{b}(\omega) \tag{2.35}$$

$$\hat{\chi}_\mathrm{m}(\boldsymbol{x},\omega) = \hat{\zeta}(\boldsymbol{x},\omega) - \hat{\zeta}_\mathrm{b}(\omega)\,. \tag{2.36}$$

An interesting feature of Eqs. (2.29)–(2.32) is that their left hand side describes the propagation of an electromagnetic wave in a homogeneous medium. So, both the incident and the scattered fields have now been formulated in such a way that the differential equation acts only in the background medium. Together, they constitute the total field.

The terms that are found on the right-hand side of Eqs. (2.31) and (2.32) can be interpreted as source contributions and are denoted as *contrast source densities* since they are the result of the total field acting on the electromagnetic contrast. The total field is the superposition of the incident and the (unknown) scattered fields, hence the contrast source densities form additional unknowns in the contrast source formulation.

2.4 Homogeneous case

We can derive an analytical solution for Maxwell's equations when homogeneous media are considered. This solution is needed in order to solve our two sets of equations Eqs. (2.29)–(2.32). In the homogeneous case the medium parameters $\hat{\eta}$ and $\hat{\zeta}$ do not depend on $\boldsymbol{x}$ and are thus functions of ω only. We can write these dependencies explicitly as

$$-\nabla \times \hat{\boldsymbol{H}}(\boldsymbol{x},\omega) + \hat{\eta}(\omega)\hat{\boldsymbol{E}}(\boldsymbol{x},\omega) = -\hat{\boldsymbol{J}}(\boldsymbol{x},\omega) \tag{2.37}$$

$$\nabla \times \hat{\boldsymbol{E}}(\boldsymbol{x},\omega) + \hat{\zeta}(\omega)\hat{\boldsymbol{H}}(\boldsymbol{x},\omega) = -\hat{\boldsymbol{K}}(\boldsymbol{x},\omega)\,. \tag{2.38}$$

2.4.1 The angular wave vector domain

The dimensionality of the equations considering homogeneous media can be reduced by applying a spatial Fourier transform. This transformation transforms the dependence on the position $\boldsymbol{x}$ into a dependence on the transform parameter $\boldsymbol{k} = \mathbf{i}_1 k_1 + \mathbf{i}_2 k_2 + \mathbf{i}_3 k_3$ denoted as the angular wave vector. By applying the spatial Fourier transform, spatial derivatives (∇) are transformed into multiplications by $\mathrm{j}\boldsymbol{k}$ and spatial convolutions are transformed into multiplications. This technique is very useful in particular in the homogeneous configuration.

In general, when considering a d-dimensional space, i.e. where $\boldsymbol{x} \in \mathbb{R}^d$, the spatial Fourier transform of $\hat{\boldsymbol{E}}(\boldsymbol{x},\omega)$ is defined as

$$\tilde{\boldsymbol{E}}(\boldsymbol{k},\omega) = \mathcal{F}_{\boldsymbol{x}}\{\hat{\boldsymbol{E}}(\boldsymbol{x},\omega)\} = \int\limits_{\boldsymbol{x}\in\mathbb{R}^d} \hat{\boldsymbol{E}}(\boldsymbol{x},\omega)\mathrm{e}^{-\mathrm{j}\boldsymbol{k}\cdot\boldsymbol{x}}\mathrm{d}\boldsymbol{x} \quad \forall \quad \boldsymbol{k} \in \mathbb{R}^d \tag{2.39}$$

where it is necessary for the convergence of the integral that $\boldsymbol{E}(\boldsymbol{x},\omega)$ is absolutely integrable with respect to $\boldsymbol{x}$. This is in general the case since field amplitudes go to zero when $|\boldsymbol{x}| \to \infty$.

To recover $\hat{\boldsymbol{E}}(\boldsymbol{x},\omega)$ in the spatial domain we apply the d-dimensional inverse spatial Fourier transform which is defined as

$$\hat{\boldsymbol{E}}(\boldsymbol{x},\omega) = \mathcal{F}_{\boldsymbol{k}}^{-1}\{\tilde{\boldsymbol{E}}(\boldsymbol{k},\omega)\} = \frac{1}{(2\pi)^d} \int\limits_{\boldsymbol{k}\in\mathbb{R}^d} \tilde{\boldsymbol{E}}(\boldsymbol{k},\omega)\mathrm{e}^{\mathrm{j}\boldsymbol{k}\cdot\boldsymbol{x}}\mathrm{d}\boldsymbol{k}\,. \tag{2.40}$$

2.4.2 Angular wave vector domain solution

We will now apply the 3-dimensional spatial Fourier transform to the frequency domain Maxwell's equations for homogeneous media, Eqs. (2.37) and (2.38), to arrive at

$$-\mathrm{j}\boldsymbol{k} \times \tilde{\boldsymbol{H}} + \hat{\eta}\tilde{\boldsymbol{E}} = -\tilde{\boldsymbol{J}} \tag{2.41}$$

$$\mathrm{j}\boldsymbol{k} \times \tilde{\boldsymbol{E}} + \hat{\zeta}\tilde{\boldsymbol{H}} = -\tilde{\boldsymbol{K}} \tag{2.42}$$

and the compatibility relations are transformed accordingly into

$$\boldsymbol{k}\cdot\hat{\eta}\tilde{\boldsymbol{E}} = -\boldsymbol{k}\cdot\tilde{\boldsymbol{J}} \tag{2.43}$$

$$\boldsymbol{k}\cdot\hat{\zeta}\tilde{\boldsymbol{H}} = -\boldsymbol{k}\cdot\tilde{\boldsymbol{K}}\,. \tag{2.44}$$

This transformation brings the equations down to two coupled linear algebraic problems with complex functions in the angular wave vector domain. Now we can derive an analytical solution to the general form of Maxwell's equations and express the unknown fields $\tilde{\boldsymbol{E}}$ and $\tilde{\boldsymbol{H}}$ via the current densities $\tilde{\boldsymbol{J}}$ and $\tilde{\boldsymbol{K}}$.

To solve 2.41 and 2.42, we rewrite them as

$$\tilde{\boldsymbol{E}} = \frac{\mathrm{j}}{\hat{\eta}}\boldsymbol{k} \times \tilde{\boldsymbol{H}} - \frac{1}{\hat{\eta}}\tilde{\boldsymbol{J}} \tag{2.45}$$

$$\tilde{\boldsymbol{H}} = -\frac{\mathrm{j}}{\hat{\zeta}}\boldsymbol{k} \times \tilde{\boldsymbol{E}} - \frac{1}{\hat{\zeta}}\tilde{\boldsymbol{K}}\,. \tag{2.46}$$

After substituting Eq. (2.46) in Eq. (2.45) and vice versa, multiplying both by $\hat{\eta}\hat{\zeta} = -\hat{k}^2$ and using the property $\boldsymbol{k} \times \boldsymbol{k} \times \boldsymbol{V} = \boldsymbol{k}(\boldsymbol{k}\cdot\boldsymbol{V}) - (\boldsymbol{k}\cdot\boldsymbol{k})\boldsymbol{V}$, we obtain

$$\big(\boldsymbol{k}\cdot\boldsymbol{k} - \hat{k}^2 - \boldsymbol{k}\boldsymbol{k}\cdot\big)\tilde{\boldsymbol{E}} = -\hat{\zeta}\tilde{\boldsymbol{J}} - \mathrm{j}\boldsymbol{k} \times \tilde{\boldsymbol{K}} \tag{2.47}$$

$$\big(\boldsymbol{k}\cdot\boldsymbol{k} - \hat{k}^2 - \boldsymbol{k}\boldsymbol{k}\cdot\big)\tilde{\boldsymbol{H}} = -\hat{\eta}\tilde{\boldsymbol{K}} + \mathrm{j}\boldsymbol{k} \times \tilde{\boldsymbol{J}} \tag{2.48}$$

where $\hat{k}$ is the complex wavenumber with $\mathrm{Im}\{\hat{k}\} \leq 0$. We note that we write $\big(\boldsymbol{k}\boldsymbol{k}\cdot\big)\tilde{\boldsymbol{E}} = \boldsymbol{k}\big(\boldsymbol{k}\cdot\tilde{\boldsymbol{E}}\big)$ for improved readability.

Now, with the compatibility relations Eqs. (2.43) and (2.44) we can rewrite Eqs. (2.47) and (2.48) as

$$\big(\boldsymbol{k}\cdot\boldsymbol{k} - \hat{k}^2\big)\tilde{\boldsymbol{E}} = \big(\hat{k}^2 - \boldsymbol{k}\boldsymbol{k}\cdot\big)\frac{1}{\hat{\eta}}\tilde{\boldsymbol{J}} - \mathrm{j}\boldsymbol{k} \times \tilde{\boldsymbol{K}} \tag{2.49}$$

$$\big(\boldsymbol{k}\cdot\boldsymbol{k} - \hat{k}^2\big)\tilde{\boldsymbol{H}} = \big(\hat{k}^2 - \boldsymbol{k}\boldsymbol{k}\cdot\big)\frac{1}{\hat{\zeta}}\tilde{\boldsymbol{K}} + \mathrm{j}\boldsymbol{k} \times \tilde{\boldsymbol{J}}\,. \tag{2.50}$$

The expression in front of $\tilde{\boldsymbol{E}}$ and $\tilde{\boldsymbol{H}}$ is a scalar, nonzero factor. Hence, we can divide by it in order to obtain

$$\tilde{\boldsymbol{E}} = \frac{1}{\boldsymbol{k}\cdot\boldsymbol{k} - \hat{k}^2}\Big[\big(\hat{k}^2 - \boldsymbol{k}\boldsymbol{k}\cdot\big)\frac{1}{\hat{\eta}}\tilde{\boldsymbol{J}} - \mathrm{j}\boldsymbol{k} \times \tilde{\boldsymbol{K}}\Big] \tag{2.51}$$

$$\tilde{\boldsymbol{H}} = \frac{1}{\boldsymbol{k}\cdot\boldsymbol{k} - \hat{k}^2}\Big[\big(\hat{k}^2 - \boldsymbol{k}\boldsymbol{k}\cdot\big)\frac{1}{\hat{\zeta}}\tilde{\boldsymbol{K}} + \mathrm{j}\boldsymbol{k} \times \tilde{\boldsymbol{J}}\Big]. \tag{2.52}$$

2.4.3 Frequency domain solution

Now we have found the expressions for the fields in the angular wave vector domain, we need to perform an inverse spatial Fourier transform on Eqs. (2.51) and (2.52) in order to obtain the expressions for the fields in the frequency domain. First we will simplify the angular wave vector domain solution, by introducing the following functions

$$\tilde{\boldsymbol{A}}(\boldsymbol{k},\omega) = \frac{1}{\hat{\eta}(\omega)}\tilde{g}(\boldsymbol{k},\omega)\tilde{\boldsymbol{J}}(\boldsymbol{k},\omega) \tag{2.53}$$

$$\tilde{\boldsymbol{F}}(\boldsymbol{k},\omega) = \frac{1}{\hat{\zeta}(\omega)}\tilde{g}(\boldsymbol{k},\omega)\tilde{\boldsymbol{K}}(\boldsymbol{k},\omega) \tag{2.54}$$

that are also known as the vector potentials in the angular wave vector domain. In these expressions we have also introduced the Green's function $\tilde{g}$ in the angular wave vector domain

$$\tilde{g}(\boldsymbol{k},\omega) = \frac{1}{\boldsymbol{k}\cdot\boldsymbol{k} - \hat{k}^2} \tag{2.55}$$

which is in fact the point-source solution of the inhomogeneous helmholtz equation.

With the normalized vector potentials we can write Eqs. (2.51) and (2.52) as

$$\tilde{\boldsymbol{E}} = \left(\hat{k}^2 - \boldsymbol{k}\boldsymbol{k}\cdot\right)\tilde{\boldsymbol{A}} - \mathrm{j}\hat{\zeta}\boldsymbol{k}\times\tilde{\boldsymbol{F}} \tag{2.56}$$

$$\tilde{\boldsymbol{H}} = \left(\hat{k}^2 - \boldsymbol{k}\boldsymbol{k}\cdot\right)\tilde{\boldsymbol{F}} + \mathrm{j}\hat{\eta}\boldsymbol{k}\times\tilde{\boldsymbol{A}}\,. \tag{2.57}$$

These expressions are transformed back to the frequency domain by applying $\mathcal{F}_{\boldsymbol{k}}^{-1}$ defined in Eq. (2.40). By recognizing the ∇ as the inverse transform of j$\boldsymbol{k}$, this gives us

$$\hat{\boldsymbol{E}} = \left(\hat{k}^2 + \nabla\nabla\cdot\right)\hat{\boldsymbol{A}} - \hat{\zeta}\nabla\times\hat{\boldsymbol{F}} \tag{2.58}$$

$$\hat{\boldsymbol{H}} = \left(\hat{k}^2 + \nabla\nabla\cdot\right)\hat{\boldsymbol{F}} + \hat{\eta}\nabla\times\hat{\boldsymbol{A}} \tag{2.59}$$

where we again write $\left(\nabla\nabla\cdot\right)\hat{\boldsymbol{A}} = \nabla\left(\nabla\cdot\hat{\boldsymbol{A}}\right)$ for improved readability.

Finally, we note that the inverse Fourier transform of the normalized vector potentials results in spatial convolutions

$$\hat{\boldsymbol{A}}(\boldsymbol{x},\omega) = \frac{1}{\hat{\eta}(\omega)}\int\limits_{\boldsymbol{x}'\in\mathbb{R}^3}\hat{g}(\boldsymbol{x}-\boldsymbol{x}',\omega)\hat{\boldsymbol{J}}(\boldsymbol{x}',\omega)\mathrm{d}V \tag{2.60}$$

$$\hat{\boldsymbol{F}}(\boldsymbol{x},\omega) = \frac{1}{\hat{\zeta}(\omega)}\int\limits_{\boldsymbol{x}'\in\mathbb{R}^3}\hat{g}(\boldsymbol{x}-\boldsymbol{x}',\omega)\hat{\boldsymbol{K}}(\boldsymbol{x}',\omega)\mathrm{d}V \tag{2.61}$$

where $\hat{g}$ is Green's function in the frequency domain, for which the actual expression is irrelevant at this point.

2.5 Integral equations for the electromagnetic field

Finally, we construct a system of integral equations from which the total electromagnetic field can be evaluated. Since the problem of solving Maxwell's equations for the field in an inhomogeneous configuration has been brought down to two problems concerning fields propagating in a homogeneous background medium, we can now use the solution found in the homogeneous case to formulate the integral representation for the total electromagnetic field.

The incident fields can be solved from Eqs. (2.29) and (2.30) using the solution of the homogeneous case, Eqs. (2.58) and (2.59), which yields

$$\hat{\boldsymbol{E}}^{\text{inc}} = \left(\hat{k}_{\text{b}}^2 + \nabla\nabla\cdot\right)\hat{\boldsymbol{A}}^{\text{inc}} - \hat{\zeta}_{\text{b}}\nabla\times\hat{\boldsymbol{F}}^{\text{inc}} \tag{2.62}$$

$$\hat{\boldsymbol{H}}^{\text{inc}} = \left(\hat{k}_{\text{b}}^2 + \nabla\nabla\cdot\right)\hat{\boldsymbol{F}}^{\text{inc}} + \hat{\eta}_{\text{b}}\nabla\times\hat{\boldsymbol{A}}^{\text{inc}} \tag{2.63}$$

where $\hat{k}_{\text{b}}$ is the complex wavenumber in the background medium with $\operatorname{Im}\{\hat{k}_{\text{b}}\} \leq 0$ and

$$\hat{\boldsymbol{A}}^{\text{inc}}(\boldsymbol{x},\omega) = \frac{1}{\hat{\eta}_{\text{b}}(\omega)} \int\limits_{\boldsymbol{x}'\in\mathcal{S}} \hat{g}(\boldsymbol{x}-\boldsymbol{x}',\omega)\hat{\boldsymbol{J}}^{\text{ext}}(\boldsymbol{x}',\omega)\mathrm{d}V \tag{2.64}$$

$$\hat{\boldsymbol{F}}^{\text{inc}}(\boldsymbol{x},\omega) = \frac{1}{\hat{\zeta}_{\text{b}}(\omega)} \int\limits_{\boldsymbol{x}'\in\mathcal{S}} \hat{g}(\boldsymbol{x}-\boldsymbol{x}',\omega)\hat{\boldsymbol{K}}^{\text{ext}}(\boldsymbol{x}',\omega)\mathrm{d}V \tag{2.65}$$

denote the vector potentials for the incident fields.

The solution for the scattered fields can be described in the same way, by considering the unknown contrast source densities as source contributions. However, we will skip this step here, and proceed to the integral equations for the electromagnetic field. Since the total field is the sum of the known incident field and the scattered field, we can write

$$\hat{\boldsymbol{E}}^{\text{inc}} = \hat{\boldsymbol{E}} - \hat{\boldsymbol{E}}^{\text{sct}} \tag{2.66}$$

$$\hat{\boldsymbol{H}}^{\text{inc}} = \hat{\boldsymbol{H}} - \hat{\boldsymbol{H}}^{\text{sct}}\,. \tag{2.67}$$

By substituting the solution for the scattered field, we find the integral equations for the electromagnetic field as

$$\hat{\boldsymbol{E}}^{\text{inc}} = \hat{\boldsymbol{E}} - \left(\hat{k}_{\text{b}}^2 + \nabla\nabla\cdot\right)\hat{\boldsymbol{A}}^{\text{sct}} + \hat{\zeta}_{\text{b}}\nabla\times\hat{\boldsymbol{F}}^{\text{sct}} \tag{2.68}$$

$$\hat{\boldsymbol{H}}^{\text{inc}} = \hat{\boldsymbol{H}} - \left(\hat{k}_{\text{b}}^2 + \nabla\nabla\cdot\right)\hat{\boldsymbol{F}}^{\text{sct}} - \hat{\eta}_{\text{b}}\nabla\times\hat{\boldsymbol{A}}^{\text{sct}} \tag{2.69}$$

in which the vector potentials for the scattered fields are expressed as

$$\hat{\boldsymbol{A}}^{\text{sct}}(\boldsymbol{x},\omega) = \frac{1}{\hat{\eta}_{\text{b}}(\omega)} \int\limits_{\boldsymbol{x}'\in\mathcal{D}} \hat{g}(\boldsymbol{x}-\boldsymbol{x}',\omega)\hat{\chi}_{\text{e}}(\boldsymbol{x}',\omega)\hat{\boldsymbol{E}}(\boldsymbol{x}',\omega)\mathrm{d}V \tag{2.70}$$

$$\hat{\boldsymbol{F}}^{\text{sct}}(\boldsymbol{x},\omega) = \frac{1}{\hat{\zeta}_{\text{b}}(\omega)} \int\limits_{\boldsymbol{x}'\in\mathcal{D}} \hat{g}(\boldsymbol{x}-\boldsymbol{x}',\omega)\hat{\chi}_{\text{m}}(\boldsymbol{x}',\omega)\hat{\boldsymbol{H}}(\boldsymbol{x}',\omega)\mathrm{d}V\,. \tag{2.71}$$

We notice that the vector potentials for the scattered fields depend on the total fields. Since these fields are unknown and appear under the integral sign, Eqs. (2.68) and (2.69) must be treated as integral equations. The integral equations are coupled since $\hat{\boldsymbol{E}}$ and $\hat{\boldsymbol{H}}$ are both unknown and appear in both equations.

The integral equations for the electromagnetic field presented in this paragraph form the starting point for computing the total electromagnetic field in inhomogeneous media. This problem, often referred to as the forward problem, can be solved numerically, which we will in Chapter 4. First, we will discuss the numerical configuration more elaborately.

Chapter 3

General configuration

In this chapter we present the general configuration that is used to support our investigation. First we will describe the two-dimensional configuration that is investigated. Subsequently we will present the model that is used to describe the interaction between the breast and the electromagnetic field.

3.1 Two-dimensional configuration

In this investigation we will use a two-dimensional configuration to model the ablation treatment. In this two-dimensional configuration, we assume that the medium parameters and the sources are independent of one spatial coordinate, say x_3. This approach will reduce the computational effort, but will still provide us a relevant indication on the feasibility of the treatment.

A two-dimensional model for the ablation system is obtained by selecting one transverse section and extending it to infinity in the x_3-direction. This corresponds to a frontal section of the breast which is encircled by a circular array of equally spaced sources, as shown in Fig. 3.1. In view of the general scattering configuration we extent the bolus to infinity in all directions. In other words, the background domain $\mathcal{D}_\mathrm{b}$ in the scattering configuration represents the bolus.

3.1.1 Two-dimensional electromagnetic equations

We shall now reformulate the electromagnetic equations in such that they describe the electromagnetic field in the two-dimensional configuration. Since there is no spatial variation in the x_3-direction, this yields $\partial_3 = 0$ and $\nabla = \mathbf{i}_1\partial_1 + \mathbf{i}_2\partial_2$. The relevant position variable will now be defined in the transverse plane as $\boldsymbol{x} = \mathbf{i}_1 x_1 + \mathbf{i}_2 x_2$. The relevant angular wave vector will also be redefined in the two-dimensional space, i.e. $\boldsymbol{k} = \mathbf{i}_1 k_1 + \mathbf{i}_2 k_2$. We can now use all equations presented in Chapter 2 keeping these changes in mind.

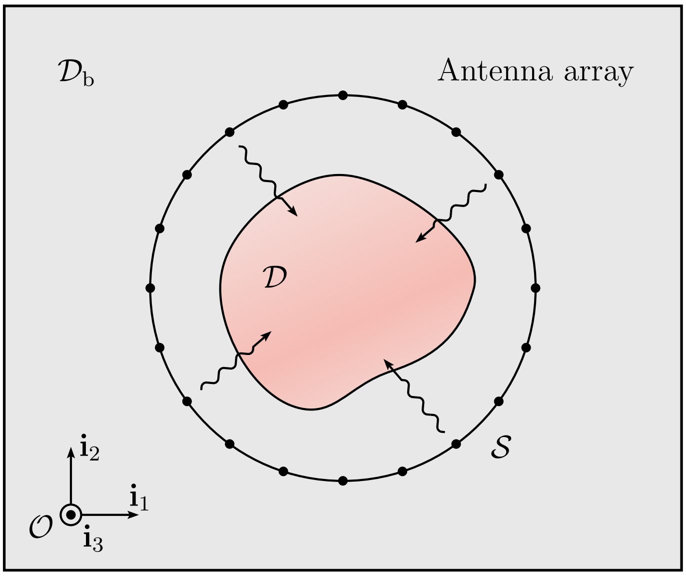

Fig. 3.1: The two-dimensional configuration

3.1.2 Polarization

In the two-dimensional formulation, the electromagnetic field decouples into two independent polarization states. The first concerns Transverse Electric (TE-) polarized waves and the second Transverse Magnetic (TM-) polarized waves. The decoupling of the electromagnetic field can be observed by substituting $\partial_3 = 0$ in Eqs. (2.62)–(2.63) and Eqs. (2.68)–(2.69). By doing so we end up with two independent sets of equations which represent the TE- and TM-polarizations.

TE-polarized waves are defined as having $\{\hat{H}_1, \hat{H}_2, \hat{E}_3\}(x_1, x_2) \neq 0$, i.e. the electric field is directed perpendicular to the direction of the power flow. By looking at the equations for the incident fields (Eqs. (2.62)–(2.65)), we see that this type of waves can be excited by the electric current density $\hat{J}_3^{\mathrm{ext}}$ and the magnetic current densities $\hat{K}_1^{\mathrm{ext}}$ and $\hat{K}_2^{\mathrm{ext}}$.

TM-polarized waves form the complement of TE-polarized waves. In other words, for this type of polarization $\{\hat{E}_1, \hat{E}_2, \hat{H}_3\}(x_1, x_2) \neq 0$ holds. TM-polarized waves can originate from the magnetic current density $\hat{K}_3^{\mathrm{ext}}$ and the electric current densities $\hat{J}_1^{\mathrm{ext}}$ and $\hat{J}_2^{\mathrm{ext}}$.

In our investigation we will only consider TM-polarized waves. This type of waves can be launched by for example a hollow waveguide or a horn antenna. In the two-dimensional case, one could imagine measuring this wave field on the corresponding plane, and extending the measured field to infinity in the x_3-direction. As a result, the dissipated power is determined by the electric field components $\{\hat{E}_1, \hat{E}_2\}$.

3.1.3 Source formulation

In the investigated configuration the sources are independent of x_3. In this respect, a convenient source model that launches TM-polarized waves is the magnetic current line source. We note that magnetic currents cannot be generated in practice. However, a magnetic current line source forms an appropriate array element in this study.

A line source has a current distribution which is located at a point on the transverse plane and stretches out to infinity in the x_3-direction. For a line source excited with unit amplitude and zero phase, this yields the following expression for the magnetic current density

$$\hat{\boldsymbol{K}}^{\mathrm{ext}}(\boldsymbol{x}) = \delta(\boldsymbol{x} - \boldsymbol{x}_s)\mathbf{i}_3 \tag{3.1}$$

where $\boldsymbol{x}_s$ denotes the location of the line source within the source domain $\mathcal{S} \subset \mathbb{R}^2$. We see that the expression does not depend on x_3, hence it stretches out to infinity in this direction.

By substituting the expression for the magnetic current density in Eqs. (2.62)–(2.65) and setting $\hat{\boldsymbol{J}}^{\mathrm{ext}} = \mathbf{0}$, we find the following expressions for the incident fields

$$\hat{\boldsymbol{E}}^{\mathrm{inc}}(\boldsymbol{x}) = -\nabla\hat{g}(\boldsymbol{x} - \boldsymbol{x}_s) \times \mathbf{i}_3 \tag{3.2}$$

$$\hat{\boldsymbol{H}}^{\mathrm{inc}}(\boldsymbol{x}) = -\mathrm{j}\omega\hat{\varepsilon}_{\mathrm{b}}\hat{g}(\boldsymbol{x} - \boldsymbol{x}_s)\mathbf{i}_3 \tag{3.3}$$

in which $\hat{g}$ is the two-dimensional Green's function.

The expression for the two-dimensional Green's function is found by applying a two-dimensional inverse Fourier transform to Eq. (2.55), with $\hat{k} = \hat{k}_{\mathrm{b}}$, which results in

$$\hat{g}(\boldsymbol{x} - \boldsymbol{x}_s) = -\frac{\mathrm{j}}{4}H_0^{(2)}(\hat{k}_{\mathrm{b}}|\boldsymbol{x} - \boldsymbol{x}_s|) \tag{3.4}$$

where $\hat{k}_{\mathrm{b}}(\omega) = \omega\sqrt{\mu_0\varepsilon_0\hat{\varepsilon}_{\mathrm{r,b}}(\omega)}$ with $\mathrm{Im}\{\hat{k}_{\mathrm{b}}\} \leq 0$ denotes the wavenumber is the background medium. More details on the derivation of the Green's function can be found in Appendix B.

The gradient of the Green's function is found to be

$$\nabla\hat{g}(\boldsymbol{x} - \boldsymbol{x}_s) = \frac{\mathrm{j}}{4}\hat{k}_{\mathrm{b}}H_1^{(2)}(\hat{k}_{\mathrm{b}}|\boldsymbol{x} - \boldsymbol{x}_s|)\frac{\boldsymbol{x} - \boldsymbol{x}_s}{|\boldsymbol{x} - \boldsymbol{x}_s|} \tag{3.5}$$

where we have used elementary differentiation rules together with the formulas for the derivatives of the Hankel function [1], which provides the relation

$$\frac{\mathrm{d}}{\mathrm{d}z}H_n^{(2)}(z) = \frac{n}{z}H_n^{(2)}(z) - H_{n+1}^{(2)}(z)\,. \tag{3.6}$$

Now we have described all aspects of the two-dimensional configuration, except for the breast model. This will be treated in the next section.

3.2 Breast model

In order to simulate the propagation of electromagnetic waves inside the female breast, we need a model that describes the interaction between the electromagnetic field and the breast. This interaction is described through the constitutive parameters $\hat{\sigma}$, $\hat{\varepsilon}$ and $\hat{\mu}$. We also need to model the heterogeneous structure of the breast.

3.2.1 Complex relative permittivity

Before we present the model for the material properties, we will define the complex relative permittivity. In the frequency domain analysis of the electromagnetic fields, the conductivity $\hat{\sigma}$ can be incorporated in the permittivity $\hat{\varepsilon}$. This leads to the definition of the complex relative permittivity.

In Chapter 2 we introduced the transverse admittance, Eq. (2.21), repeated here for convenience

$$\hat{\eta}(\boldsymbol{x},\omega) = \hat{\sigma}(\boldsymbol{x},\omega) + \mathrm{j}\omega\hat{\varepsilon}(\boldsymbol{x},\omega)\,. \tag{3.7}$$

We redefine the transverse admittance as

$$\hat{\eta}(\boldsymbol{x},\omega) = \mathrm{j}\omega\varepsilon_0\hat{\varepsilon}_\mathrm{r}(\boldsymbol{x},\omega) \tag{3.8}$$

where ε_0 is the permittivity of free space, as given in Table 2.2. From this redefinition the complex relative permittivity $\hat{\varepsilon}_\mathrm{r}$ follows as

$$\begin{aligned}\hat{\varepsilon}_\mathrm{r}(\boldsymbol{x},\omega) &= \varepsilon'_\mathrm{r}(\boldsymbol{x},\omega) - \mathrm{j}\varepsilon''_\mathrm{r}(\boldsymbol{x},\omega)\\ &= \frac{\hat{\varepsilon}(\boldsymbol{x},\omega)}{\varepsilon_0} - \mathrm{j}\frac{\hat{\sigma}(\boldsymbol{x},\omega)}{\omega\varepsilon_0}\,.\end{aligned} \tag{3.9}$$

The complex relative permittivity data is often presented by mapping the complex valued permittivity and conductivity functions into real valued relative permittivity and conductivity functions. These are written as $\varepsilon_\mathrm{r}(\boldsymbol{x},\omega) = \varepsilon'_\mathrm{r}(\boldsymbol{x},\omega)$ and $\sigma_\mathrm{eff}(\boldsymbol{x},\omega) = \omega\varepsilon_0\varepsilon''_\mathrm{r}(\boldsymbol{x},\omega)$. Using this model for the media, we can express the dissipated power (Eq. (2.28)) as

$$P_\mathrm{diss} = \tfrac{1}{2}\sigma_\mathrm{eff}\hat{\boldsymbol{E}}\cdot\hat{\boldsymbol{E}}^*\,. \tag{3.10}$$

3.2.2 Material properties

Now we will describe the electromagnetic properties of breast tissue and bolus material. It is generally known that biological tissues possess no magnetic properties at microwave frequencies, i.e. $\hat{\mu} = \mu_0$. It is also generally known that these media possess dispersive properties and exhibit losses. Breast tissues are therefore completely characterized by their permittivity $\hat{\varepsilon}$ and conductivity $\hat{\sigma}$, or complex relative permittivity $\hat{\varepsilon}_\mathrm{r}$.

Table 3.1: Cole-Cole parameters for two median dielectric properties curves

	ε_∞	$\Delta\varepsilon$	τ (ps)	α	σ_s (S/m)
glandular/fibroconnective	7.821	41.48	10.66	0.047	0.713
adipose	3.140	1.708	14.65	0.061	0.036

Breast tissue

In 2007, a large scale study has been performed on the frequency dependent dielectric properties of different types of breast tissue [30, 31]. The permittivity data was obtained by measuring the complex reflection coefficient from 0.5 GHz to 20 GHz with a small open-ended, hermetically sealed, coaxial probe connected to a vector network analyzer. The tissue composition of the probing volume was estimated using histological techniques. Finally, a statistical model was constructed for the different types of breast tissue.

A total of 807 ultrawideband (0.5-20 GHz) measurements have been performed on tissue samples obtained from reduction surgeries and cancer surgeries on 289 patients. After excluding erroneous data, for example data which is not consistent with the Kramers-Kronig relations (see, for instance [19]), 509 measurements have been used to fit a single-pole Cole-Cole constitutive relaxation model.

The single-pole Cole-Cole model is defined as

$$\hat{\varepsilon}_\mathrm{r}(\boldsymbol{x},\omega) = \varepsilon_\infty + \frac{\Delta\varepsilon}{1+(\mathrm{j}\omega\tau)^{1-\alpha}} + \frac{\sigma_\mathrm{s}}{\mathrm{j}\omega\varepsilon_0} \tag{3.11}$$

where ε_∞, $\Delta\varepsilon$, τ, α and σ_s are parameters that are used to fit the model to the measured data. The Cole-Cole parameters corresponding to the median dielectric properties of different breast tissues are given in Table 3.1. The relative permittivity and effective conductivity curves corresponding to these parameters are shown in Fig. 3.2.

As we can see from Fig. 3.2, the dielectric permittivity of the breast tissue shows a decreasing trend with frequency while the effective conductivity generally increases with frequency. Furthermore, it is clear that glandular and fibroconnective tissues exhibit higher permittivity and effective conductivity values than adipose tissues. We note that malignant tissue, which is not presented here, exhibits a slightly higher permittivity values than glandular and fibroconnective tissues.

Bolus material

We assume that the bolus, or background, surrounding the breast consists of non-magnetic material, hence $\hat{\mu} = \mu_0$ holds for all $\boldsymbol{x}$. We also assume that the bolus medium is non-conducting, in the effective sense, since that would introduce extra attenuation and cause the bolus to heat up which is undesirable in view of its function of cooling the skin. It then follows that the permittivity of the bolus $\hat{\varepsilon}_\mathrm{b}(\omega) = \varepsilon_0\varepsilon_{\mathrm{r,b}}(\omega)$ is a real valued function.

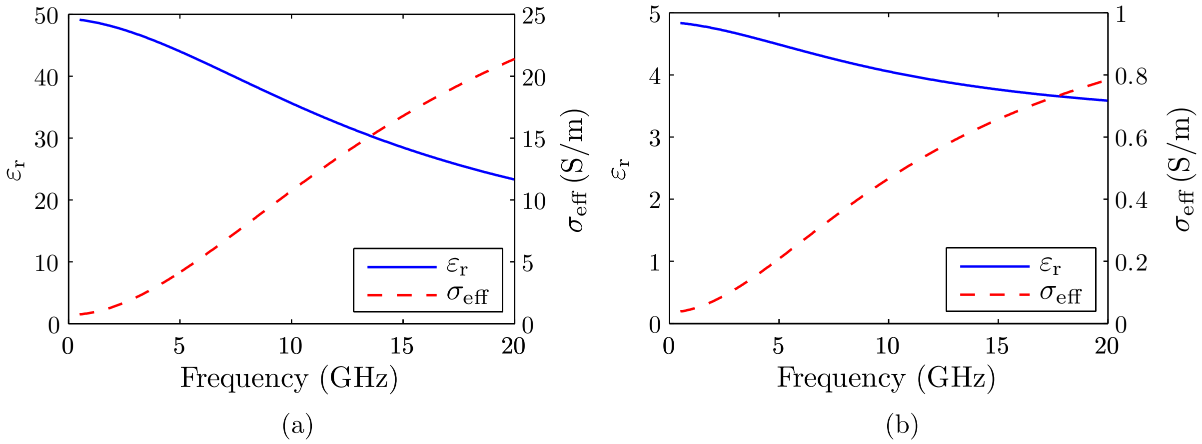

Fig. 3.2: The median dielectric permittivity and effective conductivity for (a) glandular/fibroconnective tissue and (b) adipose tissue

In this research we assume that the material properties of the bolus can be chosen in order to improve the coupling between the system and the breast. We note that introducing losses in the bolus conductivity can improve the coupling even further. However, the contrast in permittivity is much higher so matching this quantity is more important than matching the conductivity of the bolus. In Chapter 6 we will determine the optimal value of the bolus permittivity through a number of simulations.

3.2.3 Structural model

In 2008 Zastrow et al. constructed a set of three-dimensional numerical (healthy) breast models with different degrees of heterogeneity[1] [43]. The models were constructed by mapping three-dimensional T1-weighted MRI data onto the permittivity model of breast tissue as given in [30, 31]. For this procedure a piecewise linear map was used with seven linear sections. A skin layer of 1.5 mm was synthetically added to the model, because it was not imaged with a high fidelity. The model parameters corresponding to this type of tissue are given in [44]. Also, the chest wall with a layer of fat and muscle is synthetically introduced in the model. All models have a discretization step size of 0.5 mm.

From the model database we select one model of the class ‘Scattered Fibroglandular’, namely Breast ID #010204 which consists of 251-by-253-by-258 discretization cell in the x_1-, x_2- and x_3-direction respectively. A two-dimensional breast model is obtained by selecting slice number 130 in the x_3-direction. The dielectric properties of this slice are illustrated in Fig. 3.3 for $f = 5$ GHz. As one can see, several lumps of conductive tissue are scattered throughout the breast, posing some difficulties for the focusing algorithm in order not to suppress unwanted hot spots in the healthy tissue.

---

[1] This set is freely accessible via http://uwcem.ece.wisc.edu/MRIdatabase/index.html.

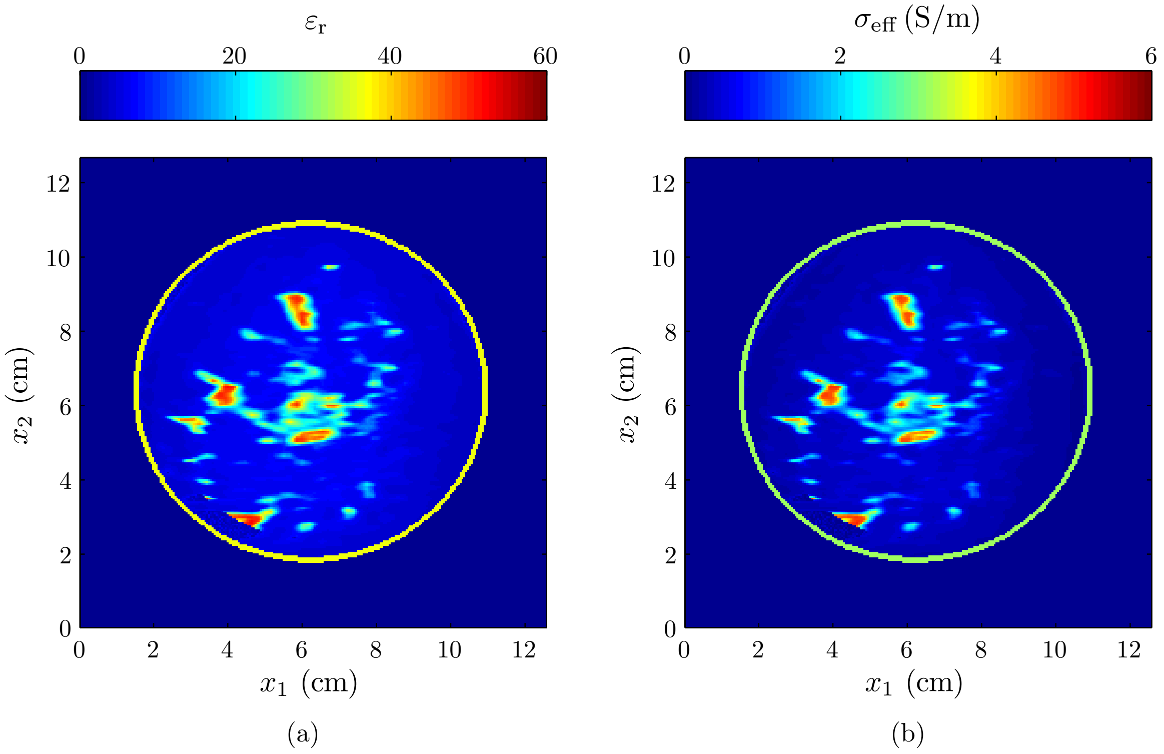

Fig. 3.3: Dielectric permittivity (a) and effective conductivity (b) of a transverse section of the numerical breast model for f = 5 GHz

We note that these models do not include tumors. One could superimpose synthetic tumors onto these models, by locally replacing a lump of tissue parameters with those of malignant tissue. However, we will assume that the tumor possesses no different dielectric properties than glandular or fibroconnective tissues, and thus simply assign a lump with a high conductivity as 'tumor'. This approach actually forms a worst-case scenario for a hyperthermia system, since tumor tissue has an approximately 10% higher conductivity than healthy glandular or fibroconnective tissues [31]. This property would actually improve the local heating potential. However, in view of the feasibility of the treatment this in not a significant difference and can therefore be neglected.

We have selected three 'tumors' denoted as tumor A, tumor B and tumor C as indicated in Fig. 3.4a. The selection of the tumors has been done by considering the conductivity pattern for $f = 5$ GHz and selecting a lump of tissue which has a conductivity higher than 1.7 S/m. The remaining tissue is then classified as 'healthy' except for the skin layer and, of course, the selected tumor. This results in a decomposition as shown in Fig. 3.4b.

Finally, we notice that the investigated configuration has been covered. We have discussed the two-dimensional model that is representative for the proposed configuration, together with a realistic breast model that describes the electromagnetic properties of the female breast. This concludes the set-up for computing the fields, which will be discussed in the next chapter.

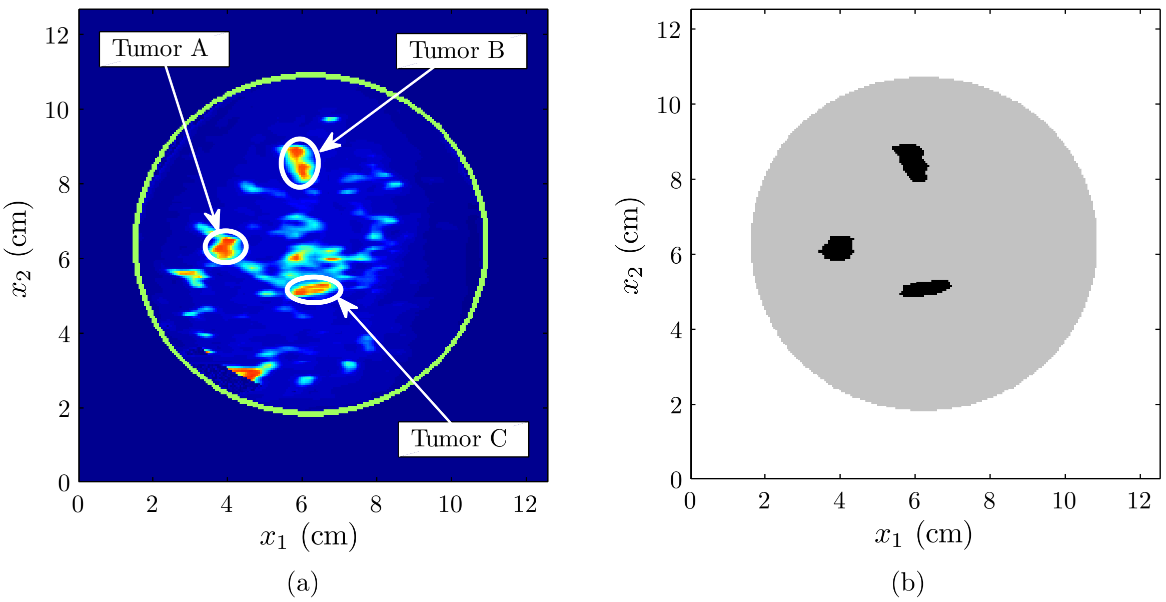

(a)

(b)

Fig. 3.4: Three ‘tumors’ selected in the healthy breast model (a) and the resulting domain decomposition (b)

Chapter 4

The forward scattering problem

The forward scattering problem assumes the incident field $\boldsymbol{E}^{\text{inc}}$ and material contrast χ to be known, and has the goal to obtain the total field inside the computational domain $\mathcal{D}$. The exact solution to the forward scattering problem can only be obtained in some specific configurations. In a realistic scattering scenario one can at most *approximate* the total field inside the domain of computation. Hence, using an iterative approach is likely to be most fruitful. The conjugate gradient scheme that we will use here is known as a simple, stable and efficient iterative method for solving dielectric scattering problems.

In the beginning of this chapter we will present the integral equation governing our forward scattering problem. Then we will treat the discretization of the computational domain and write the forward scattering problem in operator notation. We will close this chapter by describing the conjugate gradient method for solving the forward scattering problem. More information on the conjugate gradient method can be found in [46, 47].

From this point on, we will drop the $\hat{}$ notation, ω dependencies and the $^{\text{sct}}$ superscripts for improved readability.

4.1 The electric field integral equation

We will first simplify the integral equations for the electromagnetic field in Eqs. (2.68) and (2.69). Since the material in our configuration shows no contrast in its magnetic properties, which implies $\chi_{\text{m}} = 0$ and $\boldsymbol{F} = 0$, the set of coupled integral equations uncouples and one only needs to solve

$$\boldsymbol{E}^{\text{inc}} = \boldsymbol{E} - (k_{\text{b}}^2 + \nabla\nabla\cdot)\boldsymbol{A} \tag{4.1}$$

also known as the Electric Field Integral Equation (EFIE), where k_{b} is the complex wavenumber in the background medium with $\text{Im}\{k_{\text{b}}\} \leq 0$. The vector potential $\boldsymbol{A}$ is defined as

$$\boldsymbol{A}(\boldsymbol{x}) = \int\limits_{\boldsymbol{x}'\in\mathcal{D}} g(\boldsymbol{x}-\boldsymbol{x}')\chi(\boldsymbol{x}')\boldsymbol{E}(\boldsymbol{x}')\text{d}V \tag{4.2}$$

where χ denotes the relative electric contrast with respect to the background as

$$\chi(\boldsymbol{x}) = \frac{\varepsilon(\boldsymbol{x}) - \varepsilon_{\mathrm{b}}}{\varepsilon_{\mathrm{b}}} \tag{4.3}$$

and g denotes the Green's function which is expressed as

$$g(\boldsymbol{x}) = -\frac{\mathrm{j}}{4} H_0^{(2)}(k_{\mathrm{b}}|\boldsymbol{x}|)\,. \tag{4.4}$$

More details on the derivation of the two-dimensional Green's function can be found in Appendix B.

Once the electric field has been found, the magnetic field can be directly computed as

$$\boldsymbol{H} = \boldsymbol{H}^{\mathrm{inc}} + \mathrm{j}\omega\varepsilon_{\mathrm{b}} \nabla \times \boldsymbol{A} \tag{4.5}$$

however, we do not need to compute this quantity in our investigation.

We note that the Green's function that appears in the integrand of the vector potential $\boldsymbol{A}$ is singular for $\boldsymbol{x} = \boldsymbol{x}'$. This singularity poses a challenge when evaluating the convolution integral. This challenge will be dealt with later in this chapter.

Before discussing the discretization procedure, we will first rewrite the EFIE in terms of its components

$$E_\kappa^{\mathrm{inc}} = E_\kappa - k_{\mathrm{b}}^2 A_\kappa - B_\kappa\,, \quad \text{for } \kappa \in \{1, 2\} \tag{4.6}$$

where A_κ is the vector potential and B_κ is the gradient divergence operator acting on the vector potential, i.e.

$$B_\kappa = \partial_\kappa[\partial_1 A_1 + \partial_2 A_2]\,, \quad \text{for } \kappa \in \{1, 2\}\,. \tag{4.7}$$

4.2 Discretization

In order to numerically solve the EFIE we need to reduce the problem to a finite-dimensional approximation of the problem, which can then be solved on a computer. This process is called discretization.

First we assume that the computational domain $\mathcal{D}$ is bounded along the x_1- and x_2-direction. We then divide this domain in rectangular subdomains $\mathcal{D}_{m,n}$ that have a yet unspecified size of Δx_1 in the x_1-direction and Δx_2 in the x_2-direction. While doing this, we extend the computational domain such that the final discretized domain is rectangular in shape. The number of partitions in the x_1-direction is then denoted by M and the number of partitions in the x_2-direction is denoted by N. We can write $\mathcal{D}$ as the union of all subdomains, viz.

$$\mathcal{D} = \bigcup_{m=1}^{M} \bigcup_{n=1}^{N} \mathcal{D}_{m,n} \tag{4.8}$$

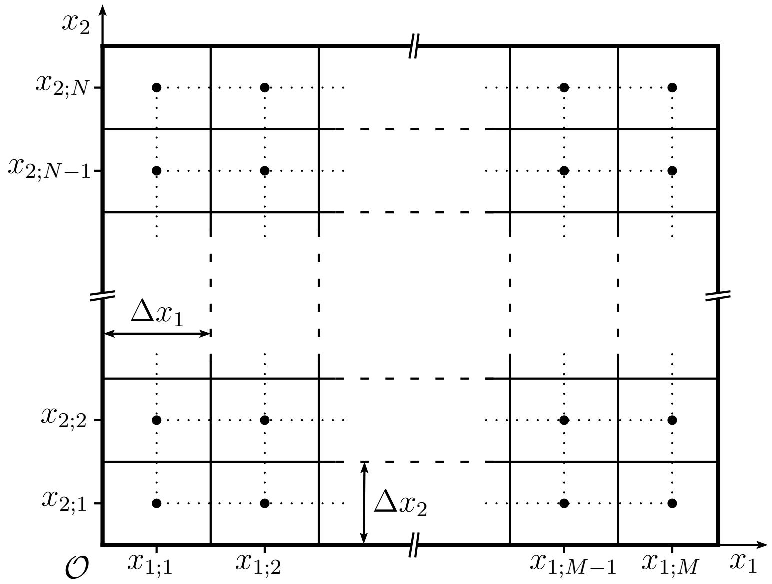

Fig. 4.1: The computational domain $\mathcal{D}$ divided into rectangular subdomains $\mathcal{D}_{m,n}$

where

$$\begin{aligned} \mathcal{D}_{m,n} = \{\, \boldsymbol{x} \in \mathbb{R}^2 : \ & |x_1 - x_{1;m}| < \tfrac{\Delta x_1}{2} \\ & |x_2 - x_{2;n}\,| < \tfrac{\Delta x_2}{2} \,\} \\ m = 1, \ldots, M, \ \ & n = 1, \ldots, N \end{aligned} \tag{4.9}$$

denotes the subdomain with center point $\boldsymbol{x}_{m,n}$, defined as

$$\boldsymbol{x}_{m,n} = \mathbf{i}_1 x_{1;m} + \mathbf{i}_2 x_{2;n} \tag{4.10}$$

of which the x_1- and x_2-coordinates are

$$x_{1;m} = x_{1;0} + (m - \tfrac{1}{2})\Delta x_1\,, \quad m = 1, \ldots, M \tag{4.11}$$

$$x_{2;n} = x_{2;0} + (n - \tfrac{1}{2})\Delta x_2\,, \quad n = 1, \ldots, N \tag{4.12}$$

where $x_{1;0}$ represents the lower x_1-bound of the computational domain $\mathcal{D}$, and $x_{2;0}$ represents its lower x_2-bound. In our case, we will simply set $x_{1;0} = x_{2;0} = 0$. The resulting discretized domain is illustrated in Fig. 4.1.

Because of the spatial differentiations that appear in Eq. (4.7) we choose to have the boundary of $\mathcal{D}$ lying completely outside the object. In other words, we have

$$\chi_{1,n} = \chi_{M,n} = 0 \quad \forall \ \ n \tag{4.13}$$

$$\chi_{m,1} = \chi_{m,N} = 0 \quad \forall \ \ m\,. \tag{4.14}$$

Now that we have discretized our computational domain, we can discretize the physical quantities related to our configuration. The first physical quantity that we discretize is the contrast χ. Within each subdomain $\mathcal{D}_{m,n}$, we replace χ by its value at the center point $\boldsymbol{x}_{m,n}$ and, hence, this is referred to as the midpoint approximation. The resulting discrete contrast is written as $\chi_{m,n}$.

In the same way we discretize the following quantities

$$E_{\kappa;m,n} = E_\kappa(\boldsymbol{x}_{m,n}) \tag{4.15}$$

$$E^{\text{inc}}_{\kappa;m,n} = E^{\text{inc}}_\kappa(\boldsymbol{x}_{m,n}) \tag{4.16}$$

$$A_{\kappa;m,n} = A_\kappa(\boldsymbol{x}_{m,n}) \tag{4.17}$$

$$B_{\kappa;m,n} = B_\kappa(\boldsymbol{x}_{m,n}) \tag{4.18}$$

of which the latter two will be described in the following two subsections. With these definitions we can write the EFIE, Eq. (4.6), in discretized and component-wise form as

$$E^{\text{inc}}_{\kappa;m,n} = E_{\kappa;m,n} - k_{\text{b}}^2 A_{\kappa;m,n} - B_{\kappa;m,n}\,, \quad \text{for } \kappa \in \{1,2\}\,. \tag{4.19}$$

It's worth dedicating a final note to the size of the subdomains, or discretization step size. It is common to relate this size to the wavelength. This idea originates from Shannon's theorem which states that at least two samples per period or wavelength are necessary in order to detect the corresponding frequency. This detection limit is however not sufficient for *approximating* a function. It is therefore more common to use approximately six to ten subdomains per wavelength [35]. In Chapter 6 we investigate the effect of three discretization step sizes.

4.2.1 The gradient divergence term

The first term of the EFIE that we will discretize is B_κ given in Eq. (4.20). We discretize it using the finite difference approximation of partial derivatives, viz.

$$B_{\kappa;m,n} = \sum_{\nu=1}^{2} \sum_{p=0}^{M+1} \sum_{q=0}^{N+1} a^{(\kappa,\nu)}_{m,n,p,q} A_{\nu;p,q}\,, \quad \text{for } \kappa \in \{1,2\} \tag{4.20}$$

where

$$a^{(1,1)}_{m,n,p,q} = \frac{(\delta_{p,m+1} - 2\delta_{p,m} + \delta_{p,m-1})\delta_{q,n}}{(\Delta x_1)^2} \tag{4.21}$$

$$\begin{aligned} a^{(1,2)}_{m,n,p,q} &= a^{(2,1)}_{m,n,p,q} \\ &= \frac{(\delta_{p,m-1} - \delta_{p,m+1})(\delta_{q,n-1} - \delta_{q,n+1})}{4\Delta x_1 \Delta x_2} \end{aligned} \tag{4.22}$$

$$a^{(2,2)}_{m,n,p,q} = \frac{(\delta_{q,n+1} - 2\delta_{q,n} + \delta_{q,n-1})\delta_{p,m}}{(\Delta x_2)^2} \tag{4.23}$$

in which

$$\delta_{m,n} = \begin{cases} 1 & \forall \quad m = n \\ 0 & \forall \quad m \neq n \end{cases} \tag{4.24}$$

defines the Kronecker delta function.

We can write $B_{\kappa;m,n}$ directly as

$$B_{1;m,n} = \frac{A_{1;m-1,n} - 2A_{1;m,n} + A_{1;m+1,n}}{(\Delta x_1)^2} + \frac{A_{2;m-1,n-1} - A_{2;m-1,n+1} - A_{2;m+1,n-1} + A_{2;m+1,n+1}}{4\Delta x_1 \Delta x_2} \tag{4.25}$$

$$B_{2;m,n} = \frac{A_{2;m,n-1} - 2A_{2;m,n} + A_{2;m,n+1}}{(\Delta x_2)^2} + \frac{A_{1;m-1,n-1} - A_{1;m+1,n-1} - A_{1;m-1,n+1} + A_{1;m+1,n+1}}{4\Delta x_1 \Delta x_2} . \tag{4.26}$$

This result has been justified by Kooij and van den Berg [25], who obtained the same results via Galerkin's method.

4.2.2 The vector potential term

Now the only step left is the discretization of the vector potential A_κ in Eq. (4.2). This step poses a specific challenge because of the singularity of the Green's function at $\boldsymbol{x}' = \boldsymbol{x}_{m,n}$. We deal with this singularity by replacing the vector potential with its weak form, that is its mean value over a circular domain with center point $\boldsymbol{x}_{m,n}$ and radius $\frac{1}{2}\Delta x = \frac{1}{2}\min(\Delta x_1, \Delta x_2)$.

We first write the weak form of the vector potential $A_{\kappa;m,n}$ as

$$\begin{aligned} A_{\kappa;m,n} &= \frac{4}{\pi(\Delta x)^2} \int\limits_{|\boldsymbol{x}''| < \frac{1}{2}\Delta x} A_\kappa(\boldsymbol{x}_{m,n} + \boldsymbol{x}'')\mathrm{d}V \\ &= \int\limits_{\boldsymbol{x}' \in \mathcal{D}} \left[\frac{4}{\pi(\Delta x)^2} \int\limits_{|\boldsymbol{x}''| < \frac{1}{2}\Delta x} g(\boldsymbol{x}_{m,n} - \boldsymbol{x}' + \boldsymbol{x}'')\mathrm{d}V \right] \chi(\boldsymbol{x}')E_\kappa(\boldsymbol{x}')\mathrm{d}V \qquad (4.27) \\ &\approx \Delta x_1 \Delta x_2 \sum_{m'=1}^{M} \sum_{n'=1}^{N} \mathcal{G}(\boldsymbol{x}_{m,n} - \boldsymbol{x}_{m',n'})\chi(\boldsymbol{x}_{m',n'})E_\kappa(\boldsymbol{x}_{m',n'})\mathrm{d}V \qquad (4.28) \end{aligned}$$

where we have applied a midpoint approximation on the convolution integral and we see that by interchanging the integration order, this weakening procedure is actually transferred onto the Green's function. What remains is computing its weak form $\mathcal{G}$, i.e. the bracketed part of Eq. (4.27) with $\boldsymbol{x}' = \boldsymbol{x}_{m',n'}$, which is described in more detail in Appendix C. The result of this computation is given by

$$\mathcal{G}(\boldsymbol{x}_{m,n} - \boldsymbol{x}_{m',n'}) = \begin{cases} -\dfrac{\mathrm{j}}{k_\mathrm{b}\Delta x}\left[H_1^{(2)}(\frac{1}{2}k_\mathrm{b}\Delta x) - \dfrac{4\mathrm{j}}{\pi k_\mathrm{b}\Delta x} \right] & \forall \;\; \boldsymbol{x}_{m,n} = \boldsymbol{x}_{m',n'} \\ -\dfrac{\mathrm{j}}{k_\mathrm{b}\Delta x} J_1(\frac{1}{2}k_\mathrm{b}\Delta x) H_0^{(2)}(k_\mathrm{b}|\boldsymbol{x}_{m,n} - \boldsymbol{x}_{m',n'}|) & \forall \;\; \boldsymbol{x}_{m,n} \neq \boldsymbol{x}_{m',n'} . \end{cases} \tag{4.29}$$

After dealing with this singularity we write the discrete vector potential as

$$A_{\kappa;m,n} = \Delta x_1 \Delta x_2 \sum_{m'=1}^{M} \sum_{n'=1}^{N} \mathcal{G}_{m-m',n-n'} \chi_{m',n'} E_{\kappa;m',n'} \,, \quad \text{for } \kappa \in \{1,2\} \tag{4.30}$$

where we have used the notation

$$\mathcal{G}_{m-m',n-n'} = \mathcal{G}(\boldsymbol{x}_{m,n} - \boldsymbol{x}_{m',n'}) \,. \tag{4.31}$$

We note that Eq. (4.30) is a discrete convolution in m' and n', which can be efficiently computed by using a Fast Fourier Transform (FFT) routine. More information on this procedure can be found in [46].

4.3 Operator notation

Before we proceed with the conjugate gradient method for solving the discretized EFIE, we will need to define some of its components. Among these are the operator, the inner product and norm on the computational domain $\mathcal{D}$, and the definition of the adjoint operator.

4.3.1 The operator L

From the discretization of the vector potential A_κ and its gradient divergence term B_κ we see that the EFIE forms a linear system of equations for $E_{\kappa;m,n}$. The behaviour of this system of equations can be described by the operator $\mathbf{L}$ acting upon $\boldsymbol{E}$ as

$$(\mathbf{L}\boldsymbol{E})_{\kappa;m,n} = E_{\kappa;m,n} - k_{\mathrm{b}}^2 A_{\kappa;m,n} - B_{\kappa;m,n} \tag{4.32}$$

where $\kappa \in \{1,2\}$, $m = 1,\ldots,M$ and $n = 1,\ldots,N$.

We can thus write the EFIE as

$$E^{\mathrm{inc}}_{\kappa;m,n} = (\mathbf{L}\boldsymbol{E})_{\kappa;m,n} \tag{4.33}$$

or in vector notation

$$\boldsymbol{E}^{\mathrm{inc}} = \mathbf{L}\boldsymbol{E} \quad \forall \quad \boldsymbol{x} \in \mathcal{D} \,. \tag{4.34}$$

4.3.2 Inner products and norms

Before we can define the adjoint operator, we need to define the L_2-inner product and the L_2-norm. For complex scalar quantities u and v, the inner product is written as

$$\langle u \,, v \rangle = u\overline{v} \tag{4.35}$$

where the bar denotes complex conjugation. The squared norm for a complex scalar quantity is related to the inner product as

$$\|u\|^2 = \langle u\,, u\rangle = |u|^2 \,. \tag{4.36}$$

For complex scalar functions of $\boldsymbol{x}$, the L_2-inner product on the computational domain $\mathcal{D}$ is defined as

$$\langle u\,, v\rangle_{\mathcal{D}} = \int\limits_{\boldsymbol{x}\in\mathcal{D}} \langle u(\boldsymbol{x})\,, v(\boldsymbol{x})\rangle \mathrm{d}V = \int\limits_{\boldsymbol{x}\in\mathcal{D}} u(\boldsymbol{x})\overline{v(\boldsymbol{x})}\mathrm{d}V \tag{4.37}$$

for continuous functions and

$$\langle u\,, v\rangle_{\mathcal{D}} = \Delta x_1 \Delta x_2 \sum_{m=1}^{M}\sum_{n=1}^{N} u_{m,n}\overline{v_{m,n}} \tag{4.38}$$

for discretized functions. For both types of functions the squared L_2-norm is related to L_2-inner product by

$$\|u\|^2_{\mathcal{D}} = \langle u\,, u\rangle_{\mathcal{D}} \,. \tag{4.39}$$

Vectorial quantities

For complex vectorial quantities in $\mathbb{C}^2$, the inner product is defined as

$$\langle \boldsymbol{u}\,, \boldsymbol{v}\rangle = \boldsymbol{u}\cdot\overline{\boldsymbol{v}} = \sum_{\kappa=1}^{2} u_\kappa \overline{v_\kappa} \tag{4.40}$$

and the squared norm as

$$\|\boldsymbol{u}\|^2 = \langle \boldsymbol{u}\,, \boldsymbol{u}\rangle \,. \tag{4.41}$$

For complex vectorial functions of $\boldsymbol{x}$, the L_2-inner product on the computational domain $\mathcal{D}$ is defined as

$$\langle \boldsymbol{u}\,, \boldsymbol{v}\rangle_{\mathcal{D}} = \int\limits_{\boldsymbol{x}\in\mathcal{D}} \langle \boldsymbol{u}(\boldsymbol{x})\,, \boldsymbol{v}(\boldsymbol{x})\rangle \mathrm{d}V = \int\limits_{\boldsymbol{x}\in\mathcal{D}} \sum_{\kappa=1}^{2} u_\kappa(\boldsymbol{x})\overline{v_\kappa(\boldsymbol{x})}\mathrm{d}V \tag{4.42}$$

for continuous functions and

$$\langle \boldsymbol{u}\,, \boldsymbol{v}\rangle_{\mathcal{D}} = \Delta x_1 \Delta x_2 \sum_{\kappa=1}^{2}\sum_{m=1}^{M}\sum_{n=1}^{N} u_{\kappa;m,n}\overline{v_{\kappa;m,n}} \tag{4.43}$$

for discretized functions. For both the squared norm is written as

$$\|\boldsymbol{u}\|^2_{\mathcal{D}} = \langle \boldsymbol{u}\,, \boldsymbol{u}\rangle_{\mathcal{D}} \,. \tag{4.44}$$

4.3.3 The adjoint operator $\mathbf{L}^\star$

The adjoint operator $\mathbf{L}^\star$ is defined through the relation

$$\langle \boldsymbol{r}\,, \mathbf{L}\boldsymbol{E}\rangle_{\mathcal{D}} = \langle \mathbf{L}^\star \boldsymbol{r}\,, \boldsymbol{E}\rangle_{\mathcal{D}}\,. \tag{4.45}$$

By substituting Eq. (4.32) in the left hand side of the latter equation and rearranging the summations of the inner product, the adjoint operator can be found as

$$(\mathbf{L}^\star \boldsymbol{r})_{\kappa;p,q} = r_{\kappa;p,q} - \Delta x_1 \Delta x_2\, \overline{\chi}_{p,q} \sum_{p'=0}^{M+1} \sum_{q'=0}^{N+1} \overline{\mathcal{G}}_{p-p',q-q'} F_{\kappa;p',q'} \tag{4.46}$$

for $\kappa \in \{1,2\}$, $p = 1,\dots,M$ and $q = 1,\dots,N$, in which

$$F_{\kappa;p,q} = k_{\mathrm{b}}^2 r_{\kappa;p,q} + \sum_{\nu=1}^{2} \sum_{m=1}^{M} \sum_{n=1}^{N} a^{(\kappa,\nu)}_{m,n,p,q} r_{\nu;m,n} \tag{4.47}$$

where the definition of $a^{(\kappa,\nu)}_{m,n,p,q}$ can be found in Eqs. (4.21)–(4.23).

Since p' ranges from 0 to $M+1$ and q' from 0 to $N+1$, and the support of $a^{(\kappa,\nu)}_{m,n,p,q}$ equals three, we need to set

$$r_{\kappa;p,q} = 0\,, \quad \text{for } p = -1, 0, M+1, M+2 \quad \forall\ q \tag{4.48}$$

$$r_{\kappa;p,q} = 0\,, \quad \text{for } q = -1, 0, N+1, N+2 \quad \forall\ p \tag{4.49}$$

for $\kappa \in \{1,2\}$ in order to obtain this expression for the adjoint operator. We note that the adjoint operator $\mathbf{L}^\star$ contains spatial convolutions just like the operator $\mathbf{L}$, which can be efficiently computed with the Fast Fourier Transform (FFT) routine.

4.4 The conjugate gradient method

We will now describe the components of the conjugate gradient method. The starting point for this method is the EFIE. For a line-source indexed by $s = 1,\dots,S$, we will write the incident field as $\boldsymbol{E}_s^{\mathrm{inc}}$. The field resulting from $\boldsymbol{E}_s^{\mathrm{inc}}$ is then denoted as $\boldsymbol{E}_s$. Since Maxwell's equations are linear and the electromagnetic field is additive, we have S linearly independent equations that need to be evaluated on the computational domain, viz.

$$\boldsymbol{E}_s^{\mathrm{inc}} = \mathbf{L}\boldsymbol{E}_s\,, \quad \text{for } s = 1,\dots,S\,. \tag{4.50}$$

The total field with simultaneous illumination is then written as

$$\boldsymbol{E} = \sum_{s=1}^{S} \boldsymbol{E}_s\,, \quad \text{for } s = 1,\dots,S\,. \tag{4.51}$$

We could also sum all incident fields and then perform the conjugate gradient method in order to approximate the total field, but we choose this approach in view of the focussing algorithm. This way, the computation of the electromagnetic fields and the optimization of source amplitudes and phases are completely separated routines.

4.4.1 Local and global residual errors

The local residual errors $\boldsymbol{r}_s$ are defined as the difference between the left- and right-hand side of Eq. (4.1) and can be written as

$$\boldsymbol{r}_s = \boldsymbol{E}_s^{\text{inc}} - \mathbf{L}\boldsymbol{E}_s\,, \quad \text{for } s = 1, \ldots, S\,. \tag{4.52}$$

The local residual errors are vector valued functions of $\boldsymbol{x}$, and thus represents a multitude of residual errors. These can be compressed into one global error per source using the square norm on the computational domain as defined in Eq. (4.44). By normalizing this global squared error we construct the cost functional as

$$\mathcal{F}_{\mathcal{D};s}(\boldsymbol{E}_s) = \frac{\|\boldsymbol{r}_s\|_{\mathcal{D}}^2}{\|\boldsymbol{E}_s^{\text{inc}}\|_{\mathcal{D}}^2} = \frac{\|\boldsymbol{E}_s^{\text{inc}} - \mathbf{L}\boldsymbol{E}_s\|_{\mathcal{D}}^2}{\|\boldsymbol{E}_s^{\text{inc}}\|_{\mathcal{D}}^2}\,, \quad \text{for } s = 1, \ldots, S \tag{4.53}$$

where we have

$$\mathcal{F}_{\mathcal{D};s}(\mathbf{0}) = 1 \qquad \text{and} \qquad \mathcal{F}_{\mathcal{D};s}(\boldsymbol{E}_s^{\text{exact}}) = 0\,, \quad \text{for } s = 1, \ldots, S\,. \tag{4.54}$$

We also introduce a global cost functional which indicates the total convergence of the scheme:

$$\mathcal{F}_{\mathcal{D}}(\boldsymbol{E}_s) = \frac{\sum\limits_{s=1}^{S} \|\boldsymbol{r}_s\|_{\mathcal{D}}^2}{\sum\limits_{s=1}^{S} \|\boldsymbol{E}_s^{\text{inc}}\|_{\mathcal{D}}^2} = \frac{\sum\limits_{s=1}^{S} \|\boldsymbol{E}_s^{\text{inc}} - \mathbf{L}\boldsymbol{E}_s\|_{\mathcal{D}}^2}{\sum\limits_{s=1}^{S} \|\boldsymbol{E}_s^{\text{inc}}\|_{\mathcal{D}}^2}\,. \tag{4.55}$$

4.4.2 Minimizing the cost functional

The conjugate gradient method consists of an algorithm that iteratively updates the electric field such that the values of the cost functionals $\mathcal{F}_{\mathcal{D};s}$ decrease. Consequently, the global cost functional $\mathcal{F}_{\mathcal{D}}$ also decreases. By doing so, a sequence of the electric fields $\{\boldsymbol{E}_{s,n}\}$ for $n = 0, 1, 2, \ldots$ is constructed where n denotes the iteration number. This sequence is constructed in the following manner.

Starting value for $n = 0$

The algorithm needs to be equipped with an initial guess for the electric fields in order to build the sequence of updates. As a starting point one can take an approximation of the electric field, or an arbitrary field like the incident electric field or simply a zero valued electric field. We choose the latter option and write

$$\boldsymbol{E}_{s,0} = \mathbf{0}\,, \quad \text{for } s = 1, \ldots, S \tag{4.56}$$

which yields the initial local residual error

$$\boldsymbol{r}_{s,0} = \boldsymbol{E}_s^{\text{inc}}\,, \quad \text{for } s = 1, \ldots, S\,. \tag{4.57}$$

Updating the electric fields

We update the total electric field for source s as

$$\boldsymbol{E}_{s,n} = \boldsymbol{E}_{s,n-1} + \alpha_{s,n}\boldsymbol{e}_{s,n} \quad \forall \quad n \geq 1 \tag{4.58}$$

where $\alpha_{s,n}$ is a scalar valued weighting parameter and the update direction $\boldsymbol{e}_{s,n}$ is a vector valued function of $\boldsymbol{x}$.

By iteratively updating the electric fields, the sequence of local residual errors is found to be

$$\boldsymbol{r}_{s,n} = \boldsymbol{r}_{s,n-1} - \alpha_{s,n}\mathbf{L}\boldsymbol{e}_{s,n}\,, \quad \text{for } s = 1,\ldots,S \tag{4.59}$$

and hence, the cost functionals in the n^{th} iteration can be written as

$$\mathcal{F}_{\mathcal{D};s,n}(\boldsymbol{E}_{s,n}) = \eta_{\mathcal{D};s}\|\boldsymbol{r}_{s,n}\|^2_{\mathcal{D}}\,, \quad \text{for } s = 1,\ldots,S \tag{4.60}$$

where

$$\eta_{\mathcal{D};s} = \left(\|\boldsymbol{E}^{\text{inc}}_s\|^2_{\mathcal{D}}\right)^{-1}, \quad \text{for } s = 1,\ldots,S \tag{4.61}$$

denotes the normalization factor.

Convergence

It has been noted in [22] that for the forward scattering problem the conjugate gradient method *always* converges to the global minimum of the cost functional, which is in our case $\boldsymbol{E}^{\text{exact}}_s$. This property assures that the algorithm is stable. We note that, due to the finite number of iterations, residual errors in the total field will always remain. In other words, $\boldsymbol{E}^{\text{exact}}_s$ can't be obtained. However, we can choose to continue improving the electric fields until a satisfactory quality is reached.

When all cost functionals have reduced to a satisfactory small value, depending on the desired quality of our approximation, the algorithm is said to have reached convergence or has converged. We will take the global cost functional as a measure for the overall quality of the approximation. We consider a normalized global squared error of $1\cdot 10^{-10}$ to be satisfactory. We also limit the number of iterations to 2048 such that the method quits the process in case the convergence rate is very low.

4.4.3 Update direction

A self evident candidate for the update direction $\boldsymbol{e}_{s,n}$ for source s is the negative gradient of the cost functional $\mathcal{F}_{\mathcal{D};s}$ with respect to the changes in the electric field $\boldsymbol{E}_s$, evaluated in $\boldsymbol{E}_{s,n-1}$. It provides the direction in which the decrease of the cost functional is maximal. Hence, the cost functional is guaranteed to decrease when a small step is taken in this direction.

In order to find an expression for the gradient of the cost functional, we linearly parameterize the electric fields as $\boldsymbol{E}_s = \boldsymbol{E}_{s,n-1} + \tau \boldsymbol{e}_{s,n}$ and we differentiate with respect to τ. This is written as

$$\partial \boldsymbol{e}_{s,n} = \frac{\partial}{\partial \tau} \mathcal{F}_{\mathcal{D};s,n-1}(\boldsymbol{E}_{s,n-1} + \tau \boldsymbol{e}_{s,n}) \,. \tag{4.62}$$

The gradient can be computed via the Fréchet derivative, which is implicitly defined through the following relation [2]

$$\lim_{\|\boldsymbol{h}\|_{\mathcal{D}} \to 0} \mathcal{F}_{\mathcal{D};s}(\boldsymbol{E}_{s,n-1} + \boldsymbol{h}) - \mathcal{F}_{\mathcal{D};s}(\boldsymbol{E}_{s,n-1}) - \mathrm{Re}\langle \partial \boldsymbol{e}_{s,n} \,, \boldsymbol{h} \rangle_{\mathcal{D}} = 0 \,. \tag{4.63}$$

After substituting $\boldsymbol{h} = \tau \boldsymbol{e}_{s,n}$ and taking the limit $\tau \to 0$ instead, we find the relation

$$\begin{aligned} \mathrm{Re}\langle \partial \boldsymbol{e}_{s,n} \,, \boldsymbol{e}_{s,n} \rangle_{\mathcal{D}} &= \lim_{\tau \to 0} \frac{\mathcal{F}_{\mathcal{D};s}(\boldsymbol{E}_{s,n-1} + \tau \boldsymbol{e}_{s,n}) - \mathcal{F}_{\mathcal{D};s}(\boldsymbol{E}_{s,n-1})}{\tau} \\ &= \eta_{\mathcal{D};s} \lim_{\tau \to 0} \frac{\|\boldsymbol{r}_{s,n-1} - \tau \mathbf{L} \boldsymbol{e}_{s,n}\|_{\mathcal{D}}^2 - \|\boldsymbol{r}_{s,n-1}\|_{\mathcal{D}}^2}{\tau} \\ &= \eta_{\mathcal{D};s} \lim_{\tau \to 0} \frac{-2\tau \mathrm{Re}\langle \boldsymbol{r}_{s,n-1} \,, \mathbf{L}\boldsymbol{e}_{s,n} \rangle_{\mathcal{D}} + \tau^2 \|\mathbf{L}\boldsymbol{e}_{s,n}\|_{\mathcal{D}}^2}{\tau} \\ &= -2\eta_{\mathcal{D};s} \mathrm{Re}\langle \mathbf{L}^\star \boldsymbol{r}_{s,n-1} \,, \boldsymbol{e}_{s,n} \rangle_{\mathcal{D}} \end{aligned} \tag{4.64}$$

from which we see that we can recognize the gradient of the cost functional from Eq. (4.64) as

$$\partial \boldsymbol{e}_{s,n} = -\mathbf{L}^\star \boldsymbol{r}_{s,n-1} \tag{4.65}$$

where we have excluded the scalar factors, since we will scale the update direction by $\alpha_{s,n}$ later on.

Taking the negative gradient as an update direction is known as the gradient descent method, or steepest descent method. These update directions can be improved however by taking the conjugate gradient direction, given by

$$\boldsymbol{e}_{s,n} = \begin{cases} -\partial \boldsymbol{e}_{s,n} & \forall \;\; n = 1 \\ -\partial \boldsymbol{e}_{s,n} + \gamma_{s,n} \boldsymbol{e}_{s,n-1} & \forall \;\; n > 1 \end{cases} \tag{4.66}$$

with

$$\gamma_{s,n} = \begin{cases} \dfrac{\langle \partial \boldsymbol{e}_{s,n} \,, \partial \boldsymbol{e}_{s,n} - \partial \boldsymbol{e}_{s,n-1} \rangle_{\mathcal{D}}}{\|\partial \boldsymbol{e}_{s,n-1}\|_{\mathcal{D}}^2} & \text{[Polak-Ribière]} \\[2ex] \dfrac{\|\partial \boldsymbol{e}_{s,n}\|_{\mathcal{D}}^2}{\|\partial \boldsymbol{e}_{s,n-1}\|_{\mathcal{D}}^2} & \text{[Fletcher-Reeves]} \,. \end{cases} \tag{4.67}$$

Finally, we note that due to the orthogonality relation between the gradients which is proven in [5] and gives $\langle \partial \boldsymbol{e}_{s,n} \,, \partial \boldsymbol{e}_{s,p} \rangle_{\mathcal{D}} = 0$ for $n \neq p$, the Polak-Ribière and Fletcher-Reeves conjugate gradient directions are actually identical here.

4.4.4 Weighting parameter

Now that we have obtained the direction in which the electric field needs to be updated, we only need to determine the magnitude of this update, which is represented by the parameter $\alpha_{s,n}$. The optimal weight is found by minimizing the cost functional in the n^{th} iteration for a variation in $\alpha_{s,n}$. By substituting Eq. (4.59) in Eq. (4.60) and applying the conditions for an extreme point

$$\frac{\partial}{\partial \alpha_{s,n}} \mathcal{F}_{\mathcal{D};s,n}(\boldsymbol{E}_{s,n}) = 0 \tag{4.68}$$

we find by using the chain rule

$$2\langle \boldsymbol{r}_{s,n-1} - \alpha_{s,n} \mathbf{L}\boldsymbol{e}_{s,n} \, , -\mathbf{L}\boldsymbol{e}_{s,n} \rangle_{\mathcal{D}} = 0 \tag{4.69}$$

which leads to

$$\alpha_{s,n} = \frac{\langle \boldsymbol{r}_{s,n-1} \, , \mathbf{L}\boldsymbol{e}_{s,n} \rangle_{\mathcal{D}}}{\|\mathbf{L}\boldsymbol{e}_{s,n}\|^2_{\mathcal{D}}} = \frac{\|\partial \boldsymbol{e}_{s,n}\|^2_{\mathcal{D}}}{\|\mathbf{L}\boldsymbol{e}_{s,n}\|^2_{\mathcal{D}}} \, . \tag{4.70}$$

We conclude this subsection and chapter by noting that we have presented all elements that constitute the conjugate gradient method for solving the forward scattering problem. The performance of this method will be evaluated in Chapter 6. After computing the electric fields, an optimization routine can be used to determine the excitation amplitude and phase that optimize the power distribution for ablation of the tumor. This routine will be covered in the next chapter.

Chapter 5

Power optimization

So far, we have discussed the computation of the electromagnetic field in a female breast. Now, we will discuss the methods for computing the optimal phase and amplitude of each array element such that the power dissipation is optimized for thermal ablation.

After a general introduction of optimization we will introduce two eigenvalue methods. We conclude Chapter 5 by presenting a conjugate gradient scheme that optimizes a given power dissipation pattern in order to suppress hot spots in the healthy tissue.

5.1 General formulation

In general, optimization problems involve the maximization or minimization of a *real valued functional*, be it or not upon accounting for a number of *constraints*. The functional is defined on a generic S-dimensional set of *control variables* denoted as $\boldsymbol{a} = \{a_1, \ldots, a_S\}$. The set in which the optimum is searched for is referred to as the set of *admissible controls* U and it is, usually, a subset of the set in which $\boldsymbol{a}$ is defined, the extent of the subset being determined by the constraints. In the case no constraints are imposed, the optimization problem is referred to as *unconstrained optimization* and U is identical with the original S-dimensional space. With these notations, the optimization problems can be formally expressed as

$$\text{Maximize (or minimize)} \quad \mathcal{J}(\boldsymbol{a}) \quad \text{over } \boldsymbol{a} \in U\,. \tag{5.1}$$

In our case, we are modeling an antenna array which consists of S line-sources and, thus, the set U consists of the complex feeding vectors $\boldsymbol{a} = \{a_1, \ldots, a_S\} \in \mathbb{C}^S$.

The problem of optimization can be formulated as the search for the control parameter $\boldsymbol{a}_0 \in U$ for which $\mathcal{J}(\boldsymbol{a}_0)$ is an absolute maximum (or minimum) over U. For instance in case of a maximization problem, we can formulate the optimization problem as the search for $\boldsymbol{a}_0 \in U$ that satisfies

$$\mathcal{J}(\boldsymbol{a}_0) \geq \mathcal{J}(\boldsymbol{a}) \quad \forall \quad \boldsymbol{a} \in U\,. \tag{5.2}$$

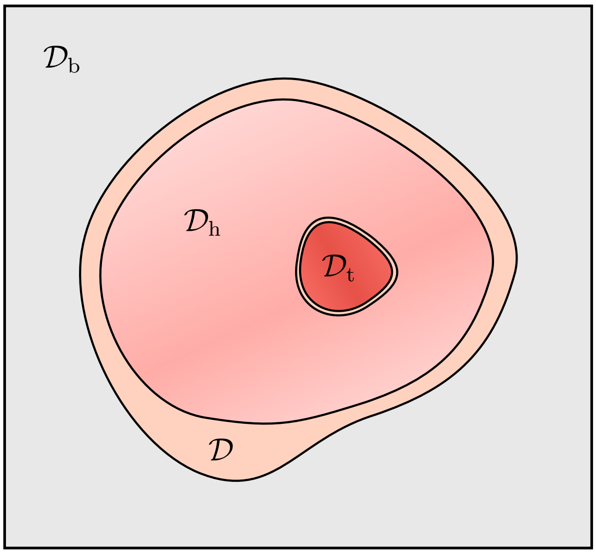

Fig. 5.1: The general decomposition of the object domain into a tumor domain and a healthy domain

In the formulation of the optimization problem, we will denote the subdomain that contains cancerous tissue as $\mathcal{D}_\mathrm{t}$ and the subdomain that contains healthy tissue as $\mathcal{D}_\mathrm{h}$. These domains are located inside the object domain $\mathcal{D}$ and are disjoint, i.e. $\mathcal{D}_\mathrm{t} \cap \mathcal{D}_\mathrm{h} = 0$. This is illustrated in Fig. 5.1.

5.2 Performance measures

The main component of an optimization method is a real valued functional the extremum of which is being computed. For this we assign the performance functional $\mathcal{J}$ that will relate the control parameter $\boldsymbol{a}$ to the performance index $\mathcal{J}(\boldsymbol{a})$. The functional will provide a measure for the effectiveness of the ablation treatment.

In essence, the performance of an ablation system is measured through the temperature distribution that is obtained. The optimization of this temperature distribution can be translated directly into a power optimization problem, for which a justification is given in Appendix A. This analysis gives rise to the goal expressed in Eq. (A.5), repeated here in slightly different notation

$$\text{Maximize} \quad \frac{\min\limits_{\boldsymbol{x} \in \mathcal{D}_\mathrm{t}} P_\mathrm{diss}(\boldsymbol{x})}{\max\limits_{\boldsymbol{x} \in \mathcal{D}_\mathrm{h}} P_\mathrm{diss}(\boldsymbol{x})} \tag{5.3}$$

where

$$P_\mathrm{diss}(\boldsymbol{x}) = \tfrac{1}{2}\sigma_\mathrm{eff}(\boldsymbol{x})\boldsymbol{E}(\boldsymbol{x})\cdot\boldsymbol{E}^*(\boldsymbol{x})\,. \tag{5.4}$$

Functionals used in optimization studies often include a certain norm to measure the quality of the result. In the optimization problem formulated in Eq. (5.3) one might suggest using an infinity norm to construct the performance functional, since it can measure the maximum value of certain functions. Unfortunately, it is difficult to assure that an optimization problem involving such a norm has a *unique* solution, if a solution exists at all.

There are however optimization problems for which the existence and uniqueness can be proven. This is the case in optimization problems that concern a *convex* subset U, and a *strictly convex* functional $\mathcal{J}$ [2].

We suggest using an L_2-norm as introduced in Chapter 4 to measure the quality of the result, since this norm is a strictly convex function of its input argument. The resulting problem can be interpreted as optimizing a *global* quantity like the total or the average dissipated power in a domain. Although local hotspots are not measured specifically through this norm, they are taken into account. In the rest of this study we will therefore consider optimizing *average* power densities only.

5.3 Eigenvalue methods

In this section we will discuss the first two methods that optimize the dissipated power distribution in the breast. The two eigenvalue methods presented in this paragraph have been introduced, though sometimes in a slightly different form, in numerous research projects on hyperthermia [4, 6, 24, 27, 38]. Both methods can be obtained using the Lagrange multiplier rule, which is extensively described in [2]. We will, however, derive them in a more straightforward way, which involves only elementary algebraic steps but essentially yields the same method.

5.3.1 Performance functionals

The main goal in ablative therapy is to maximize the power dissipation in the tumor. So, the first candidate functional that meets this demand can be formed by simply taking the average dissipated power in the tumor domain $\mathcal{D}_\mathrm{t}$. However, we need to constrain the input power in this case since it is directly related to this quantity. In fact, we should consider maximizing the *focussing* of the power into the tumor domain, which we can quantify as the average dissipated power in the tumor domain relative to the input power, which is proportional to the square norm of the feed vector $\boldsymbol{a}$. We thus define $\mathcal{J}_1$ as

$$\mathcal{J}_1(\boldsymbol{a}) = \frac{1}{\mathcal{A}_\mathrm{t}\|\boldsymbol{a}\|^2} \int\limits_{\boldsymbol{x}\in\mathcal{D}_\mathrm{t}} \sigma(\boldsymbol{x})\boldsymbol{E}(\boldsymbol{x})\cdot\boldsymbol{E}^*(\boldsymbol{x})\mathrm{d}V = \frac{1}{\mathcal{A}_\mathrm{t}} \frac{\langle\sigma\boldsymbol{E},\boldsymbol{E}\rangle_{\mathcal{D}_\mathrm{t}}}{\|\boldsymbol{a}\|^2} \tag{5.5}$$

where we used the inner product on the computational domain defined in Chapter 4, and

$$\mathcal{A}_{\mathrm{t}} = \int\limits_{\boldsymbol{x}\,\in\mathcal{D}_{\mathrm{t}}} \mathrm{d}V \tag{5.6}$$

denotes the size of the tumor. We note that this functional has the physical dimensions of W/m^3. One might hope that the power dissipated in healthy tissue would be indirectly minimized through the norm of the feeding vector $\boldsymbol{a}$. However, this goal is not incorporated in a very refined manner. In the second performance functional this is done more explicitly.

The second performance functional that we will investigate is closer to what we actually want to achieve. Next to maximizing the power dissipated in the tumor, we also need to constrain the power dissipated in the healthy tissue. We therefore define this functional as the ratio between the average power dissipation in the tumor tissue and the average power dissipation in the healthy tissue, viz.

$$\mathcal{J}_2 = \frac{\mathcal{A}_{\mathrm{h}}}{\mathcal{A}_{\mathrm{t}}} \frac{\langle \sigma \boldsymbol{E}, \boldsymbol{E} \rangle_{\mathcal{D}_{\mathrm{t}}}}{\langle \sigma \boldsymbol{E}, \boldsymbol{E} \rangle_{\mathcal{D}_{\mathrm{h}}}} \,. \tag{5.7}$$

We note that this functional has no physical dimensions.

Now we have defined two performance functionals that will lead us to two eigenvalue methods. In order to get there, we will present a matrix notation of the performance functionals.

5.3.2 Matrix notation

First we will write the performance functionals in matrix notation. The total field inside the breast is the sum of the fields excited by the sources individually, which are driven through the complex feeding vector $\boldsymbol{a}$. We write the total field as

$$\boldsymbol{E} = \sum_{p=1}^{S} a_p \boldsymbol{E}_p \tag{5.8}$$

where $\boldsymbol{E}_p$ denotes the field excited by the source with index p.

Using this expression for the total field, and the definition for the inner product, we can redefine the average power dissipation in an arbitrary region $\mathcal{D}$ with size $\mathcal{A}$ as defined in Eq. (5.6) as

$$\begin{aligned} \frac{1}{\mathcal{A}} \langle \sigma \boldsymbol{E}, \boldsymbol{E} \rangle_{\mathcal{D}} &= \frac{1}{\mathcal{A}} \int\limits_{\boldsymbol{x}\in\mathcal{D}} \sigma(\boldsymbol{x}) \boldsymbol{E}(\boldsymbol{x}) \cdot \boldsymbol{E}^*(\boldsymbol{x}) \mathrm{d}V \\ &= \frac{1}{\mathcal{A}} \sum_{q=1}^{S} \sum_{p=1}^{S} \int\limits_{\boldsymbol{x}\in\mathcal{D}} a_q^* \boldsymbol{E}_q^*(\boldsymbol{x}) \cdot \boldsymbol{E}_p(\boldsymbol{x}) a_p \sigma(\boldsymbol{x}) \mathrm{d}V \\ &= \boldsymbol{a}^{\mathrm{H}} \boldsymbol{\Xi}^{\mathcal{D}} \boldsymbol{a} \end{aligned} \tag{5.9}$$

where the $^{\mathrm{H}}$ superscript denotes conjugate transposition. The elements $\xi^{\mathcal{D}}_{p,q}$ of $\Xi^{\mathcal{D}}$ are defined as

$$\xi^{\mathcal{D}}_{p,q} = \frac{1}{\mathcal{A}} \int\limits_{\boldsymbol{x}\in\mathcal{D}} \boldsymbol{E}^*_q(\boldsymbol{x})\cdot\boldsymbol{E}_p(\boldsymbol{x})\sigma(\boldsymbol{x})\mathrm{d}V = \frac{1}{\mathcal{A}}\langle\sigma\boldsymbol{E}_p, \boldsymbol{E}_q\rangle_{\mathcal{D}}\,. \tag{5.10}$$

for $p = 1, \ldots, S$ and $q = 1, \ldots, S$. We note that the diagonal elements of $\Xi^{\mathcal{D}}$, e.g. $\xi^{\mathcal{D}}_{p,p}$, represent the average dissipated power in $\mathcal{D}$ due to the illumination by the source p. Off-diagonal elements, e.g. $\xi^{\mathcal{D}}_{p,q}$, can be interpreted as the average correlation in $\mathcal{D}$ between the field generated by the source p and the field generated by the source q, weighted by the conductivity profile in $\mathcal{D}$. We note that $\Xi^{\mathcal{D}}$ is intrinsically positive definite and hermitian, i.e. $\Xi^{\mathcal{D}}$ is equal to its conjugate transpose.

Using Eq. (5.9), we can write the first performance functional, Eq. (5.5), as

$$\mathcal{J}_1(\boldsymbol{a}) = \frac{\boldsymbol{a}^{\mathrm{H}}\Xi^{\mathcal{D}_\mathrm{t}}\boldsymbol{a}}{\boldsymbol{a}^{\mathrm{H}}\boldsymbol{a}} \tag{5.11}$$

and the second can be written as

$$\mathcal{J}_2(\boldsymbol{a}) = \frac{\boldsymbol{a}^{\mathrm{H}}\Xi^{\mathcal{D}_\mathrm{t}}\boldsymbol{a}}{\boldsymbol{a}^{\mathrm{H}}\Xi^{\mathcal{D}_\mathrm{h}}\boldsymbol{a}}\,. \tag{5.12}$$

5.3.3 Eigenvalue problem

The performance functionals in Eqs. (5.11) and (5.12) can be maximized by setting the following conditions for an extremum

$$\frac{\partial\mathcal{J}(\boldsymbol{a})}{\partial a_q} = 0\,, \quad \text{for } q = 1, 2, \ldots, S \tag{5.13}$$

and

$$\frac{\partial\mathcal{J}(\boldsymbol{a})}{\partial a^*_q} = 0\,, \quad \text{for } q = 1, 2, \ldots, S\,. \tag{5.14}$$

However, since our performance functionals are real valued, we only need to set one of these conditions.

First performance functional

We will start with our first performance functional. By applying Eq. (5.14) to Eq. (5.11) and using standard differentiation rules, we obtain

$$\frac{\partial\mathcal{J}_1(\boldsymbol{a})}{\partial a^*_q} = \frac{1}{\boldsymbol{a}^{\mathrm{H}}\boldsymbol{a}}\left[\sum_{p=1}^{S}\xi^{\mathcal{D}_\mathrm{t}}_{p,q}a_p - \mathcal{J}_1(\boldsymbol{a})a_q\right] = 0\,. \tag{5.15}$$

By assuming that $\boldsymbol{a}^{\mathrm{H}}\boldsymbol{a} \neq 0$ holds, we can write Eq. (5.15) in the matrix form

$$\Xi^{\mathcal{D}_\mathrm{t}}\boldsymbol{a} = \mathcal{J}_1(\boldsymbol{a})\boldsymbol{a} \tag{5.16}$$

which is easily recognized as a standard eigenvalue problem with eigenvalues $\mathcal{J}_1(\boldsymbol{a}_p)$, system matrix $\Xi^{\mathcal{D}_\mathrm{t}}$ and eigenvectors $\boldsymbol{a}_p$. We will refer to the eigenvalue method that results from optimizing $\mathcal{J}_1$ as the 'first eigenvalue method'.

Second performance functional

For the second functional a similar derivation gives us to the following expression

$$\frac{\partial \mathcal{J}_2(\boldsymbol{a})}{\partial a_q^*} = \frac{1}{\boldsymbol{a}^\mathrm{H}\Xi^{\mathcal{D}_\mathrm{h}}\boldsymbol{a}}\left[\sum_{p=1}^{S}\xi_{p,q}^{\mathcal{D}_\mathrm{t}}a_p - \mathcal{J}_2(\boldsymbol{a})\sum_{p=1}^{S}\xi_{p,q}^{\mathcal{D}_\mathrm{h}}a_p\right] = 0 \tag{5.17}$$

leading to

$$\Xi^{\mathcal{D}_\mathrm{t}}\boldsymbol{a} = \mathcal{J}_2(\boldsymbol{a})\Xi^{\mathcal{D}_\mathrm{h}}\boldsymbol{a} \tag{5.18}$$

which we recognize as a *generalized* eigenvalue problem with eigenvalues $\mathcal{J}_2(\boldsymbol{a}_p)$, system matrices $\Xi^{\mathcal{D}_\mathrm{t}}$ and $\Xi^{\mathcal{D}_\mathrm{h}}$ and eigenvectors $\boldsymbol{a}_p$. We will refer to the eigenvalue method that results from optimizing $\mathcal{J}_2$ as the 'second eigenvalue method'.

Discussion

All eigenvectors are normalized such that $\|\boldsymbol{a}_p\| = 1$ for all p. By doing so, we can compare different power dissipation patterns since the input power is always the same.

Also, we order the eigenvectors such that $\mathcal{J}_{1,2}(\boldsymbol{a}_p) > \mathcal{J}_{1,2}(\boldsymbol{a}_{p+1})$. For the first eigenvalue method, the first eigenvector $\boldsymbol{a}_1$ will then yield maximal average power dissipation in the tumor. Analogously, minimal power dissipation in the tumor is attained through the last eigenvector $\boldsymbol{a}_S$ since $\mathcal{J}_1(\boldsymbol{a}_S)$ denotes the smallest eigenvalue. Since we normalize the eigenvectors, the biggest eigenvalue represents the average power dissipated in the tumor domain. As noted in [4], the quotient of the biggest and smallest eigenvalue can indicate the ability of the system to heat or preserve a domain. However, since we are not interested in preserving the tumor domain, this measure can not indicate the system performance.

For the second eigenvalue method, the first eigenvector will maximize the ratio between the average power dissipation in the tumor and the average power dissipation in the healthy tissue. In the second eigenvalue method the biggest eigenvalue directly represents the ratio between the average power dissipation in the tumor and the average power dissipation in the healthy domain. This functional can serve as an indication for the system performance since it resembles the main goal of thermal ablation (Eq. (5.3)).

To conclude the description of the eigenvalue methods we note that, since the resulting eigenvalue problems concern hermitian and positive definite matrices, we can use efficient eigenvalue solvers that are available in software libraries.

5.4 Conjugate gradient method

We can also apply the conjugate gradient method to the power optimization problem, which would yield an iterative method as opposed to the closed form solution of the eigenvalue method. The conjugate gradient method has been used in hyperthermia treatment techniques in the past, where it was used to optimize the temperature distribution directly [12, 32]. In the present case, the conjugate gradient method aims at updating the feed vector in such a way that the power distribution is improved. We will apply the same steps as described in Chapter 4, hence, we will present the method more briefly here. For more details on the conjugate gradient method, we refer the reader to Chapter 4.

5.4.1 Operator notation

We start by defining the basic elements of the conjugate gradient method. Among these are the source operator **S**, the inner product on the source domain and the adjoint source operator $\mathbf{S}^\star$.

Source operator S

We need to describe the relation between the field and the feed vector through an operator. We have already seen this relation in the eigenvalue method, and we will now write this as

$$\mathbf{S}\boldsymbol{a} = \sum_{s=1}^{S} a_s \boldsymbol{E}_s \tag{5.19}$$

where **S** denotes the source operator which maps $\mathbb{C}^S$ onto $\mathbb{C}^{\kappa\times M\times N}$.

Inner product on the source domain

In order to find an expression for the adjoint source operator, we need to adopt an inner product which acts on the feed vector in the source domain $\mathcal{S}$. It is given for complex feed functions u and v by

$$\langle \boldsymbol{u}\,, \boldsymbol{v}\rangle_{\mathcal{S}} = \int\limits_{\boldsymbol{x}\in\mathcal{S}} \langle \boldsymbol{u}(\boldsymbol{x})\,, \boldsymbol{v}(\boldsymbol{x})\rangle \mathrm{d}V = \int\limits_{\boldsymbol{x}\in\mathcal{S}} u(\boldsymbol{x})\overline{v(\boldsymbol{x})}\mathrm{d}V \tag{5.20}$$

when u and v are continuous functions and

$$\langle \boldsymbol{u}\,, \boldsymbol{v}\rangle_{\mathcal{S}} = \sum_{s=1}^{S} u_s \overline{v_s} \tag{5.21}$$

for the feed vector driving the line sources in our configuration. For both the squared norm is written as

$$\|\boldsymbol{u}\|_{\mathcal{S}}^2 = \langle \boldsymbol{u}\,, \boldsymbol{u}\rangle_{\mathcal{S}}\,. \tag{5.22}$$

Adjoint source operator $\mathbf{S}^\star$

Intuitively we see that the adjoint source operator will map $\mathbb{C}^{\kappa\times M\times N}$ onto $\mathbb{C}^S$. It is defined through the relation

$$\langle \boldsymbol{r}\,, \mathbf{S}\boldsymbol{a}\rangle_{\mathcal{D}} = \langle \mathbf{S}^\star \boldsymbol{r}\,, \boldsymbol{a}\rangle_{\mathcal{S}}\,. \tag{5.23}$$

By substituting the expressions for the inner products and the source operator and interchanging the summations we find the adjoint source operator simply as

$$(\mathbf{S}^\star \boldsymbol{r})_s = \Delta x_1 \Delta x_2 \sum_{\kappa=1}^{2}\sum_{m=1}^{M}\sum_{n=1}^{N} \overline{E_{\kappa;m,n,s}}\, r_{\kappa;m,n}\,. \tag{5.24}$$

5.4.2 Cost functional

The conjugate gradient method is introduced to improve a given power distribution. This improvement is measured by the cost functional $\mathcal{J}_3$ that will be *minimized* here.

The basic idea behind the current approach is introduced in [2]. The power optimization problem at hand consists of two *conflicting objectives*. The first objective is to maximize the average power dissipated in the tumor, and the second objective is to minimize the average power dissipated in the healthy tissue. For the thermal ablation of the tumor it might be more important to sacrifice some power dissipated in the tumor in order to reduce the power dissipated in the healthy tissue.

The starting point of the algorithm is a feed vector $\boldsymbol{a}_0$ that maximizes the average power dissipated in the tumor. Then, we minimize a cost functional that consists of two terms, namely the average power dissipated in the healthy tissue and the deviation from $\boldsymbol{a}_0$. The latter term represents the maximization of the average power dissipated in the tumor since this is the starting point of the algorithm. The terms are combined via a real valued weighting parameter ν.

The cost functional is written as

$$\begin{aligned}\mathcal{J}_3(\boldsymbol{a}) &= \frac{\langle \sigma\mathbf{S}\boldsymbol{a}\,, \mathbf{S}\boldsymbol{a}\rangle_{\mathcal{D}_\mathrm{h}}}{\langle \sigma\mathbf{S}\boldsymbol{a}_0\,, \mathbf{S}\boldsymbol{a}_0\rangle_{\mathcal{D}_\mathrm{h}}} + \nu\frac{\|\boldsymbol{a}-\boldsymbol{a}_0\|_{\mathcal{S}}^2}{\|\boldsymbol{a}_0\|_{\mathcal{S}}^2} \\ &= \eta_{\mathcal{D}_\mathrm{h}}\|w_\mathrm{h}\mathbf{S}\boldsymbol{a}\|_{\mathcal{D}}^2 + \eta_{\mathcal{S}}\|\boldsymbol{a}-\boldsymbol{a}_0\|_{\mathcal{S}}^2\end{aligned} \tag{5.25}$$

where we have

$$\mathcal{J}_3(\boldsymbol{a}_0) = 1\,. \tag{5.26}$$

The weighting function w_h is defined as

$$w_\mathrm{h}(\boldsymbol{x}) = \begin{cases} \sqrt{\sigma(\boldsymbol{x})} & \forall\ \ \boldsymbol{x}\in\mathcal{D}_\mathrm{h} \\ 0 & \forall\ \ \boldsymbol{x}\notin\mathcal{D}_\mathrm{h}\end{cases} \tag{5.27}$$

and the normalization constants are written as

$$\eta_{\mathcal{D}_\mathrm{h}} = \left(\|w_\mathrm{h}\mathbf{S}\boldsymbol{a}_0\|_{\mathcal{D}}^2\right)^{-1} \tag{5.28}$$

$$\eta_{\mathcal{S}} = \nu \left(\|\boldsymbol{a}_0\|_{\mathcal{S}}^2\right)^{-1} . \tag{5.29}$$

Since we are interested in the focusing of the power, i.e. the relative distribution of power instead of the absolute power dissipation, we will apply a unit norm constraint on the feed vector. This unit norm restricts the solution space to a unit ball in $\mathbb{C}^S$.

5.4.3 Updating the feed vector

Now that we have defined the basic elements of the conjugate gradient method, we can describe the sequence of updates that minimize the cost functional $\mathcal{J}_3$.

Starting vector for $n = 0$

As indicated before, the algorithm starts with the feed vector which maximizes the power dissipation in the tumor, denoted by $\boldsymbol{a}_0$. This feed vector can be obtained from the eigenvalue method applied to $\mathcal{J}_1$ or $\mathcal{J}_2$.

Update sequence

The update sequence consists of two steps. The first is the standard conjugate gradient step and the second implements the unit norm constraint. We write the updates as

$$\tilde{\boldsymbol{a}}_n = \boldsymbol{a}_{n-1} + \beta_n \boldsymbol{\theta}_n \tag{5.30}$$

where $\boldsymbol{\theta}_n$ denotes the update direction, weighted by β_n. The second step is written as

$$\boldsymbol{a}_n = \frac{\tilde{\boldsymbol{a}}_n}{\|\tilde{\boldsymbol{a}}_n\|_{\mathcal{S}}} . \tag{5.31}$$

We note that due to the unit norm constraint, the orthogonality between the gradients is lost.

Convergence

In the current optimization problem we say that the algorithm has converged when the algorithm has reached a minimum of the cost functional. We will consider a relative decrease of less than $1 \cdot 10^{-5}$ to be sufficient for quitting the iterative process.

5.4.4 Update direction

For constructing the update direction $\boldsymbol{\theta}_n$ we start again by taking the negative gradient of the cost functional $\mathcal{J}_3$ with respect to the changes in the feed vector $\boldsymbol{a}$ evaluated in $\boldsymbol{a}_{n-1}$. Using the Fréchet derivative relation and the parameterization $\boldsymbol{a} = \boldsymbol{a}_{n-1} + \tau\boldsymbol{\theta}_n$, we find the following relation for the gradient

$$\begin{aligned}
\mathrm{Re}\langle\partial\boldsymbol{\theta}_n\,,\boldsymbol{\theta}_n\rangle_{\mathcal{S}} &= \lim_{\tau\to0}\frac{\mathcal{J}_3(\boldsymbol{a}_{n-1}+\tau\boldsymbol{\theta}_n)-\mathcal{J}_3(\boldsymbol{a}_{n-1})}{\tau} \\
&= \lim_{\tau\to0}\frac{\eta_{\mathcal{D}_\mathrm{h}}\|w_\mathrm{h}\mathbf{S}(\boldsymbol{a}_{n-1}+\tau\boldsymbol{\theta}_n)\|_{\mathcal{D}}^2-\eta_{\mathcal{D}_\mathrm{h}}\|w_\mathrm{h}\mathbf{S}\boldsymbol{a}_{n-1}\|_{\mathcal{D}}^2}{\tau} \\
&\quad+\frac{\eta_{\mathcal{S}}\|\boldsymbol{a}_{n-1}+\tau\boldsymbol{\theta}_n-\boldsymbol{a}_0\|_{\mathcal{S}}^2-\eta_{\mathcal{S}}\|\boldsymbol{a}_{n-1}-\boldsymbol{a}_0\|_{\mathcal{S}}^2}{\tau} \\
&= \lim_{\tau\to0}2\frac{\eta_{\mathcal{D}_\mathrm{h}}\tau\mathrm{Re}\langle w_\mathrm{h}\mathbf{S}\boldsymbol{a}_{n-1}\,,w_\mathrm{h}\mathbf{S}\boldsymbol{\theta}_n\rangle_{\mathcal{D}}+\eta_{\mathcal{D}_\mathrm{h}}\tau^2\|w_\mathrm{h}\mathbf{S}\boldsymbol{\theta}_n\|_{\mathcal{D}}^2}{\tau} \\
&\quad+2\frac{\eta_{\mathcal{S}}\tau\mathrm{Re}\langle\boldsymbol{a}_{n-1}-\boldsymbol{a}_0\,,\boldsymbol{\theta}_n\rangle_{\mathcal{S}}+\eta_{\mathcal{S}}\tau^2\|\boldsymbol{\theta}_n\|_{\mathcal{S}}^2}{\tau} \\
&= 2\eta_{\mathcal{D}_\mathrm{h}}\mathrm{Re}\langle w_\mathrm{h}\mathbf{S}\boldsymbol{a}_{n-1}\,,w_\mathrm{h}\mathbf{S}\boldsymbol{\theta}_n\rangle_{\mathcal{D}}+2\eta_{\mathcal{S}}\mathrm{Re}\langle\boldsymbol{a}_{n-1}-\boldsymbol{a}_0\,,\boldsymbol{\theta}_n\rangle_{\mathcal{S}} \\
&= 2\mathrm{Re}\langle\eta_{\mathcal{D}_\mathrm{h}}\mathbf{S}^\star w_\mathrm{h}^2\mathbf{S}\boldsymbol{a}_{n-1}+\eta_{\mathcal{S}}(\boldsymbol{a}_{n-1}-\boldsymbol{a}_0)\,,\boldsymbol{\theta}_n\rangle_{\mathcal{S}} \qquad (5.32)
\end{aligned}$$

from which we recognize the gradient as

$$\partial\boldsymbol{\theta}_n = \eta_{\mathcal{D}_\mathrm{h}}\mathbf{S}^\star w_\mathrm{h}^2\mathbf{S}\boldsymbol{a}_{n-1}+\eta_{\mathcal{S}}(\boldsymbol{a}_{n-1}-\boldsymbol{a}_0)\,. \tag{5.33}$$

We then write the conjugate gradient update direction as

$$\boldsymbol{\theta}_n = \begin{cases} -\partial\boldsymbol{\theta}_n & \forall \;\; n=1 \\ -\partial\boldsymbol{\theta}_n+\gamma_n\boldsymbol{\theta}_{n-1} & \forall \;\; n>1 \end{cases} \tag{5.34}$$

where we use the Polak-Ribière formula for the coefficients γ_n, given by

$$\gamma_n = \frac{\langle\partial\boldsymbol{\theta}_n\,,\partial\boldsymbol{\theta}_n-\partial\boldsymbol{\theta}_{n-1}\rangle_{\mathcal{S}}}{\|\partial\boldsymbol{\theta}_{n-1}\|_{\mathcal{S}}^2}\,. \tag{5.35}$$

5.4.5 Weighting parameter

We find the optimal weighting parameter by differentiating the cost functional in the n^{th} iteration for a variation in β_n, and equating this result to zero, viz.

$$\frac{\partial}{\partial\beta_n}\mathcal{J}_3(\boldsymbol{a}_{n-1}+\beta_n\boldsymbol{\theta}_n) = 0\,. \tag{5.36}$$

We obtain the following expression for the left-hand side using standard differentiation rules

$$2\eta_{\mathcal{D}_\mathrm{h}}\langle w_\mathrm{h}\mathbf{S}(\boldsymbol{a}_{n-1}+\beta_n\boldsymbol{\theta}_n)\,,w_\mathrm{h}\mathbf{S}\boldsymbol{\theta}_n\rangle_{\mathcal{D}}+2\eta_{\mathcal{S}}\langle\boldsymbol{a}_{n-1}+\beta_n\boldsymbol{\theta}_n-\boldsymbol{a}_0\,,\boldsymbol{\theta}_n\rangle_{\mathcal{S}} = 0 \tag{5.37}$$

which yields

$$\begin{aligned}\beta_n &= -\frac{\eta_{\mathcal{D}_\mathrm{h}}\langle w_\mathrm{h}\mathbf{S}\boldsymbol{a}_{n-1}\,,w_\mathrm{h}\mathbf{S}\boldsymbol{\theta}_n\rangle_{\mathcal{D}} + \eta_{\mathcal{S}}\langle \boldsymbol{a}_{n-1}-\boldsymbol{a}_0\,,\boldsymbol{\theta}_n\rangle_{\mathcal{S}}}{\eta_{\mathcal{D}_\mathrm{h}}\|w_\mathrm{h}\mathbf{S}\boldsymbol{\theta}_n\|^2_{\mathcal{D}} + \eta_{\mathcal{S}}\|\boldsymbol{\theta}_n\|^2_{\mathcal{S}}} \\ &= -\frac{\eta_{\mathcal{D}_\mathrm{h}}\langle \mathbf{S}^\star w_\mathrm{h}^2\mathbf{S}\boldsymbol{a}_{n-1}\,,\boldsymbol{\theta}_n\rangle_{\mathcal{S}} + \eta_{\mathcal{S}}\langle \boldsymbol{a}_{n-1}-\boldsymbol{a}_0\,,\boldsymbol{\theta}_n\rangle_{\mathcal{S}}}{\eta_{\mathcal{D}_\mathrm{h}}\|w_\mathrm{h}\mathbf{S}\boldsymbol{\theta}_n\|^2_{\mathcal{D}} + \eta_{\mathcal{S}}\|\boldsymbol{\theta}_n\|^2_{\mathcal{S}}} \\ &= -\frac{\langle \partial\boldsymbol{\theta}_n\,,\boldsymbol{\theta}_n\rangle_{\mathcal{S}}}{\eta_{\mathcal{D}_\mathrm{h}}\|w_\mathrm{h}\mathbf{S}\boldsymbol{\theta}_n\|^2_{\mathcal{D}} + \eta_{\mathcal{S}}\|\boldsymbol{\theta}_n\|^2_{\mathcal{S}}}\,. \end{aligned} \tag{5.38}$$

This subsection is concluded by noting that we have now described all elements which constitute the conjugate gradient method for optimizing the power dissipation in the breast. The three power optimization methods that are presented in this chapter will be evaluated in the next chapter.

Chapter 6

Numerical simulations and results

In order to validate the methods presented in previous chapters and determine the feasibility of focused microwave ablation of female breast tumors, a series of numerical experiments have been performed. Through these experiments we also optimized some unspecified system parameters, this will be done through a number of experiments with parameter sweeps.

All methods that we evaluate have been implemented in Fortran 90. The Laboratory of Electromagnetic Research of the Delft University of Technology supplied us the Fortran routines for the forward solver.

We have implemented the first eigenvalue method in the `Focus_Pt_to_Pin` routine, which uses the `DEVEHF` routine of the IMSL library to solve the eigenvalue problem. The conjugate gradient method has been implemented numerically without any external routines in the routine called `FOCUS_CG`.

The routine that focuses the fields according to the second eigenvalue method is called `Focus_Pt_to_Ph`. We followed the same structure as the Matlab function `eig`. This comes down to transforming the generalized eigenvalue problem into a standard eigenvalue problem by applying a cholesky factorization for $\Xi^{\mathcal{D}_\mathrm{h}}$ and solving this equivalent problem with the `DEVCCG` routine of the IMSL library. For the transformation we have used the IMSL routines `DLFTDH` and `DLINCT`. The quality of the solutions has been checked through the IMSL routines `DEPIHF` for the first eigenvalue method and `DEPICG` for the second eigenvalue method.

The processing of the results and the generation of numerical breast models has been done in Matlab. All computations have been done on an desktop PC with an Intel Core Duo E8400 processor running at 3 GHz and 3 GB of memory.

6.1 Problem indication

Before we present the results of the optimization studies, we will indicate the need for accurate computation of the wave fields and power optimization methods through an example of the Target Center Position (TCP) method [3]. This algorithm focuses power at a point by compensating for the phase differences between the *incident* fields at the desired point. This power optimization method does not take the scattering of the object into account, neither does it account for the shape or the size of the tumor.

We have set up a center focused incident field, by applying the following feed vector

$$a_s = \mathrm{e}^{\mathrm{j}\frac{2\pi s}{S}}\,, \quad \text{for } s = 1, \ldots, S\,. \tag{6.1}$$

This excitation yields the total incident field as shown in Fig. 6.1a. We introduced some losses (e.g. $1 \cdot 10^{-9}$ S/m) for processing ease. In this simulation we have used $f = 5$ GHz, $S = 32$ and $\varepsilon_{\mathrm{r,b}} = 10$. When introducing the breast model in the configuration, the resulting power dissipation pattern is shown in Fig. 6.1b. The colorscale has been clipped to the maximum inside the breast.

It is clear that the scattering of the breast alters the interference pattern. Not only has the focal spot been lost, all healthy tissue is heated with significant hot spots occurring in the high conducting parts of the breast, rendering this method not suitable for the thermal ablation of breast cancer. This result indicates that the field is strongly scattered by the breast. Thus, an accurate propagation model is important, together with an optimization methods for focusing the scattered fields in the best way possible.

The dielectric properties of the breast model that is used in these latter simulation, and throughout the rest of this chapter are shown in Fig. 6.2. We repeat it here, since it provides an indication for the local heating potential of certain tissue areas. This can aid the reader in evaluating the pictures that are presented in this chapter.

6.2 The forward scattering problem

In this section we will investigate the performance of the conjugate gradient method for solving the forward scattering problem. We will also investigate the influence of the gridsize, bolus permittivity $\varepsilon_{\mathrm{r,b}}$, operational frequency f and number of sources S on the performance of this algorithm and on the focusing ability of the system. The goal of these parameter sweeps is to explore which system parameters are optimal in ablative therapy. The focusing ability of the system is evaluated using the eigenvalue method for $\mathcal{J}_2$, configured to focus the power in the tumor A shown in Fig. 3.4b.

We note that we will not consider the influence of the array radius here. Simulations with different array radii showed that a smaller radius increases the power density in the breast since the configuration is closer to the sources. However, it did not influence the relative distribution of power, i.e. the focusing ability of the system.

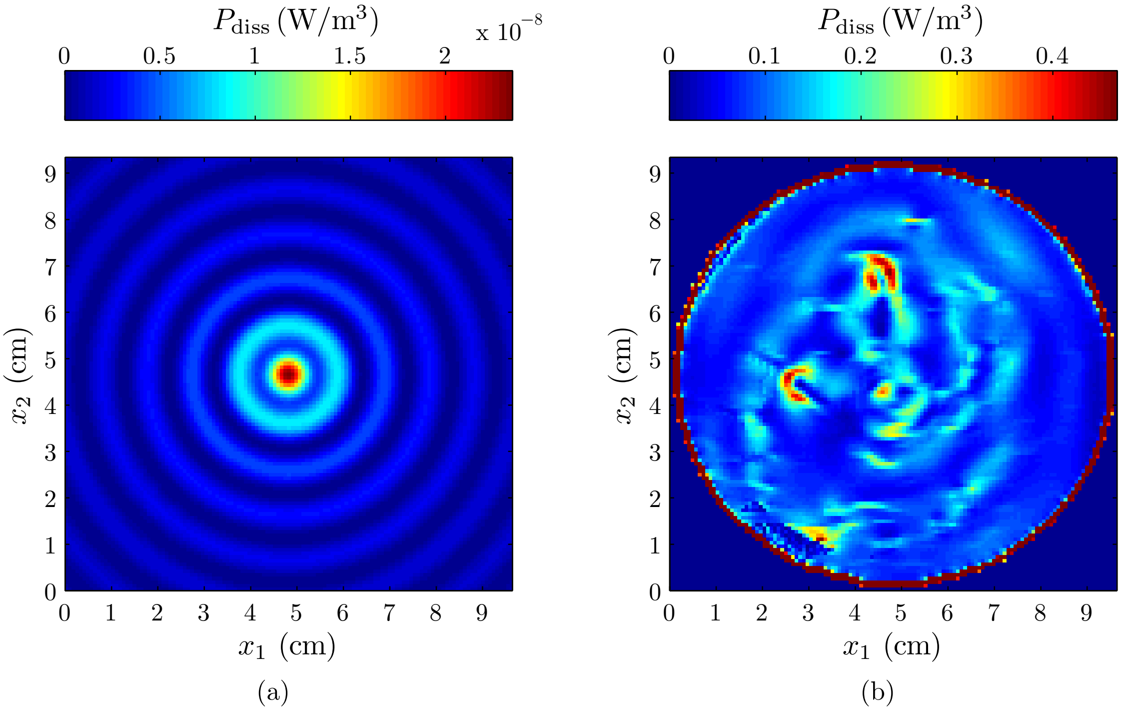

(a) (b)

Fig. 6.1: Center focused field (a) and the power distribution that results from introducing the breast (b)

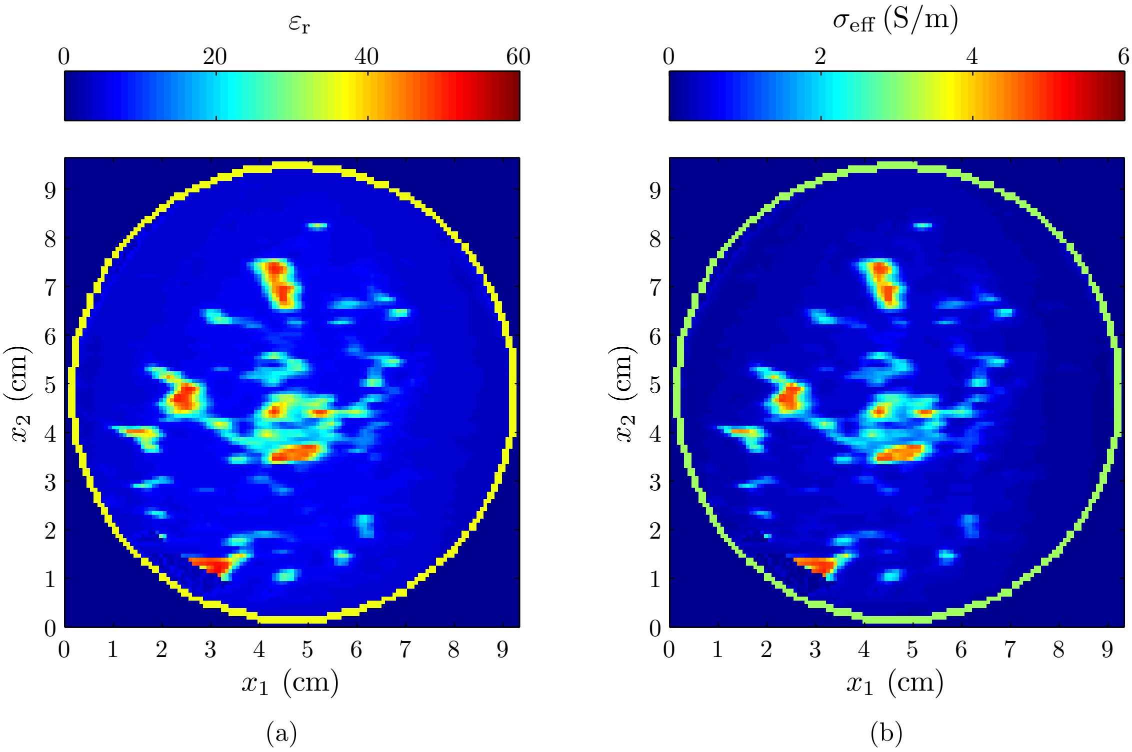

(a) (b)

Fig. 6.2: Dielectric permittivity (a) and effective conductivity (b) of a transverse section of the numerical breast model for f = 5 GHz

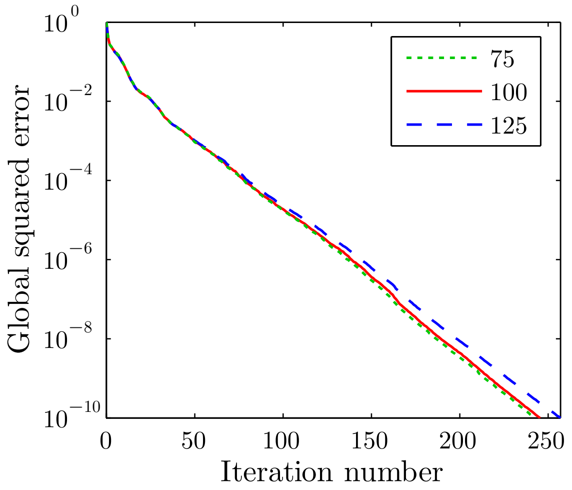

Fig. 6.3: Convergence for the three different grids

6.2.1 Gridsize

The first parameter that we investigate is the gridsize. In general, taking more samples of a function will improve its approximation. This will however raise the computational costs since there are more values that need to be computed. In order to investigate the numerical dependence on the gridsize, we test the conjugate gradient method for solving the forward scattering problem with three differently discretized numerical breast models. In this part of the investigation we will set $f = 5$ GHz, $S = 32$ and $\varepsilon_{\mathrm{r,b}} = 10$.

The numerical breast models that are available in the online repository have a discretization step size of 0.5 mm [43]. We downsample the chosen breast model such that its length and width are below 75 subdomains, secondly below 100 subdomains and finally below 125 subdomains. Also, we remove a strip of the background border such that the resulting discretized domain has a single strip of zero contrast around the domain as required by Eqs. (4.13) and (4.14). The resulting computational domains consist of 75-by-73, 100-by-97 and 125-by-121 subdomains, respectively. For downsampling we used the two-dimensional interpolation function `interp2` of Matlab to apply a 'nearest neighbour' interpolation method. Other methods have been considered as well but this method preserved the 'layer' structure of the skin best. The resulting discretized models have a step size of approximately 1.3 mm, 0.97 mm and 0.77 mm, respectively.

Due to the interpolation step the resulting models actually represent slightly different breasts. Hence, comparing field related values is not a suitable way of evaluating the numerical dependence of the conjugate gradient method. We can however compare the convergence rates and computation time. In Fig. 6.3 the convergence of the conjugate gradient method for the three different gridsizes is compared.

It is interesting to see that the convergence rates of the three different gridsizes are practically the same. This is because the level of heterogeneity with respect to the wavelength has not increased, but is just represented through more gridpoints. The differences that do appear are likely due to interpolation differences.

Another interesting outcome is that with these three different gridsizes the algorithm took almost the same amount of time to reach convergence. The time needed for computing the fields was 23, 24 and 25 minutes for the 75-by-73, 100-by-97 and 125-by-121 configuration, respectively. The time needed for computation is approximately the same in these cases due to zero-padding for the FFT algorithm. This causes the arrays to be extended to the same width and length of 2^n, where n is 8 in our case. It then simply follows that taking the biggest grid that fits a certain FFT size yields the most accurate results without any extra computational costs. In other words, the dependence of the computation time on the gridsize is quantized due to the use of FFT's.

We note that when using this grid at a frequency of 10 GHz, the resolution requirement of approximately 6 points per wavelength is satisfied for relative permittivity values up to 42, which is in fact higher than the median relative permittivity of glandular and fibroconnective tissues. Hence, inaccuracies will be present but we consider this discretization step size to be sufficiently accurate for constructing an approximation of the fields inside the breast.

6.2.2 Bolus permittivity

In this part we investigate the desired permittivity value of the bolus and its influence on the conjugate gradient method for solving the forward scattering problem. One of the functions of the bolus material is to improve the power transmission into the breast. Power which is reflected is not transmitted into the breast, hence the reflections originating at the skin interface reduce the power dissipated in the tumor. Another mechanism that deteriorates the focusing ability of the system is the diffuse scattering of the electromagnetic fields. Thus, the bolus material should reduce both the reflections at the skin interface, as well as the overall scattering of the wave fields inside the breast.

In order to reduce reflections we could think of matching the bolus permittivity to that of the skin. This would reduce the initial reflection and hence this benefits the transmission of power into the breast. However, the scattering inside the breast would then increase. By matching to the adipose tissue we would reduce the overall contrast, hence, the overall scattering is reduced consequently. However, power transmission into the breast is reduced in this case. In other words, we have encountered a trade-off scenario. In order to investigate the optimal permittivity value we have run the eigenvalue method for $\mathcal{J}_2$ on tumor A with 32 sources operating at a frequency of $f = 5$ GHz and we test bolus permittivities ranging from 5 to 35.

In Fig. 6.4 we illustrate the number of iterations needed for convergence together with the value of $\mathcal{J}_2(\boldsymbol{a}_1)$ for different values of $\varepsilon_{\mathrm{r,b}}$. We observe that the number of iterations is minimal for $\varepsilon_{\mathrm{r,b}} \approx 10$. This is because this bolus permittivity reduces the average contrast on the computational domain. With respect to the focusing ability of the system we conclude that $\varepsilon_{\mathrm{r,b}} \approx 20$ is the optimum. We note that this value might not be optimal for all frequencies or tumors, but its influence on the system performance is low enough to accept a potentially suboptimal bolus permittivity in other cases.

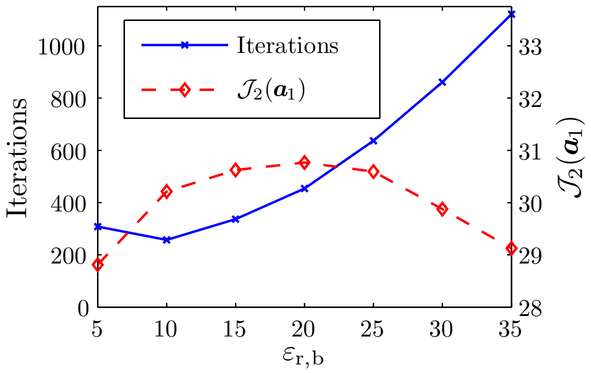

Fig. 6.4: Iterations needed and the focusing ability of the system for different values of the bolus permittivity at $f = 5$ GHz

6.2.3 Operational frequency

From antenna theory we know that the main beamwidth of an antenna, for a fixed antenna size, is proportional to the wavelength. Thus, choosing a higher operational frequency can increase the focusing ability of the system since the focal spot will become smaller. We note that the decrease in tissue permittivity does not cancel this trend. However, increasing the frequency will reduce the transmission of power into the breast. Also, we know that the conductivity of breast tissues increases with frequency, therefore the power transmission into the breast will decrease even further. Hence, we find ourselves again in a trade-off scenario and we will therefore perform a frequency sweep from 1 to 10 GHz with steps of 1 GHz in order to find the optimal operating frequency. We will apply the results obtained in the previous optimizations, that is $\varepsilon_{\mathrm{r,b}} = 20$ and the 125-by-121 grid. We again consider the ablation of tumor A and we set $S = 32$.

The variation of the number of iterations needed for convergence and the value of $\mathcal{J}_2(\boldsymbol{a}_1)$ are shown in Fig. 6.5 for frequencies between 1 and 10 GHz. We observe an increasing trend in the number of iterations needed for convergence, because this is related to the level of heterogeneity with respect to the wavelength. We see that the optimal frequency is around 4 and 5 GHz in this case.

The performance of the system seems to depend significantly on the frequency. The most optimal power distributions for $f = 1$ GHz and $f = 10$ GHz are illustrated in Fig. 6.6. Clearly, the performance of the system is unsatisfactory at these frequencies. For $f = 1$ GHz, we cannot even recognize a focal spot[1]. For $f = 10$ GHz, we see that the power transmission into the breast is very bad and most power is dissipated in between the skin and the tumor.

---

[1] With the eigenvalue method for $\mathcal{J}_1$ we did observe a focal spot, however at the cost of an increased power dissipation in the healthy tissue.

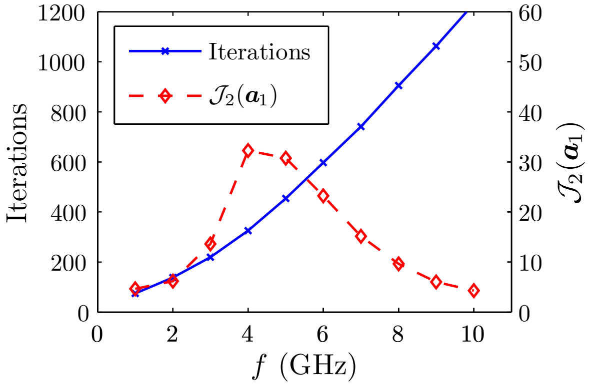

Fig. 6.5: Iterations needed and the focusing ability of the system for different operating frequencies with $\varepsilon_{\mathrm{r,b}} = 20$

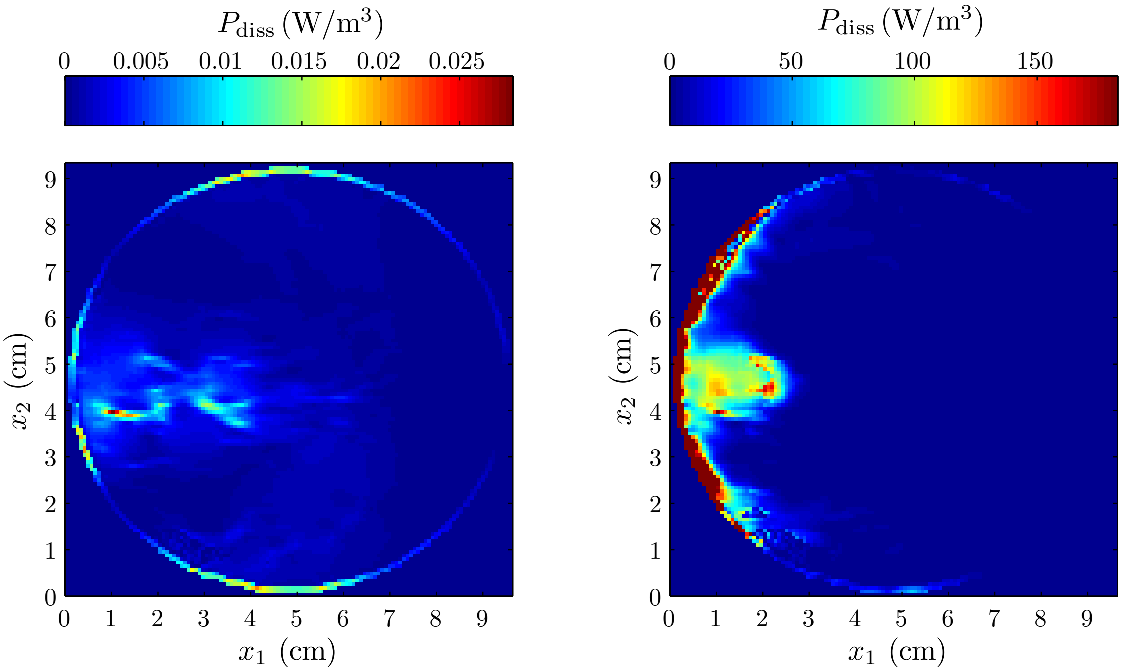

(a) (b)

Fig. 6.6: Comparison between the most optimal power dissipation patterns for $f = 1$ GHz (a) and $f = 10$ GHz (b) obtained through the eigenvalue method for $\mathcal{J}_2$

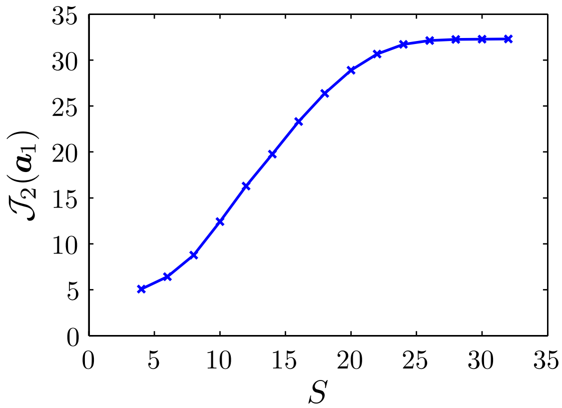

Fig. 6.7: Focusing ability of the system for different number of sources at $f = 4$ GHz

6.2.4 Number of sources

When considering the number of sources to use in our configuration, we know on beforehand that adding sources will in general improve the focusing abilities of the system. In Fig. 6.7, $\mathcal{J}_2(\boldsymbol{a}_1)$ is plotted for different values of S. The other parameters are again set to the optimal values previously found, i.e. $f = 4$ GHz, $\varepsilon_{\mathrm{r,b}} = 20$ and the 125-by-121 grid.

We see that the system performance indeed increases when we add sources but the improvement gradually stalls at $S \approx 26$. In the following investigations we choose to set the number of sources at 32 since it simply guarantees the best system performance.

In practice, the interactions between array elements will have to be taken into account. In that case, a smaller number of elements might be preferable in order to decrease the mutual coupling between elements. This consideration is however not relevant here.

We note that the performance of the conjugate gradient method for solving the forward scattering problem is not relevant since it concerns independent EFIE equations. Hence, the individual convergence rates do not depend on the number of sources. However, the computation time does increase approximately linearly with the number of sources.

6.3 Homogeneous configuration

In this section we will evaluate the power optimization methods presented in Chapter 5 for a homogeneous configuration in order to validate the methods and gain more insight in their fundamental behaviour. First we test the two eigenvalue methods and then we test the conjugate gradient method.

The computational domain in this configuration is completely filled with a relative permittivity of 20. In order to construct nonzero system matrices for the eigenvalue problem, we have introduced some losses (e.g. $1{\cdot}10^{-9}$ S/m) in the bolus material. Experiments are time efficient in this configuration since the fields are computed in just 1 iteration of the conjugate gradient scheme.

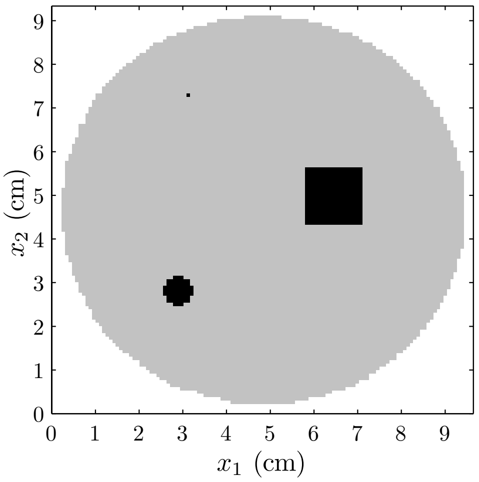

Fig. 6.8: The three focusing domains and the nulling domain in the homogeneous study

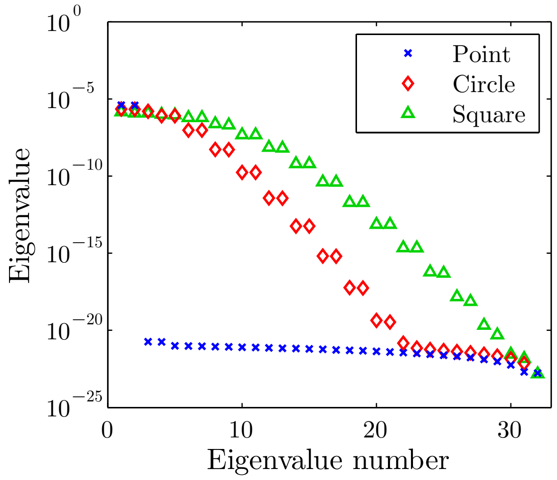

Fig. 6.9: The eigenvalues $\mathcal{J}_1$ for the three target domains

We assign three focusing domains. The first is a point, or actually one subdomain. The second is a circle with a diameter of $\lambda/2$, where λ is the wavelength in the bolus material. The last domain to which we focus power is a square with sides of length λ. These target domains are illustrated in Fig. 6.8. We also investigate the placement of nulls in the surrounding area.

6.3.1 Eigenvalue method for $\mathcal{J}_1$

The first eigenvalue method will be investigated here. We recall that, in this case, our only goal is to focus power in the tumor domain. Reducing hotspots is thus not considered as a goal in this method.

Focusing towards a single point

An initial test of the eigenvalue method for $\mathcal{J}_1$ is performed with the point as tumor domain. The resulting eigenvalues are shown in Fig. 6.9. The first two eigenvalues are approximately the same, and the other eigenvalues are very low. The first two eigenvectors steer the power in two complementary power dissipation patterns as shown in Fig. 6.10.

Focusing towards the circular domain

The second analysis is performed on the circular domain. The resulting eigenvalues are also shown in Fig. 6.9 and the power dissipation patterns for the two biggest eigenvalues are presented in Fig. 6.11a and 6.11b. We observe that many eigenvalues come in pairs with approximately the same value, for example the first two eigenvalues. We see that the corresponding eigenvectors steer the power in complementary patterns, or *modes*. Combining the power distributions resulting from these modes results in a better power distribution. This is shown in Fig. 6.11.

Focusing towards the square domain

Now we investigate the focusing performance for the square target domain. The eigenvalues are shown in Fig. 6.9. In this case we see that the distribution of eigenvalues is less steep, or in other words, there are more modes that deposit power in the square domain. Again, we obtain complementary modes which can be combined to yield the desired pattern. Combining the first three leads to the pattern shown in Fig. 6.12. In this case, we weigh the patterns such that 50% contribution comes from the first mode and 25% comes from the second and third mode. This smoothens the dissipation pattern.

6.3.2 Eigenvalue method for $\mathcal{J}_2$

The second eigenvalue method resulted from maximizing the ratio between the average power in the tumor domain and the average power in the healthy domain. The eigenvalues that result from the second eigenvalue method for the tree target domains and the healthy domain are shown in Fig. 6.13a. We observe that the eigenvalues show the same distribution as for the first eigenvalue method, apart from a scaling factor. The resulting power distributions or modes don't differ much from the first eigenvalue method and are thus not reported here. This is the case because it is simply not possible to suppress the side lobes everywhere in the domain surrounding the tumor domain.

In order to validate the operation of the eigenvalue method for $\mathcal{J}_2$, we configure the circle as the tumor domain, and the square domain as the healthy domain in which the dissipated power is to be minimized. This yields an eigenvalue distribution which is shown in Fig. 6.13b. The resulting power distribution is shown in Fig. 6.14.

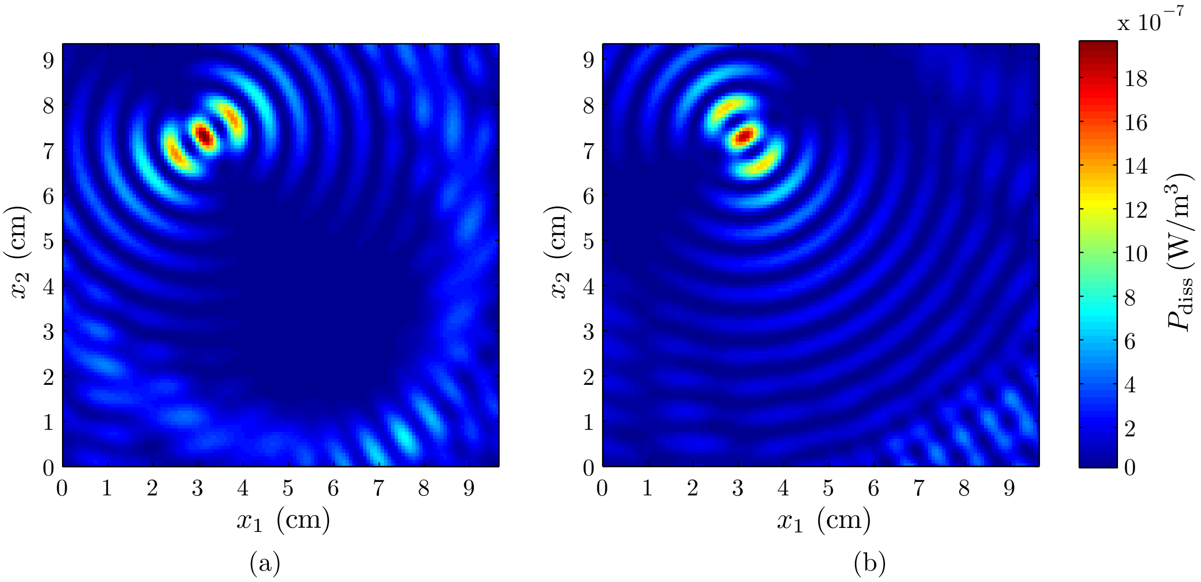

(a)

(b)

Fig. 6.10: First (a) and second (b) mode that focus power to the point target domain

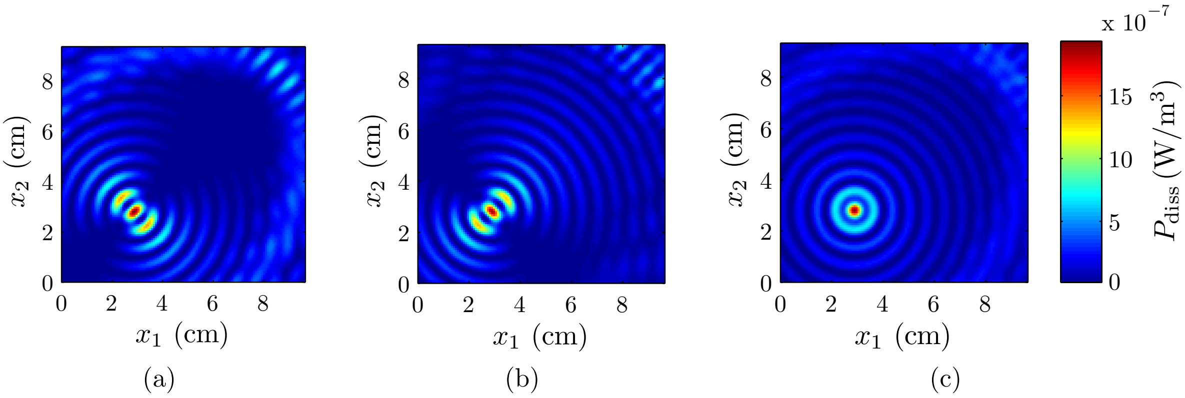

(a)

(b)

(c)

Fig. 6.11: Combining the first (a) and the second (b) mode improves the pattern (c)

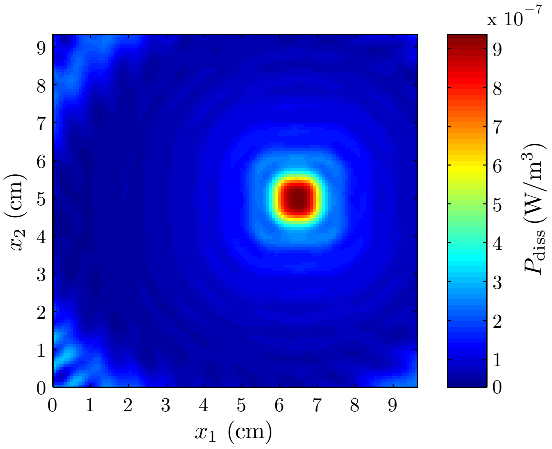

Fig. 6.12: Combining the first three modes that focus towards the square domain

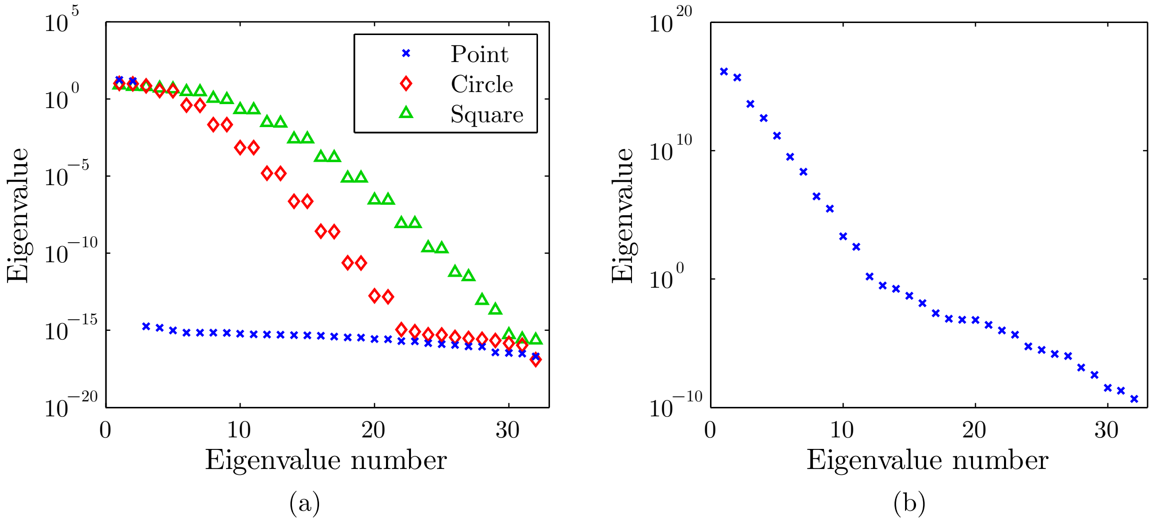

(a) (b)

Fig. 6.13: The eigenvalues $\mathcal{J}_2$ when focused on the three target domains (a) and when focused on the circle while preserving the square (b)

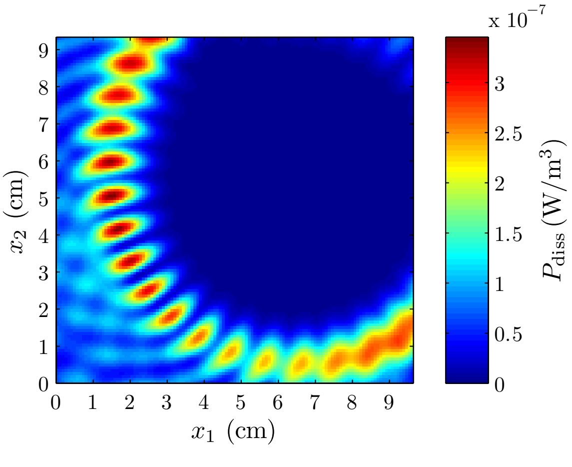

Fig. 6.14: Result of the second eigenvalue method focused on the circle while preserving the square

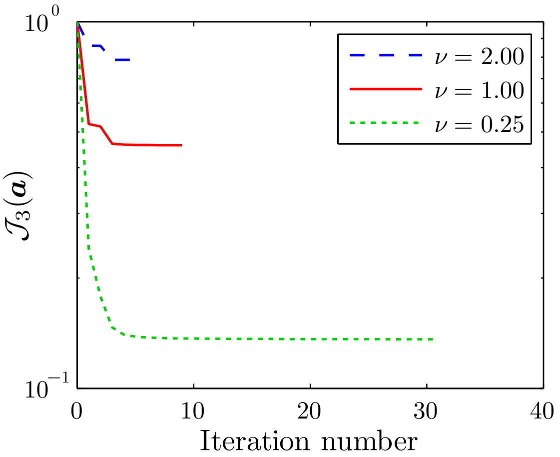

Fig. 6.15: Convergence of the conjugate gradient method for different values of the weighting parameter ν

6.3.3 Conjugate gradient method

We validate the conjugate gradient method by selecting the circle as the target domain, and the square as the healthy domain. The starting vector is taken from the first eigenvalue method which focuses power in the circular domain. We actually take the second eigenvector since this one creates side lobes covering the square domain. Thus, the algorithm will need to suppress these side lobes with the least amount of deviation of the initial pattern.

The resulting convergence plot is shown in Fig. 6.15. We see that a smaller value of the weighting parameter ν lowers the minimum of the cost functional and reduces the side lobes that cover the square domain. According to our expectations, a smaller value of ν allows a bigger deviation from the initial dissipated power pattern.

The resulting power dissipation patterns for three values of ν are shown in Fig. 6.16. Here, the power is plot in dB such that the differences are more clearly shown. We see that the dissipated power in the square domain decreases with smaller values of ν. These results show that the basic operation of this conjugate gradient scheme is correct.

So far, we have seen that the power optimization methods function correctly. Now we can introduce realistic breast model in the configuration in order to simulate a realistic treatment scenario.

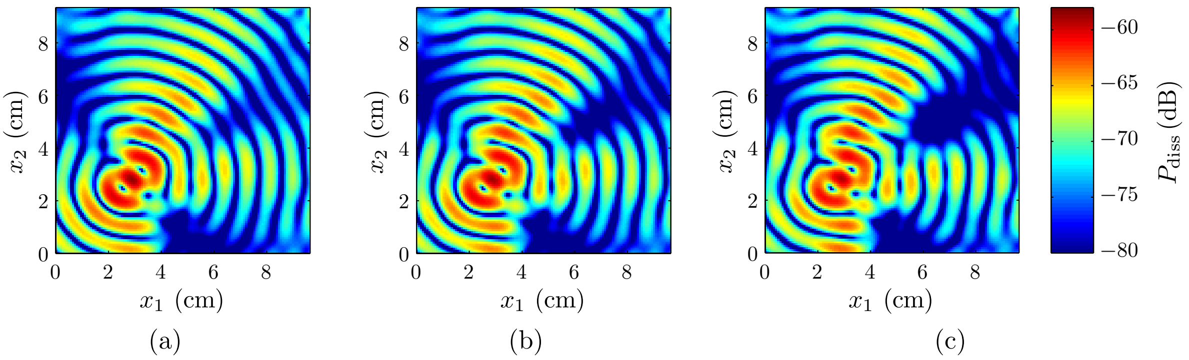

(a) (b) (c)

Fig. 6.16: Power dissipation patterns (in dB) of the conjugate gradient method for $\nu = 2.00$ (a), $\nu = 1.00$ (b) and $\nu = 0.25$ (c)

6.4 Realistic breast model

Now we will investigate the performance of the three power optimization methods on a realistic breast model. We will evaluate the power distributions when focusing towards the three tumors shown in Fig. 3.4b. We will compare the performance of the focusing algorithms per tumor. In these simulations we will apply the optimal system parameters obtained in the first section of this chapter.

For further evaluating the power distribution in the breast, we will use a normalized cumulative power histogram. It indicates what part of the healthy tissue and what part of the tumor receives a relative amount of power or more. We normalize power densities to the maximal power density found in the tumor domain, and areas or volumes are normalized to the size of the corresponding domain.

An example is shown in Fig. 6.17a. The red curve in this graph shows that in 95% of the tumor more than 30% of the maximum power density is dissipated. The blue curve on the other hand indicates that this is also the case in 5% of the healthy tissue.

6.4.1 Tumor A

First we consider the ablation of tumor A. The eigenvalues resulting from the two eigenvalue methods are shown in Fig. 6.17b. In both methods the biggest eigenvalue distinguishes itself more from the other eigenvalues, as opposed to the results of the homogeneous configuration. This is reflected in that the other mode patterns, not reported here, don't contribute much to the focusing of power into the tumor. They did produce a complementary pattern inside the tumor domain, however these modes introduced large hotspots in the healthy region as well. We will therefore evaluate the eigenvalue methods based on the first eigenvector alone.

The power distributions that are obtained with the two eigenvalue methods are illustrated in Fig. 6.19a and 6.19b. The power distributions appear to be approximately the same. Reducing the power dissipated in the healthy tissue seems to increase the power

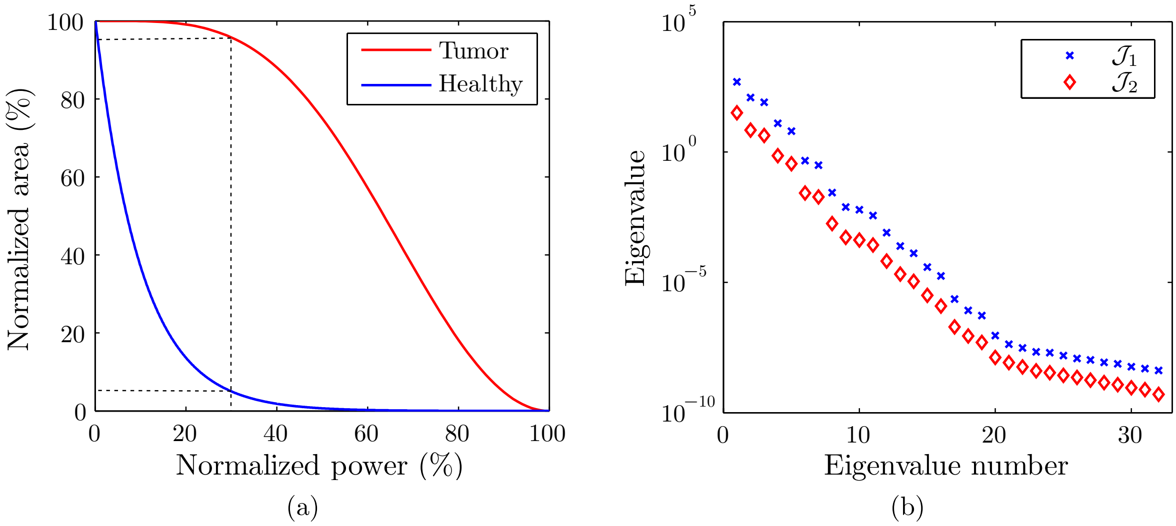

Fig. 6.17: Example of a normalized cumulative power histogram (a) and the eigenvalues resulting from the two eigenvalue methods for tumor A

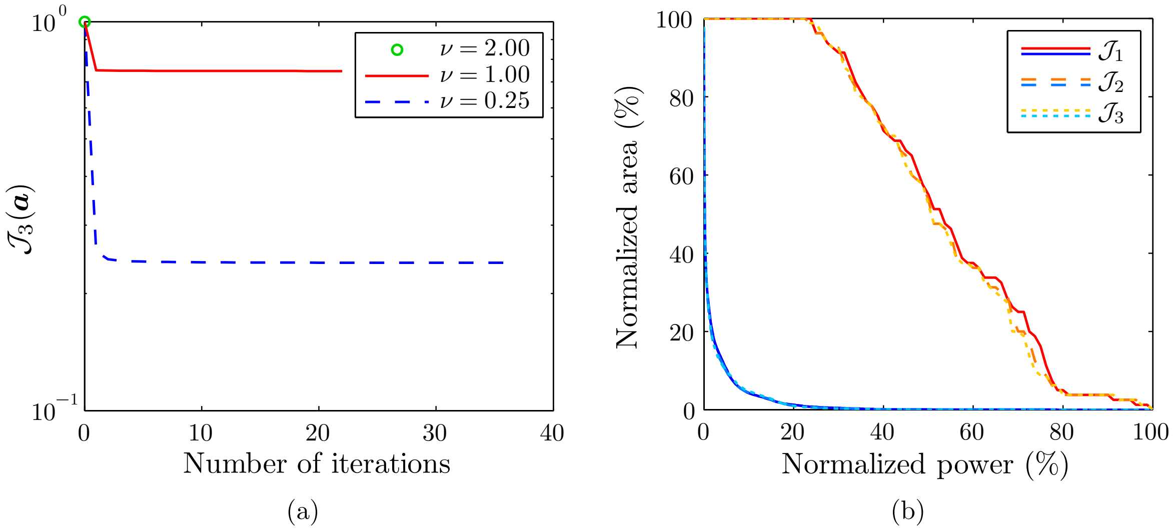

Fig. 6.18: The convergence of the conjugate gradient method for three values of ν (a) and the normalized cumulative power histograms for the two eigenvalue methods and the conjugate gradient method with $\nu = 0.25$ (b) for tumor A

dissipated in the skin, however this is not considered harmful. Although barely visible, the eigenvalue method for $\mathcal{J}_2$ reduces the peak dissipated power in the healthy tissue. In general we see that the breast is mainly illuminated by the sources that are on the left side of the breast, i.e. that are closest to the tumor. It also appears to be difficult to heat the right side of the tumor.

The conjugate gradient method was designed to decrease the power dissipated in the healthy tissue, while maintaining the focus in the tumor. We will consider improving the power dissipation pattern that was obtained through the eigenvalue method for $\mathcal{J}_2$. The convergence of the conjugate gradient method with three settings of the weighting parameter ν is plotted in Fig. 6.18a. We note that in fact, for $\nu = 2.00$ the algorithm could not improve the power distribution significantly. The lowest value for $\mathcal{J}_3$ was obtained by allowing the biggest deviation of the original pattern, thus by setting $\nu = 0.25$. The corresponding power distribution is illustrated in Fig. 6.19c.

The normalized cumulative power histograms of the two eigenvalue methods and the conjugate gradient method are shown in Fig. 6.18b. From these graphs we see that the methods yield approximately the same result. There are minor differences that indicate that the methods are in fact functioning correctly. For instance, although barely visible in the graph, the second eigenvalue method and the conjugate gradient suppress the high power dissipation in the healthy tissue which goes together with less optimal power distribution in the tumor. In general, we see that there is simply little room left for improvement of the power distribution obtained by the first eigenvalue method.

We note that we have experienced significant differences between the results of the power optimization algorithms at a suboptimal frequency, for instance at $f = 2$ GHz. For this frequency, the power distributions that result from the first two eigenvalue methods are shown in Fig. 6.20. We see clearly that the second eigenvalue suppresses the hot spot in the healthy tissue, whereas the first eigenvalue method yields a better power distribution in the tumor domain. However, both power distributions are not localized enough to be useful in focused microwave ablation of the breast tumor.

We conclude by evaluating the power distribution in terms of a thermal distribution, by using the power ratio as defined in Eq. (A.5). In a realistic treatment scenario one might choose to heat for instance 95% of the tumor to at least 50 ℃. From the cumulative power distribution we can see that this means that 94.2% of the healthy tissue is not damaged, i.e. kept below 43℃.

We note that the remaining 6% of the healthy tissue includes tissue adjacent to the tumor as well, heating of which should actually not be considered harmful since a safety margin is always taken into account in cancer treatment. Furthermore, it might be possible to reduce the input power, since the thermal conduction may still yield total coverage of the tumor site. However, this implies the need for accurate thermal simulations. In any case, we consider the results to be sufficient for regarding the ablation of tumor A possible.

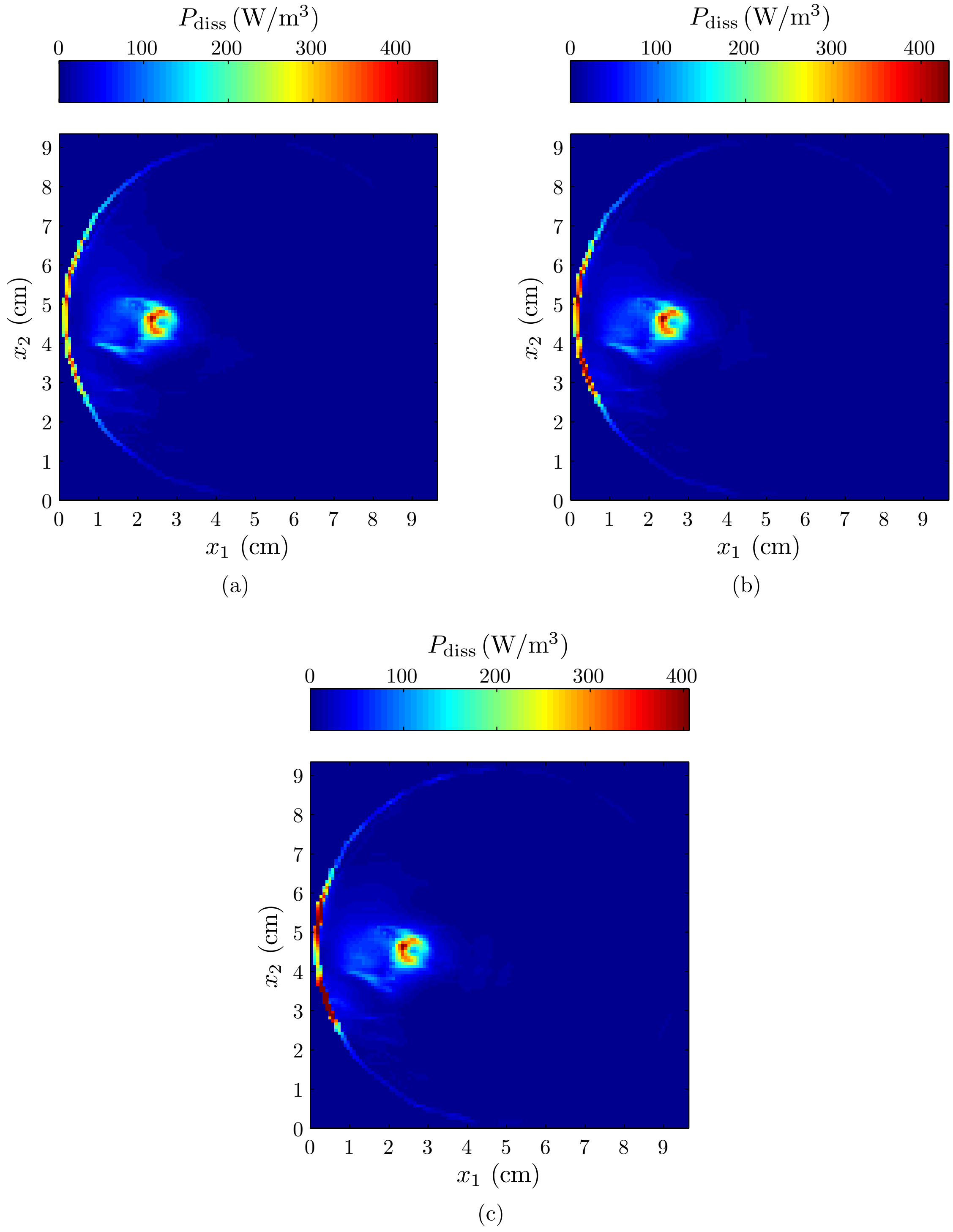

(a)

(b)

(c)

Fig. 6.19: The most optimal power distributions in the treatment of tumor A for the two eigenvalue methods (a,b) and the conjugate gradient method with $\nu = 0.25$ (c)

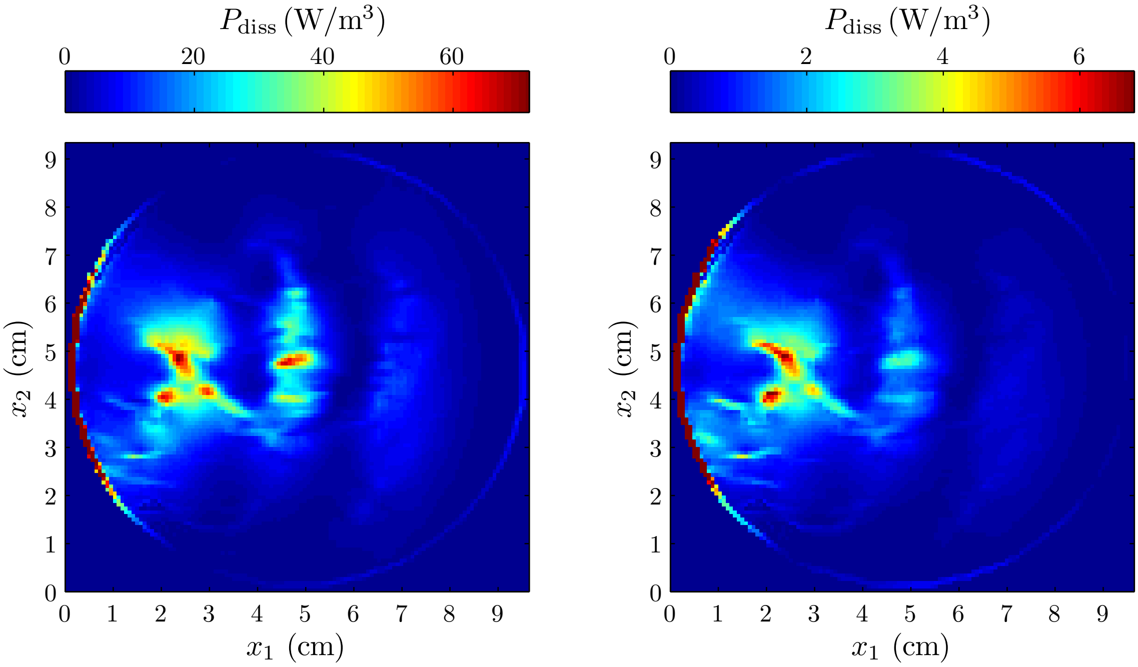

(a)

(b)

Fig. 6.20: At 2 GHz, the difference the first (a) and the second (b) eigenvalue method is clearly visible for the ablation of tumor A

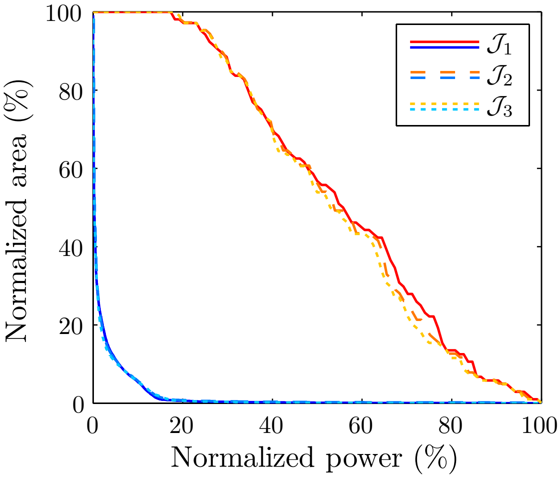

Fig. 6.21: The normalized cumulative power histograms of tumor B for the two eigenvalue methods and the conjugate gradient method with $\nu = 0.25$

6.4.2 Tumor B

The same investigation is performed for tumor B. The eigenvalues that result from the two eigenvalue methods appear to be distributed in the same fashion as the ones obtained for tumor A. The conjugate gradient method also showed the same convergence behavior as before.

The dissipated power patterns obtained with the three power optimization methods are illustrated in Fig. 6.22. Again, we see that the three power optimization methods yield approximately the same results. The power distributions are quite localized. Again, we see that it is difficult to heat the 'back' and the interior of the tumor. It is interesting to see that the power dissipation in the healthy tissue appears to actually increases in the eigenvalue method for $\mathcal{J}_2$ and even more for the conjugate gradient method.

The corresponding normalized cumulative power histograms are shown in Fig. 6.21. We see that reducing the power dissipated in the healthy tissue is again accompanied by a reduction of the power dissipated in the tumor. This reduction is also visible in the power dissipation pattern of Fig. 6.22c. From these graphs, we see again that the three methods yield approximately the same results. Apparently, for tumor B there is little room left for improvement as well.

We conclude again by investigating the actual temperature distribution. If we consider heating 95% of the tumor to at least 50 ℃, then 92.5% of the healthy tissue is kept within the range of physiologically safe temperatures.

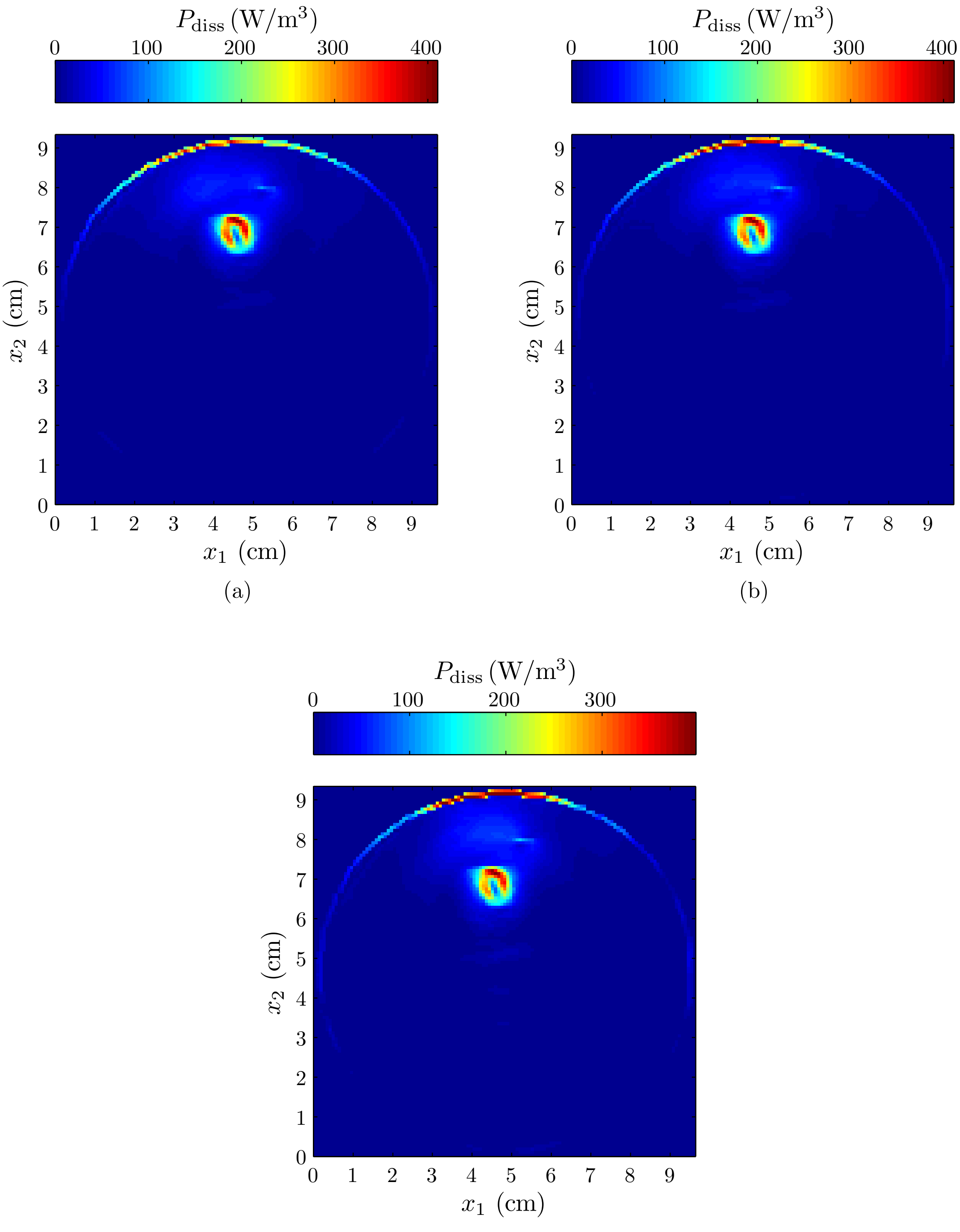

(a) (b) (c)

Fig. 6.22: The dissipated power density in the treatment of tumor B for the two eigenvalue methods (a,b) and the conjugate gradient method with $\nu = 0.25$ (c)

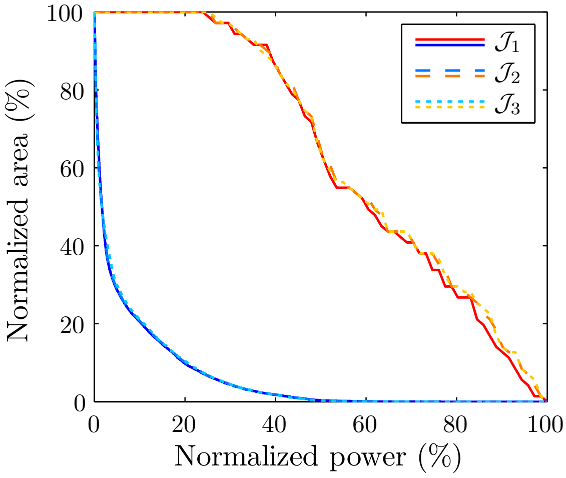

Fig. 6.23: The normalized cumulative power histograms of tumor C for the two eigenvalue methods and the conjugate gradient method with $\nu = 0.25$

6.4.3 Tumor C

Finally, the ablation of tumor C is investigated. The dissipated power patterns obtained with the three power optimization methods are illustrated in Fig. 6.24. Once again, the three power optimization methods yield approximately the same results. The normalized cumulative power histograms are shown in Fig. 6.23.

A more striking outcome of these simulations is the substantial increase of the power dissipation in the healthy tissue. In fact, the power dissipated in the healthy tissue renders the treatment of tumor C infeasible. If we would heat 95% of the tumor to more than 50°C, then only 80% of the healthy domain is kept below 43°C, an outcome which we consider to be insufficient for the ablation of tumor C. We figure that this is due to the deep location of the tumor. The attenuation in the breast tissue renders the suppression of hot spots in the healthy tissue to suffer.

We recall that the result of the frequency study in the beginning of this chapter was that the performance of the system depends strongly on the operational frequency. We also recall that this involved a trade-off between focal spot size and power transmission into the breast. In other words, since tumor C is located in a deeper part of the breast, we might consider using a lower frequency for the ablation of this tumor. For tumor B we might consider using another frequency as well. However, we expect that the optimal frequency for tumor B is approximately the same as for tumor A since both tumors are situated at approximately the same depth and within approximately the same surrounding.

Another frequency sweep has been performed for tumor C and also a smaller sweep for tumor B. The resulting variation of $\mathcal{J}_2(\boldsymbol{a}_1)$ for these sweeps is shown in Fig. 6.25a, together with results for tumor A. We see that the focusing ability of the system is optimal for tumor C at $f = 2$ to 3 GHz, and for tumor B at $f = 4$ to 5 GHz, just like tumor A. This result indicates that for the ablation of female breast tumors, we need to consider using different frequencies.

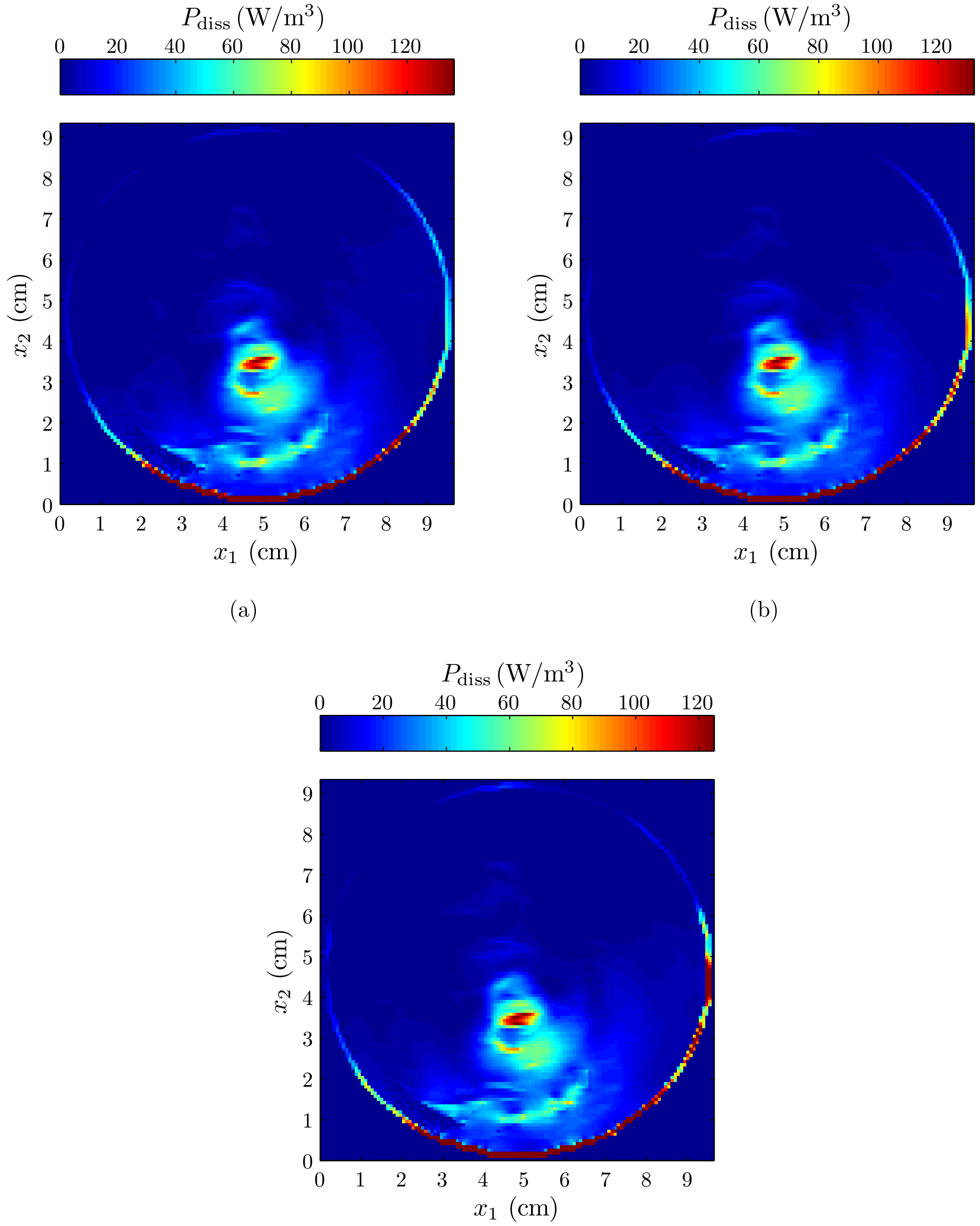

(a)

(b)

(c)

Fig. 6.24: The dissipated power density in the treatment of tumor C for the two eigenvalue methods (a,b) and the conjugate gradient method with $\nu = 0.25$ (c)

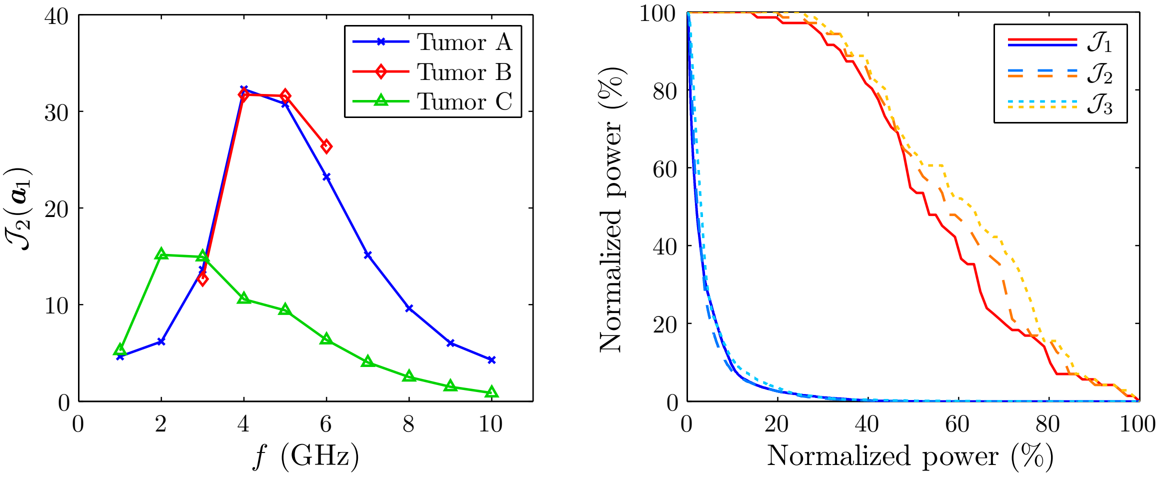

(a) (b)

Fig. 6.25: The frequency-dependent focusing ability of the system for the three tumors (a) the normalized cumulative power histograms of tumor C for $f = 2$ GHz

We have experienced that for the ablation of tumor C at 2 GHz, the best results of the conjugate gradient method were obtained for $\nu = 1.00$ as opposed to the previously found $\nu = 0.25$. The normalized cumulative power histograms for the two eigenvalue methods and the conjugate gradient method, with $\nu = 1.00$ and $f = 2$ GHz, are shown in Fig. 6.25b. The normalized cumulative power histograms obtained with the first two eigenvalue methods are shown in Fig. 6.23. The power distributions resulting from the second eigenvalue method at $f = 2$ and 3 GHz are shown in Fig. 6.26.

By evaluating the cumulative power histogram for $f = 2$ GHz, we can conclude that it is possible to heat 95% of the tumor to at least 50 ℃, while keeping 94.2% of the healthy tissue within the range of physiological temperatures. This result shows that it is possible to ablate even deep seated tumors using electromagnetic radiation.

6.5 Concluding remarks

In this chapter we have presented the results of various investigations concerning the ablation of female breast cancer. The main result is that it is possible to ablate a tumor that is seated at intermediate depth, using electromagnetic radiation at a frequency of 4 GHz. We have also shown that it is possible to ablate a tumor which is situated deep in the breast, using electromagnetic radiation at a frequency of 2 GHz.

Investigations on the various focusing algorithms did not yield big differences. The correct operation of the algorithms could still be shown nonetheless. It seemed as if the methods are performing equally well, when a localized power distribution is feasible at all. From this we conclude that the physical effects and system parameters play a bigger role in the thermal ablation of breast tumors than the focusing algorithm.

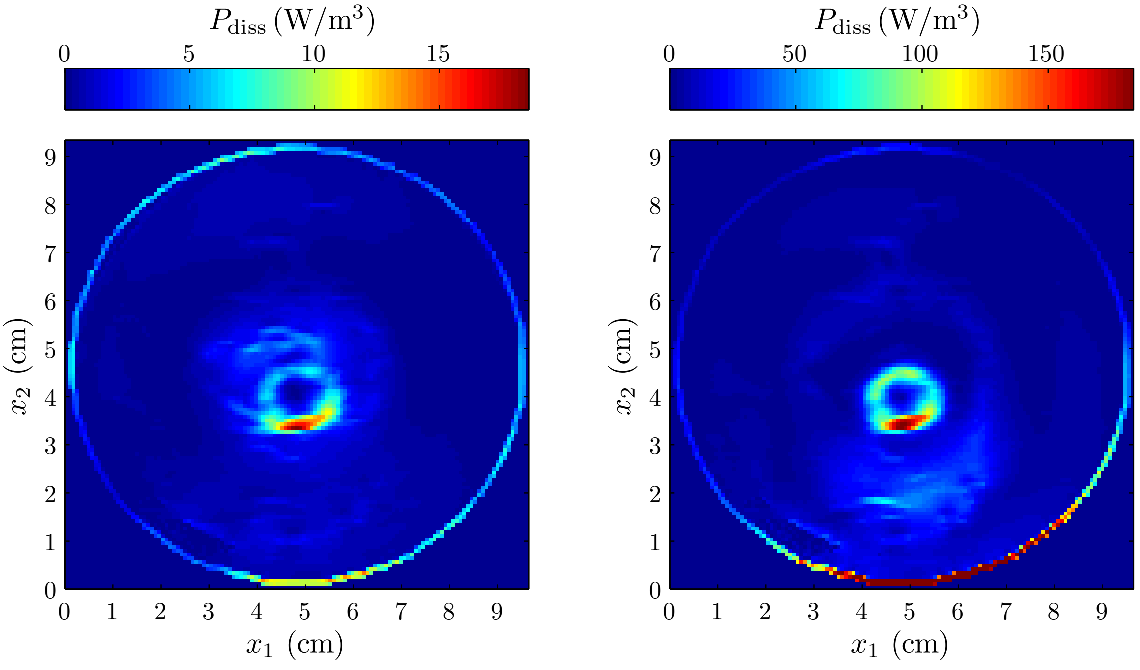

(a) (b)

Fig. 6.26: The dissipated power density resulting from the second eigenvalue method at $f = 2$ GHz (a) and $f = 3$ GHz (b) for tumor C

However, when undesired hot spots enter the configuration, differences between the performance of the algorithms may become of vital importance. We have seen that by taking the power dissipation in healthy tissue into account a lot of improvement can be obtained, however in these cases the feasibility of breast cancer ablation should be strongly questioned.

Chapter 7

Conclusions and recommendations

In this thesis we have assessed the feasibility of non-invasive electromagnetic ablation of female breast tumors. We have simulated a two-dimensional configuration with a circular array of line sources operating at a single frequency within the range of 1 to 10 GHz. We have incorporated a realistic model of the breast that accounts for the heterogeneous structure and the dispersive properties of the breast tissue. For computing the fields we have used the iterative conjugate gradient method for evaluating the discretized electric field integral equation (EFIE). Using this method together with one of the power optimization schemes, we have determined the optimal settings for the gridsize, bolus permittivity, operational frequency and number of sources.

Three power optimization methods have been presented in this work. The first method maximizes the power dissipated in the tumor and the second method maximizes this quantity with respect to the power dissipated in the healthy tissue. Both methods resulted in a closed form solution, namely that of an eigenvalue problem. The third method has been designed to improve a given power distribution by reducing the power dissipated in the healthy tissue while maintaining the focus in the tumor. This was done by iteratively minimizing a cost functional.

7.1 Conclusions

In this thesis it is shown that the non-invasive electromagnetic ablation of female breast tumors is possible. We have shown that tumors seated at intermediate depth can be ablated using electromagnetic radiation at a frequency of 4 GHz. We have also shown that it is possible to ablate a tumor which is situated deep in the breast, using electromagnetic radiation at a frequency of 2 GHz.

From the preliminary investigation we have found that the numerical dependence of the forward solver on the gridsize is quantized due to the use of the Fast Fourier Transform algorithm for computing the convolution integrals. Using the biggest gridsize that fits a certain FFT size yields the most accurate results without increasing the computational cost. We have also found that the optimal value of the bolus permittivity is located in between the permittivity of the skin and the permittivity of the adipose tissue. Simulation results suggest setting $\varepsilon_{\mathrm{r,b}} \approx 20$. We have also shown that using 32 sources is enough to assure optimal performance of the system.

Simulations with a homogeneous configuration have shown that the basic operation of the three power optimization algorithms is correct. The eigenvalue methods showed that eigenvectors corresponding to eigenvalues with approximately the same value can yield complementary power dissipation patterns. Combining these patterns can significantly improve the resulting power distribution.

Simulations with a realistic breast model showed that the three focusing algorithms do not yield significantly different results. From this we conclude that the physical effects and system parameters play a bigger role in the thermal ablation of breast tumors than the focusing algorithm.

However, when undesired hot spots enter the configuration, differences between the performance of the algorithms may become of vital importance. We have seen that by taking the power dissipation in healthy tissue into account a lot of improvement can be obtained, however, in these cases the feasibility of breast cancer ablation should still be strongly questioned.

7.2 Recommendations

The following follow-up research topics can be thought of:

- The investigation of different breast models deserves attention, for instance models of the class ‘heterogeneously scattered’ and ‘very dense’. These models may yield different results.

- We may include the dielectric properties of tumor tissue in the numerical breast model. Since the tumor exhibits 10% higher dielectric properties, this introduces more scattering and increases the local heating potential of the tumor.

- The investigation of the full 3D configuration or, as an intermediate step, the single-sided illumination of a sagittal cross section of the breast in a two-dimensional configuration can be interesting.

- Including thermal simulations to asses the damage deserves attention. The thermal models that we used to approximate the problem did not incorporate the tissue heterogeneity, as for the thermal parameters. Also, we note that the healthy tissue that is heated to more then 43°C is not directly ablated, since tissue damage increases exponentially with treatment time and temperature. Thus, to really assess the induced damage, we need accurate thermal simulations as well.

- We may investigate other cost functionals for the conjugate gradient power optimization method.
- It may be interesting to investigate the ablation problem as a vector optimization problem [2]. We can then investigate pareto optimal points of the problem.
- We may develop a conjugate gradient method that combines the computation of the total field with the optimization of the power distribution in one scheme. The basic idea for this is to steer the *total* incident field instead of one incident field per source. This way, one only needs to evaluate one EFIE and thus reduces the computational effort potentially with a factor of approximately $\frac{1}{S}$.
- We may investigate time domain optimization methods using a wideband signal. It is expected that some improvements can be obtained using this approach.
- The design of appropriate antennas for the implementation of a focused microwave ablation system can be done.
- Including a realistic antenna model in the investigated configuration is valuable.
- The feeding networks for phased array antennas often introduce quantized phase and amplitude shifts. It is therefore valuable to investigate the effect of phase and amplitude quantization on the power distribution.
- Assessing the effect of modeling errors on the power distribution deserves attention. In a realistic scenario, one can not assume that the propagation model is free of errors, for instance the patient could be moving or the breast model could include imaging artefacts.
- The power optimization methods can be applied to other physical domains like high intensity focused ultrasound.

This concludes our thesis on the feasibility of non-invasive electromagnetic ablation of female breast cancer. We hope that the research described in this thesis contributes to the further development of this modality for treating breast cancer.

Bibliography

[1] M. Abramowitz, and I.A. Stegun, *Handbook of mathematical functions with formulas, graphs and mathematical tables*, 9th ed., Dover Publications, New York, 1964.

[2] T.S. Angell, and A. Kirsch, "Optimization methods in electromagnetic radiation," Springer-Verlag, New York, USA, 2004.

[3] J.F. Bakker, "Heating breast tumors with an ultrasound or electromagnetic cylindrical phased-array," MSc Thesis, 2008.

[4] F. Bardati, A. Borrani, A. Gerardino, and G. A. Lovisolo, "SAR Optimization in a phased array radiofrequency hyperthermia system," *IEEE Trans. Biomed. Eng.*, vol. 42, no. 12, pp. 1201–1207, 1995.

[5] P.M. van den Berg, "Iterative schemes based on the minimization of the error in field problems," *Electromagnetics*, vol. 5, no. 2, pp. 237–262, 1985.

[6] A. Boag, and Y. Leviatan, "Analysis and optimization of waveguide multiapplicator hyperthermia systems," *IEEE Trans. Biomed. Eng.*, vol. 40, no. 9, pp. 946–952, 1993.

[7] A.Y. Cheung, and A. Neyzari, "Deep local hyperthermia for cancer therapy: external electromagnetic and ultrasound techniques," *Cancer Research (Suppl.)*, vol. 44, pp. 4736s–4744s, 1984.

[8] M. Converse, E.J. Bond, B.D. Van Veen, and S.C. Hagness, "A computational study of ultra-wideband versus narrowband microwave hyperthermia for breast cancer treatment," *IEEE Trans. Microw. Theory and Tech.*, vol. 54, no. 5, pp. 2169-2180, 2006.

[9] A.J. Fenn, and G.A. King, "An adaptive radio-frequency hyperthemia phased-array system for improved cancer therapy: phantom target measurements," Linc. Lab. J., vol. 6, no. 2, pp. 269287, 1993.

[10] A.J. Fenn, and G.A. King, "Experimental investigation of an adaptive feedback algorithm for hot spot reduction in radio-frequency phased array hyperthermia," *IEEE Trans. Biomed. Eng.*, vol. 43, no. 3, pp. 273–280, 1996.

[11] A.J. Fenn, V. Sathiaseelan, G.A. King, and P.R. Stauffer, "Improved localization of energy deposition in adaptive phased-array hyperthermia treatment of cancer," Linc. Lab. J., vol. 9, no. 2, pp. 187–196, 1996.

[12] F.S. Gayzik, E.P. Scott, and T. Loulou, "Experimental validation of an inverse heat transfer algorithm for optimizing hyperthermia treatment," J. Biom. Eng., vol. 128, no. 4, pp. 505–515, 2006.

[13] S.N. Goldberg, "Radiofrequency tumor ablation: principles and techniques," Eur. J. Ultrasound, vol. 13, pp. 129–147, 2001.

[14] Y. Gong, and G. Wang, "Superficial tumor hyperthermia with flat left-handed metamaterial lens," *Progr. In Electrom. Res.*, vol. 98, pp. 389–405, 2009.

[15] I.S. Gradshteyn, and I.M. Ryzhik, *Table of integrals, series and products*, 6th ed., A. Jeffrey and D. Zwillinger, eds., Academic Press, San Diego, 2000.

[16] B. Hildebrandt, P. Wust, O. Ahlers, et al., "The cellular and molecular basis of hyperthermia," Critical Reviews in Oncology/Hematology, vol. 43, pp. 33-56, 2002.

[17] I. Hilger, W. Andrä, R. Hergt, R. Hiergeist, H. Schubert, and W.A. Kaiser, "Electromagnetic heating of breast tumors in interventional radiology: in vitro and in vivo studies in human cadavers and mice," *Radiology*, issue 218, pp. 570–575, 2001.

[18] I. Hilger, R. Hergt, and W.A. Kaiser, "Use of magnetic nanoparticle heating in the treatment of breast cancer," *IEE Proc. Nanobiotechnol.*, vol. 152, no. 1, pp. 33–39, 2005.

[19] A.T. de Hoop, *Handbook of radiation and scattering of waves*, Academic press, London, UK, 1995.

[20] T. Huttunen, J.P. Kaipio, and M. Malinen, "Optimal control in high intensity focused ultrasound surgery," C.J.S. Alves, P.M. Pardalos, eds., Optimization in Medicine, Springer, 2008.

[21] D.S. Kapp, "Efficiacy of adjuvant hyperthermia in the treatment of superficial recurrent breast cancer: confirmation and future directions," Int. J. Radiation Oncology Biol. Phys., vol. 35, pp. 1117–1121, 1996.

[22] R.E. Kleinman, and P.M. van den Berg, "Iterative methods for solving integral equations," *Application of Conjugate Gradient Method to Electromagnetic and Signal Analysis*, ed. T.K. Sarkar, *Progr. In Electrom. Res.*, vol. 5, Elsevier, New York, USA, pp. 67–102, 1991.

[23] J. Kremer, and A.K. Louis, "On the mathematical foundations of hyperthermia therapy," *Math. Meth. Appl. Sci.*, vol. 13, pp. 467–479, 1990.

[24] T. Köhler, P. Maass, P. Wust, and M. Seebass, "A fast algorithm to find optimal controls of multiantenna applicators in regional hyperthermia," *Phys. Med. Biol.*, vol. 46, pp. 2503-2514, 2001.

[25] B.J. Kooij, and P.M. van den Berg, "Nonlinear inversion in TE scattering," *IEEE Trans. Microw. Theory and Tech.*, vol. 46, no. 11, pp. 1704–1712, 1998.

[26] M.E. Kowalski, B. Behnia, A.G. Webb, and J.M. Jin, "Optimization of electromagnetic phased-arrays for hyperthermia via magnetic resonance temperature estimation," *IEEE Trans. Biomed. Eng.*, vol. 49, no. 11, pp. 1229–1241, 2002.

[27] M.E. Kowalski, and J.M. Jin, "Model-based optimization of phased arrays for electromagnetic hyperthermia," *IEEE Trans. Micr. Th. Tech.*, vol. 52, no. 8, pp. 1964–1977, 2004.

[28] I.E. Lager, and B.J. Kooij, "Non-linear Imaging Algorithm for the Detection of Female Breast Cancer in the Incipient State," Proc. European Microwave Week, Paris, France, pp. 217–220, 2005.

[29] M. Lazebnik, M.C. Converse, J.H. Booske, and S.C. Hagness, "Ultrawideband temperature-dependent dielectric properties of animal liver tissue in the microwave frequency range," *Phys. Med. Biol.*, vol. 51, pp. 1941-1955, 2006.

[30] M. Lazebnik, L. McCartney, D. Popovic, C.B. Watkins, M.J. Lindstrom, J. Harter, S. Sewall, A. Magliocco, J.H. Booske, M. Okoniewski, and S.C. Hagness, "A large-scale study of the ultrawideband microwave dielectric properties of normal breast tissue obtained from reduction surgeries," *Phys. Med. Biol.*, vol. 52, pp. 2637-2656, 2007.

[31] M. Lazebnik, D. Popovic, L. McCartney, C.B. Watkins, M.J. Lindstrom, J. Harter, S. Sewall, T. Ogilvie, A. Magliocco, T.M. Breslin, W. Temple, D. Mew, J.H. Booske, M. Okoniewski, and S.C. Hagness, "A large-scale study of the ultrawideband microwave dielectric properties of normal, benign and malignant breast tissues obtained from cancer surgeries," *Phys. Med. Biol.*, vol. 52, pp. 6093-6115, 2007.

[32] T. Loulou, and E.P. scott, "Thermal dose optimization in hyperthermia treatments by using the conjugate gradient method," Numerical Heat Transfer, Part A: Applications, 42: 7, pp. 661–683, 2002.

[33] J.T. Loane, H. Ling, B.F. Wang, and S.W. Lee, "Experimental investigation of a retro-focusing microwave hyperthermia applicator: conjugate field matching scheme," *IEEE Trans. Micr. Th. Tech.*, vol. MTT-34, no. 5, pp. 490–494, 1986.

[34] J.T. Loane, and S.W. Lee, "Gain optimization of a near-field focusing array for hyperthermia applications," *IEEE Trans. Micr. Th. Tech.*, vol. 37, no. 10, pp. 1629–1635, 1989.

[35] S. Marburg, "Discretization requirements: How many Elements per wavelength are necessary?," S. Marburg, B. Notl, eds.,Computational acoustics of noise propagation in fluids: finite and boundary element methods C.J.S. Alves, P.M. Pardalos, eds., Optimization in Medicine, Springer, 2008.

[36] J. Overgaard, and O.S. Nielsen, "The importance of thermotolerance for the clinical treatment with hyperthermia," Radiother. Oncol., vol. 7, pp. 167–178, 1983.

[37] W. Schramm, D. Yang, B.J. Wood, F. Rattay, and D. Haemmerich, "Contribution of direct heating, thermal conduction and perfusion during radiofrequency and microwave ablation," Open Biomed. Eng. J., vol. 1, pp. 47–52, 2007.

[38] M. Seebass, R. Beck, J. Gellermann, J. Nadobny, and P. Wust, "Electromagnetic phased arrays for regional hyperthermia optimal frequency and antenna arrangement," Int. J. Hyperth., vol. 17, no. 4, pages 321–336, 2001.

[39] D. Ward, D. Burton, A. Craig, J. Day, C. Dimmer, H. Lynn, and M. Parnell, Breast cancer: an environmental disease, 2005. Available: www.nomorebreastcancer.org.uk

[40] A.S. Wright, L.A. Sampson, T.F. Warner, D.M. Mahvi, and F.T. Lee, Jr., "Radiofrequency versus microwave ablation in a hepatic porcine model," *Radiology*, vol. 236, no. 1, pp. 132–139, 2005.

[41] L. Wu, R.J. McGough, O.A. Arabe, and T.V. Samulski, "An RF phased array applicator designed for hyperthermia breast cancer treatments," *Phys. Med. Biol.*, vol. 51, no. 1, pp. 1-20, 2006.

[42] P. Wust, and J. Gellermann, "Regional thermotherapy," in *Regional Cancer Therapy*, P.M. Schlag, U.S. Stein, Totowa: Humana Press Inc., pp. 73–90, 2007.

[43] E. Zastrow, S.K. Davis, M. Lazebnik, F. Kelcz, B.D. Van Veen, and S.C. Hagness, "Development of anatomically realistic numerical breast phantoms with accurate dielectric properties for modeling microwave interactions with the human breast," *IEEE Trans. Biomed. Eng.*, vol. 55, no. 12, pp. 2792–2800, 2008.

[44] E. Zastrow, S.K. Davis, M. Lazebnik, F. Kelcz, B.D. Van Veen, and S.C. Hagness, "Database of 3D grid-based numerical breast phantoms for use in computational electromagnetics simulations," Instruction manual, Department of Electrical and Computer Engineering, University of Wisconsin-Madison, 2007.

[45] J. van der Zee, "Heating the patient: a promising approach?," Annals of Oncology, vol. 13, pp. 1173–1184, 2002.

[46] A.P.M. Zwamborn, "Scattering by objects with electric contrast," Ph.D. dissertation, Delft University Press, ISBN 90-6275-691-3/CIP, ch. 4, pp. 69–74, 1991.

[47] A.P.M. Zwamborn, and P.M. van den Berg, "A weak form of the Conjugate Gradient FFT method for two-dimensional TE scattering problems," *IEEE Transactions on Microwave Theory and Techniques*, vol. 39, no. 6, pp. 953–960, 1991.

Appendix A

Tissue thermodynamics

This appendix treats the relationship between electromagnetic energy dissipation and the resulting tissue temperature. This relation would give us an indication on the amount of power needed to achieve coagulative necrosis in the tumor tissue. It would also set the maximal level of power dissipation allowed in the healthy tissue in order not to cause any cell damage.

The transfer of heat in tissue can be modeled by the bioheat equation of Pennes, which accounts for heat conduction, blood perfusion and metabolic heat production. It is given by

$$\rho c \frac{\partial T}{\partial t} = \nabla \cdot k \nabla T + Q_{\mathrm{m}} + P_{\mathrm{diss}} - w_{\mathrm{b}} c_{\mathrm{b}} (T - T_{\mathrm{b}}) \tag{A.1}$$

in which ρ represents the tissue density, c is the specific heat, the variable T denotes the temperature, t stands for the time-instant, k is the thermal conductivity of the tissue, Q_{m} represents metabolic heat production, P_{diss} denotes the dissipated electromagnetic power, w_{b} represents the blood perfusion rate, c_{b} the specific heat of the blood and T_{b} denotes the blood temperature. The solution to this differential equation describes the resulting temperature distribution during treatment, and can give an indication for the power needed to obtain coagulative necrosis in the tumor tissue. The relevant tissue parameters are given in Table A.1 [8].

Several clinical studies have compared the influence of blood perfusion and heat conduction on the resulting temperature distribution in radiofrequency ablation and microwave ablation [37, 40]. These investigations show that in microwave tumor ablation the final temperature in the tumor is less affected by blood perfusion and thermal con-

Table A.1: Thermal parameters for breast tissue and tumor tissue

Media	ρ [kg m^{-3}]	c [J kg^{-1} K^{-1}]	k [W m^{-1} K^{-1}]	Q_{m} [W m^{-3}]	$w_{\mathrm{b}} c_{\mathrm{b}}$ [W m^{-3} K^{-1}]
Tumor	1182	3049	0.496	5500	5350
Breast	1069	2279	0.306	350	2229

duction due to the short treatment time. It has been shown that the tissue temperature depends mostly on the locally dissipated power, even when the heated tissue is close to large vasculature structures.

For investigating the power needed to raise the tumor temperature to 50 ℃, we will first assume that the heat conduction and blood perfusion is of negligible influence on the obtained temperature. We will also assume that metabolic heating is of an insignificant influence on the resulting temperature distribution. Removing these terms reduces Eq. (A.1) to

$$\rho c \frac{\partial T}{\partial t} = P_{\mathrm{diss}} \tag{A.2}$$

Solving this differential equation yields

$$T(t_{\mathrm{f}}) = T(t_0) + \frac{1}{\rho c} \int_{t_0}^{t_{\mathrm{f}}} P_{\mathrm{diss}}(t) \mathrm{d}t \tag{A.3}$$

where t_0 and t_{f} represent the starting end ending instant, respectively. Since the dissipated power is approximately constant during the treatment, we can derive the following relation between the dissipated power and the temperature increase

$$\Delta T = \frac{1}{\rho c} P_{\mathrm{diss}} \Delta t \tag{A.4}$$

where $\Delta t = t_{\mathrm{f}} - t_0$ represents the treatment duration and $\Delta T = T(t_{\mathrm{f}}) - T(t_0)$ denotes the local temperature increase.

First we will consider the tumor tissue. If we assume $T(t_0) = 37$ ℃, $T(t_{\mathrm{f}}) \geq 50$ ℃ and a treatment duration of 10 seconds, then we would need to obtain a dissipated power density of at least $4.7 \cdot 10^6$ W/m^3 in order to induce coagulative necrosis. So to ablate a tumor of 1 cm^3 in size within 10 seconds, we would need to dissipate at least 4.7 W in the tumor. This is a feasible number considering the use an antenna array.

While heating the tumor tissue, we will need to constrain the dissipated power density in the healthy tissue in order to prevent irreversible damage there. By setting $T(t_{\mathrm{f}}) \leq$ 43 ℃ we find the maximal dissipated power density in healthy tissue to be $1.5 \cdot 10^6$ W/m^3.

To review our simplification of the bioheat equation, we will compare the dissipated power density P_{diss} with the other terms that prevail in the right hand side of Eq. A.1. It turns out that when we fill in the relevant parameters, the other terms that contribute to the differential equation are orders of magnitude smaller than the source term. Eq. (A.4) is therefore a valid approximation of the Pennes bioheat equation.

With the simplified bioheat equation we can derive a quantative goal which needs to be satisfied by an ablation system. Essentially, we want to achieve a *minimal* temperature of 50 ℃ in the tumor tissue together with a *maximal* temperature of 43 ℃ in the healthy tissue. Since the temperature increases linearly with the dissipated power density, we can form a quantative goal in terms of the *minimal* dissipated power density in the tumor tissue and the *maximal* dissipated power density in the healthy tissue. This results in

$$\frac{\min P_{\mathrm{diss,t}}}{\max P_{\mathrm{diss,h}}} \leq \frac{\rho_{\mathrm{t}} c_{\mathrm{t}} \Delta T_{\mathrm{t}}}{\rho_{\mathrm{h}} c_{\mathrm{h}} \Delta T_{\mathrm{h}}} = 3.2 \tag{A.5}$$

where the subscripts t and h denote the tumor tissue and healthy tissue, respectively. This number can be used as a figure of merit and can serve as a quantified goal for the focusing algorithm.

Appendix B

Two-dimensional Green's function

In this appendix we will derive the Green's function in the two-dimensional spatial domain. In Chapter 2 we obtained an expression for the Green's function in the angular wave vector domain, Eq. (2.55), repeated here for convenience

$$\tilde{g}(\boldsymbol{k}, \omega) = \frac{1}{\boldsymbol{k} \cdot \boldsymbol{k} - \hat{k}_{\mathrm{b}}^2} \tag{B.1}$$

where $\boldsymbol{k} \in \mathbb{R}^2$ and $\hat{k}_{\mathrm{b}}$ denotes the complex wavenumber in the background medium. Since we consider a non-magnetic background medium, we have $\hat{k}_{\mathrm{b}}(\omega) = \omega\sqrt{\mu_0 \hat{\varepsilon}_{\mathrm{b}}(\omega)}$. This leaves two possible solutions for $\hat{k}_{\mathrm{b}}$ depending on how one defines the square root. By defining the Laplace transform for $\mathrm{Re}\{s\} \geq 0$ we also have the condition $\mathrm{Im}\{\hat{\varepsilon}_{\mathrm{b}}(\omega)\} \leq 0$. We then simply choose to take the principal square root with $-\pi < \arg\{\hat{\varepsilon}_{\mathrm{b}}\} \leq \pi$ which results in $\mathrm{Im}\{\hat{k}_{\mathrm{b}}\} \leq 0$.

We can now start our derivation by applying the two-dimensional inverse spatial Fourier transform to $\tilde{g}$

$$\hat{g}(\boldsymbol{x}, \omega) = \mathcal{F}_{\boldsymbol{k}}^{-1}\{\tilde{g}(\boldsymbol{k}, \omega)\} = \frac{1}{(2\pi)^2} \int\limits_{\boldsymbol{k} \in \mathbb{R}^2} \tilde{g}(\boldsymbol{k}, \omega) \mathrm{e}^{\mathrm{j}\boldsymbol{k} \cdot \boldsymbol{x}} \mathrm{d}A\,. \tag{B.2}$$

By using the parameterization $\boldsymbol{k} = \boldsymbol{i}_1 \kappa \cos\theta + \boldsymbol{i}_2 \kappa \sin\theta$ and $\boldsymbol{x} = \boldsymbol{i}_1 r \cos\phi + \boldsymbol{i}_2 r \sin\phi$, where $\kappa = |\boldsymbol{k}|$ and $r = |\boldsymbol{x}|$, we see that we can rewrite Eq. (B.2) as

$$\begin{aligned}
\hat{g}(\boldsymbol{x}, \omega) &= \frac{1}{(2\pi)^2} \int_0^{2\pi} \int_0^{\infty} \frac{1}{\kappa^2 - \hat{k}_{\mathrm{b}}^2} \mathrm{e}^{\mathrm{j}\kappa r \cos(\theta - \phi)} \kappa \mathrm{d}\kappa \mathrm{d}\theta \\
&= \frac{1}{(2\pi)^2} \int_0^{2\pi} \int_0^{\infty} \frac{\kappa}{\kappa^2 - \hat{k}_{\mathrm{b}}^2} \mathrm{e}^{\mathrm{j}\kappa r \cos\theta} \mathrm{d}\kappa \mathrm{d}\theta \\
&= \frac{1}{2\pi} \int_0^{\infty} \frac{\kappa}{\kappa^2 - \hat{k}_{\mathrm{b}}^2} J_0(\kappa r) \mathrm{d}\kappa
\end{aligned} \tag{B.3}$$

which is in fact a Hankel transform of order zero. In order to arrive at this expression we have recognized the integral representation of the Bessel function of the first kind and order zero, which is defined for complex arguments as

$$J_0(z) = \frac{1}{2\pi}\int_0^{2\pi} \mathrm{e}^{\mathrm{j}z\cos\theta}\mathrm{d}\theta\,. \tag{B.4}$$

Using the expressions for the Hankel functions of the first and second kind

$$H_n^{(1)}(z) = J_n(z) + \mathrm{j}Y_n(z) \tag{B.5}$$

$$H_n^{(2)}(z) = J_n(z) - \mathrm{j}Y_n(z) \tag{B.6}$$

we can write

$$J_0(z) = \tfrac{1}{2}(H_0^{(1)}(z) + H_0^{(2)}(z))\,. \tag{B.7}$$

After substituting this expression in Eq. (B.3) we arrive at

$$\hat{g}(\boldsymbol{x},\omega) = \frac{1}{4\pi}\int_0^{\infty} \frac{\kappa}{\kappa^2 - \hat{k}_\mathrm{b}^2}\left[H_0^{(1)}(\kappa r) + H_0^{(2)}(\kappa r)\right]\mathrm{d}\kappa\,. \tag{B.8}$$

Hankel functions are known to be multiple valued functions having $\kappa r = 0$ as a branch point. By designating the branch cut at $(-\infty, 0)$ in the complex κ-plane, we can use the following relation along the lower side of the interval $(0,\infty)$ [15]

$$\begin{aligned} H_0^{(1)}(z) &= -H_0^{(2)}(z\mathrm{e}^{-\mathrm{j}\pi}) \\ &= -H_0^{(2)}(-z) \end{aligned} \tag{B.9}$$

which is inserted in Eq. (B.8) as follows

$$\begin{aligned} \hat{g}(\boldsymbol{x},\omega) &= \frac{1}{4\pi}\int_0^{\infty} \frac{\kappa}{\kappa^2 - \hat{k}_\mathrm{b}^2}\left[H_0^{(2)}(\kappa r) - H_0^{(2)}(-\kappa r)\right]\mathrm{d}\kappa \\ &= \underbrace{\fint_{-\infty}^{\infty} \frac{1}{4\pi}\frac{\kappa}{\kappa^2 - \hat{k}_\mathrm{b}^2} H_0^{(2)}(\kappa r)}_{f(\kappa)}\,\mathrm{d}\kappa\,. \end{aligned} \tag{B.10}$$

We need to formulate the latter integral as a principal value integral since the integrand $f(\kappa)$ is not defined at $\kappa = 0$.

We compute Eq. (B.10) analytically based on a contour integration technique. We note that the integrand $f(\kappa)$ has two poles at $\kappa = \pm\hat{k}_\mathrm{b}$. Since we defined the complex wavenumber with $\mathrm{Im}\{\hat{k}_\mathrm{b}\} \leq 0$, we find $\hat{k}_\mathrm{b}$ in the lower half-plane. One specific problem arises when the complex wavenumber is purely real, for instance in case of a lossless

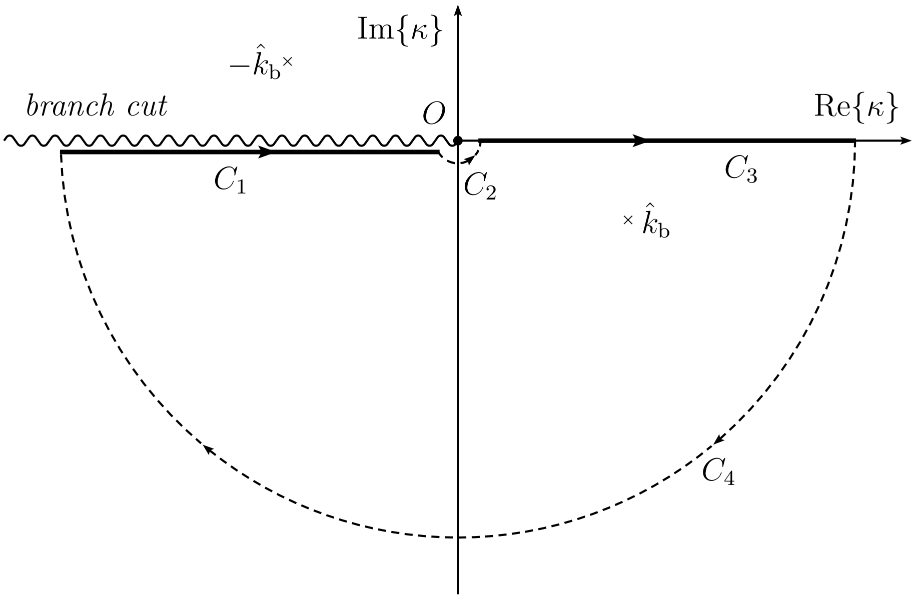

Fig. B.1: Integration contour C in the complex κ-plane

background medium. This case introduces two poles on the integration path, where one of them is actually on the branch cut, which will make this derivation rather tedious. We will therefore assume that our background medium exhibits infinitesimal losses, and thus $\mathrm{Im}\{\hat{k}_\mathrm{b}\} < 0$ holds.

We choose to integrate along a contour C in the lower half of the complex κ-plane, which is the union of C_1, C_2, C_3 and C_4 as shown in Fig. B.1. In order to keep the integrand analytic and single valued, the contour may not intersect the branch cut. Hence, C_1 runs just below the branch cut and C_2 encircles the branch point $\kappa = 0$ tightly.

By performing the contour integration along the contour C in the complex κ-plane, bearing in mind that this contour encircles the pole $\hat{k}_\mathrm{b}$ in a clockwise direction, we can now apply the theorem of residues

$$\int\limits_C f(\kappa)\mathrm{d}\kappa = -2\pi\mathrm{j}\,\mathrm{Res}\left[f(\kappa);\kappa = \hat{k}_\mathrm{b}\right] . \tag{B.11}$$

Since the integrand $f(\kappa)$ is continuous on C, the contour along C_1 and C_3 will give us the integral that we want to evaluate, Eq. (B.10). Hence, we only need to evaluate the integrals along C_2 and C_4 and the residual in order to obtain our result.

At contour C_2, κ circumvents the origin tightly from below in counterclockwise direction. In order to evaluate this integral, we parameterize κ in polar coordinates as $\kappa = \epsilon \mathrm{e}^{\mathrm{j}\phi}$ with $\epsilon \downarrow 0$. We then use the limiting form of the Hankel function $H_0^{(2)}(z)$ for small arguments [1] in order to obtain

$$
\begin{aligned}
\lim_{\epsilon\downarrow 0} \oint_{|\kappa|=\epsilon} f(\kappa)\mathrm{d}\kappa &= \frac{1}{4\pi} \lim_{\epsilon\downarrow 0} \int_{-\pi}^{0} \frac{\epsilon \mathrm{e}^{\mathrm{j}\phi}}{\epsilon^2 \mathrm{e}^{\mathrm{j}2\phi} - \hat{k}_{\mathrm{b}}^2} H_0^{(2)}(r\epsilon \mathrm{e}^{\mathrm{j}\phi})\mathrm{d}\phi \\
&= \frac{-1}{4\pi \hat{k}_{\mathrm{b}}^2} \lim_{\epsilon\downarrow 0} \epsilon \int_{-\pi}^{0} \mathrm{e}^{\mathrm{j}\phi} \left[1 - \mathrm{j}\frac{2}{\pi}\left\{\ln\left(\frac{r\epsilon \mathrm{e}^{\mathrm{j}\phi}}{2}\right) + \gamma\right\}\right] \mathrm{d}\phi \\
&= \frac{-1}{4\pi \hat{k}_{\mathrm{b}}^2} \lim_{\epsilon\downarrow 0} \epsilon \int_{-\pi}^{0} \mathrm{e}^{\mathrm{j}\phi} \left[1 - \mathrm{j}\frac{2}{\pi}\left\{\ln\epsilon + \ln\left(\frac{r \mathrm{e}^{\mathrm{j}\phi}}{2}\right) + \gamma\right\}\right] \mathrm{d}\phi \\
&= \frac{1}{4\pi \hat{k}_{\mathrm{b}}^2} \lim_{\epsilon\downarrow 0} \epsilon \int_{-\pi}^{0} \mathrm{e}^{\mathrm{j}\phi} \left[\mathrm{j}\frac{2}{\pi}\ln\epsilon\right] \mathrm{d}\phi \\
&= \frac{1}{\pi^2 \hat{k}_{\mathrm{b}}^2} \lim_{\epsilon\downarrow 0} \epsilon \ln\epsilon \\
&= 0
\end{aligned}
\tag{B.12}
$$

with γ denoting Euler's constant. We have evaluated the resulting limit using l'Hôpital's rule as follows

$$
\lim_{\epsilon\downarrow 0} \epsilon\ln\epsilon = \lim_{\epsilon\downarrow 0} \frac{\ln\epsilon}{1/\epsilon} = \lim_{\epsilon\downarrow 0} \frac{1/\epsilon}{-1/\epsilon^2} = -\lim_{\epsilon\downarrow 0} \epsilon = 0\,. \tag{B.13}
$$

In order to evaluate the integral over C_4, we parameterize κ in polar coordinates as $\kappa = R\mathrm{e}^{\mathrm{j}\phi}$ with $R \to \infty$ and use the asymptotic form of the Hankel function $H_0^{(2)}(\kappa)$ for large arguments [1], given by

$$
H_0^{(2)}(\kappa) \sim \sqrt{\frac{2}{\pi\kappa}} \mathrm{e}^{-\mathrm{j}(\kappa - \frac{\pi}{4})}\,. \tag{B.14}
$$

Since the integrand goes to zero on C_4, the integral over C_4 also vanishes.

Now, since the contributions of the integrals over C_2 and C_4 are zero, the result of Eq. (B.10) is equal to Eq. (B.11), and we have thus found the Green's function in the frequency domain as

$$
\begin{aligned}
\hat{g}(\boldsymbol{x}, \omega) &= -2\pi\mathrm{j}\,\mathrm{Res}\left[\frac{1}{4\pi}\frac{\kappa}{(\kappa + \hat{k}_{\mathrm{b}})(\kappa - \hat{k}_{\mathrm{b}})} H_0^{(2)}(\kappa r); \kappa = \hat{k}_{\mathrm{b}}\right] \\
&= -\frac{\mathrm{j}}{4} H_0^{(2)}(\hat{k}_{\mathrm{b}}|\boldsymbol{x}|)\,.
\end{aligned}
\tag{B.15}
$$

We note that since $\mathrm{Im}\{\hat{k}_{\mathrm{b}}\} < 0$, the Green's function will decay to zero when $|\boldsymbol{x}| \to \infty$ and thus this solution is physically correct. This is even the case when we consider a lossless background with $\mathrm{Im}\{\hat{k}_{\mathrm{b}}\} = 0$. Hence, we assume this solution is valid for $\mathrm{Im}\{\hat{k}_{\mathrm{b}}\} \leq 0$.

Appendix C

Weak form of the Green's function

In the discretization of the EFIE we have encountered a specific challenge, namely the weakening of the two-dimensional Green's function g. In this appendix we will describe how weak form of the Green's function is obtained.

In the weakening procedure we replace g by its mean value over a circular domain with center point $\boldsymbol{x}_{m,n} - \boldsymbol{x}_{m',n'} = \boldsymbol{x}$ and radius $\frac{1}{2}\Delta x = \frac{1}{2}\mathrm{min}(\Delta x_1, \Delta x_2)$, after which the weak form of the Green's function is denoted by $\mathcal{G}$, viz.

$$\begin{aligned} \mathcal{G}(\boldsymbol{x}) &= \frac{4}{\pi(\Delta x)^2} \int\limits_{|\boldsymbol{x}''| < \frac{1}{2}\Delta x} g(\boldsymbol{x} + \boldsymbol{x}'')\mathrm{d}V \\ &= -\frac{\mathrm{j}}{\pi(\Delta x)^2} \int\limits_{|\boldsymbol{x}''| < \frac{1}{2}\Delta x} H_0^{(2)}(k_\mathrm{b}|\boldsymbol{x} + \boldsymbol{x}''|)\mathrm{d}V \,. \end{aligned} \tag{C.1}$$

By using the summation theorem for Bessel functions [15] we can rewrite the Hankel function that appears in the integrand as

$$H_0^{(2)}(k_\mathrm{b}|\boldsymbol{x} + \boldsymbol{x}''|) = \begin{cases} \displaystyle\sum_{k=-\infty}^{\infty} J_k(k_\mathrm{b}|\boldsymbol{x}|)H_k^{(2)}(k_\mathrm{b}|\boldsymbol{x}''|)\mathrm{e}^{\mathrm{j}k\phi} & \forall \quad |\boldsymbol{x}''| \geq |\boldsymbol{x}| \\ \displaystyle\sum_{k=-\infty}^{\infty} J_k(k_\mathrm{b}|\boldsymbol{x}''|)H_k^{(2)}(k_\mathrm{b}|\boldsymbol{x}|)\mathrm{e}^{\mathrm{j}k\phi} & \forall \quad |\boldsymbol{x}''| \leq |\boldsymbol{x}| \end{cases} \tag{C.2}$$

where ϕ denotes the angle between $\boldsymbol{x}$ and $\boldsymbol{x}''$ as depicted in Fig. C.1.

Singular case

In the singular case we have $\boldsymbol{x} = \boldsymbol{0}$. Since the Hankel function $H_0^{(2)}(|\boldsymbol{x}+\boldsymbol{x}''|)$ is not defined at $|\boldsymbol{x} + \boldsymbol{x}''| = 0$, we will have to formulate the integral as a limit where $\boldsymbol{x} \to \boldsymbol{0}$. With this

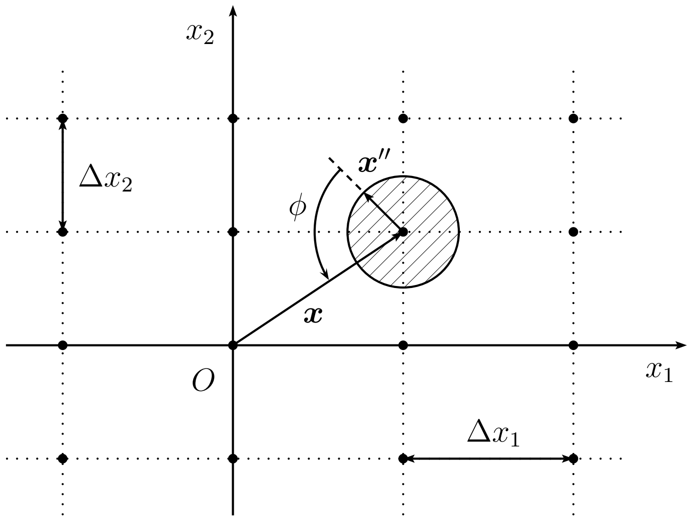

Fig. C.1: Weakening configuration

limit, one part of the integration interval will satisfy $|\boldsymbol{x}''| \leq |\boldsymbol{x}|$ and the other part will satisfy $|\boldsymbol{x}''| \geq |\boldsymbol{x}|$. We will thus have to split the integral and use both cases of Eq. (C.2).

By using polar coordinates with $|\boldsymbol{x}''| = r$ and $|\boldsymbol{x}| = \epsilon$, and noting that the terms with $k \neq 0$ drop out due to the integration over ϕ, we can rewrite Eq. (C.1) as

$$\mathcal{G}(\mathbf{0}) = \lim_{\epsilon \to 0} -\frac{2\mathrm{j}}{(\Delta x)^2}\left[H_0^{(2)}(k_\mathrm{b}\epsilon)\int_0^{\epsilon} J_0(k_\mathrm{b}r)r\mathrm{d}r + J_0(k_\mathrm{b}\epsilon)\int_{\epsilon}^{\frac{1}{2}\Delta x} H_0^{(2)}(k_\mathrm{b}r)r\mathrm{d}r\right]. \tag{C.3}$$

By using the formulas for derivatives [1], which gives us the relation $z^n\mathscr{C}_{n-1}^{(2)}(z) = \frac{\mathrm{d}}{\mathrm{d}z}[z^n\mathscr{C}_n^{(2)}(z)]$ where $\mathscr{C}_n$ denotes the Bessel function J_n or the Hankel function $H_n^{(1,2)}$, and the Wronskian relation $J_{n+1}(z)Y_n(z) - J_n(z)Y_{n+1}(z) = 2/\pi z$, we find the following

$$\begin{aligned}
\mathcal{G}(\mathbf{0}) &= \lim_{\epsilon \to 0} -\frac{2\mathrm{j}}{(\Delta x)^2}\left[\frac{1}{k_\mathrm{b}}H_0^{(2)}(k_\mathrm{b}\epsilon)\Big[rJ_1(k_\mathrm{b}r)\Big]_{r=0}^{r=\epsilon} + \frac{1}{k_\mathrm{b}}J_0(k_\mathrm{b}\epsilon)\Big[rH_1^{(2)}(k_\mathrm{b}r)\Big]_{r=\epsilon}^{r=\frac{1}{2}\Delta x}\right] \\
&= \lim_{\epsilon \to 0} -\frac{2\mathrm{j}}{(\Delta x)^2}\left[\frac{\frac{1}{2}\Delta x}{k_\mathrm{b}}J_0(k_\mathrm{b}\epsilon)H_1^{(2)}(\tfrac{1}{2}k_\mathrm{b}\Delta x) - \frac{2\mathrm{j}}{\pi k_\mathrm{b}^2}\right] \\
&= -\frac{\mathrm{j}}{k_\mathrm{b}\Delta x}\left[H_1^{(2)}(\tfrac{1}{2}k_\mathrm{b}\Delta x) - \frac{4\mathrm{j}}{\pi k_\mathrm{b}\Delta x}\right]
\end{aligned} \tag{C.4}$$

where we have used the series expansion of $J_0(k_\mathrm{b}r)$ [1] in order to evaluate the limit.

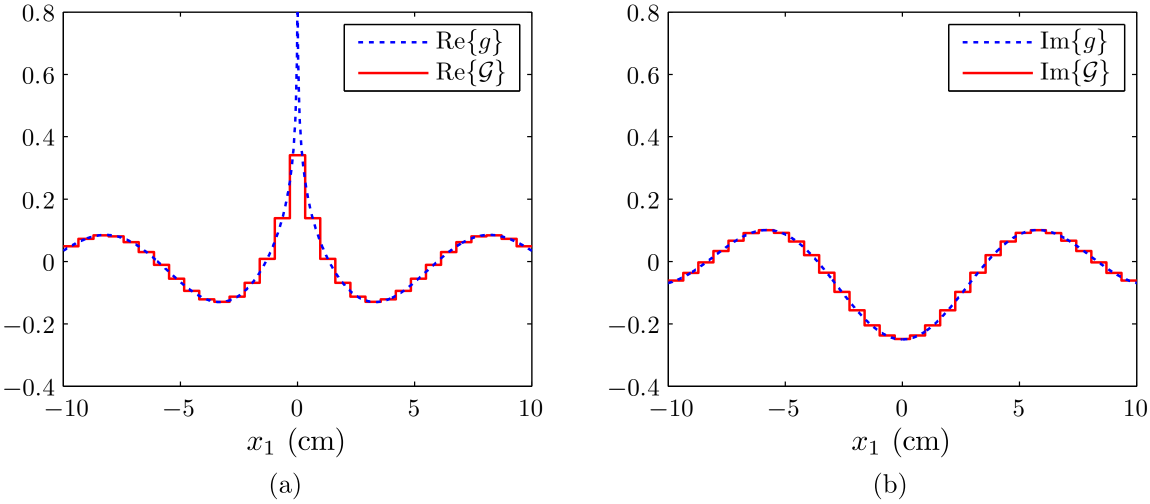

(a)

(b)

Fig. C.2: The real (a) and imaginary (b) part of the Green's function and it's weak form

Regular case

In the regular case we will always find that $|\boldsymbol{x}''| \leq |\boldsymbol{x}|$. We will thus only need the first expression of Eq. (C.2). Now, by using polar coordinates with $|\boldsymbol{x}''| = r$ and the formulas for derivatives, we obtain

$$\begin{aligned}\mathcal{G}(\boldsymbol{x}) &= -\frac{2\mathrm{j}}{(\Delta x)^2} H_0^{(2)}(k_\mathrm{b}|\boldsymbol{x}|) \int\limits_0^{\frac{1}{2}\Delta x} J_0(k_\mathrm{b} r) r \mathrm{d}r \\ &= -\frac{2\mathrm{j}}{k_\mathrm{b}(\Delta x)^2} H_0^{(2)}(k_\mathrm{b}|\boldsymbol{x}|) \Big[r J_1(k_\mathrm{b} r) \Big]_{r=0}^{r=\frac{1}{2}\Delta x} \\ &= -\frac{\mathrm{j}}{k_\mathrm{b}\Delta x} J_1(\tfrac{1}{2} k_\mathrm{b} \Delta x) H_0^{(2)}(k_\mathrm{b}|\boldsymbol{x}|)\,. \end{aligned} \tag{C.5}$$

We conclude this appendix by illustrating what the weak form of the two-dimensional Green's function looks like. For this we simulate a lossless, non-magnetic background with $\varepsilon_{\mathrm{r,b}} = 10$ at $f = 1$ GHz. We discretize a domain of 20-by-20 cm in 31-by-31 subdomains. The real and imaginary part of the Green's function and it's weak form are plotted along the x_1-axis in Fig. C.2.